Theoretical models of Buoyancy-induced flow in Rotating cavities

Tang, Hui

Award date:
2017

Awarding institution:
University of Bath

THEORETICAL MODELS OF BUOYANCY-INDUCED FLOW IN ROTATING CAVITIES

Hui Tang

A thesis submitted for the degree of Doctor of Philosophy

University of Bath
Department of Mechanical Engineering
December 2016

COPYRIGHT

. . . . . .

Abstract

Calculation of the blade tip clearances of the high-pressure-compressor rotors in aeroengines involves calculating the radial growth of the corotating compressor discs. This requires the calculation of the thermal growth of the discs, which in turn requires a knowledge of the disc temperatures and Nusselt numbers for the buoyancy-induced flow in the cavity between the discs. This is a strongly conjugate problem in which the equations for the fluid flow and the disc temperature are coupled.

In this thesis, the buoyancy-induced flow and heat transfer inside the compressor rotors is modelled assuming laminar Ekman-layer flow on the discs and compressible flow in the fluid core between the Ekman layers; conduction in the discs is modelled using a one-dimensional fin equation. The theoretical predictions are compared with Nusselt numbers and temperatures obtained from two independent sets of temperature measurements, obtained on a multi-cavity compressor rig, and the 'experimental' Nusselt numbers were calculated using a Bayesian model for the inverse solution of the fin equation. For most of the experimental cases, with Grashof numbers up to 10^{12}, mainly good agreement was achieved between the theoretical predictions and experimental values of the disc temperatures and Nusselt numbers. As predicted by the model, increasing the rotational Reynolds number can, under certain conditions, cause a *decrease* in the Nusselt numbers. Importantly, the results suggest that laminar Ekman-layer flow could occur even at the high Grashof numbers found in the compressor rotors of aeroengines.

An extension of the buoyancy model included empirical correlations for the Nusselt numbers for the compressor shroud and disc cobs. This extended model was used to predict the

temperature rise of the axial throughflow of cooling air in the compressor rotor, and reasonable agreement was achieved between the predicted and measured throughflow temperatures.

This is the first time a theoretical model (rather than CFD) has been used to predict the temperatures of a compressor disc and the axial throughflow, and the model takes only seconds to predict the temperatures that would take days or even weeks to predict using CFD. Some suggestions are made for future research to improve the extent and accuracy of the model.

Table of Contents

List of Figures

List of Tables

Nomenclature

a	inner radius (m)
a'	inner radius of buoyancy region (m)
A	cross-sectional area of disc (m^2); an event for Bayes' theorem
A_1, A_2	constants for the form of Rayleigh-Bénard convection
b	outer radius (m)
B	an event for Bayes' theorem
B_1, B_2	constants for the correlation of convection for the inner surface of the cob
Bi	Biot number ($= h_f b/k_s$)
Bi'	modified Biot number ($= 2b^2 h_f/k_s t$)
$\overline{Bi}$	mean of Bi
c	speed of sound in core ($= \sqrt{\gamma R T_{c,a}}$)
c_p	specific heat capacity at constant pressure
C	covariance matrix of Bi for the Bayesian model
C_1, C_2	constants for analytical solution of the special fin equation
Co	Coriolis parameter (=$2\left(1-\frac{\Omega_c}{\Omega}\right)\frac{1}{\beta(T_{o,b}-T_{c,b})}$)
d	distance between two plates (m)
d_h	hydraulic diameter ($= 2(a - r_s)$) (m)

F	posterior potential
g	acceleration of gravity (m/s^2)
G	gap ratio
Gr	Grashof number
Gr'	Grashof number defined in published literature
Gr_c	Grashof number in theory ($= Re_\phi'^2 \beta(T_{o,b} - T_{c,b})$)
Gr_f	Grashof number in experiments ($= (1 - a/b)^3 Re_\phi^2 \beta(T_{o,b} - T_f)$)
Gr_{sh}	Shroud Grashof number in theory ($= (s/2b)^3 Re_\phi'^2 \beta(T_{sh} - T_{c,b})$)
Gr_{sh}'	Shroud Grashof number in published literature
h	heat transfer coefficient
h_a	heat transfer coefficient for the inner surface of the cob ($= q_a/(T_{o,a} - T_c)$)
h_c	heat transfer coefficient based on T_c ($= q_o/(T_o - T_c)$)
h_f	heat transfer coefficient based on T_f ($= q_o/(T_o - T_f)$)
i	index for the instrumented disc in multi-cavity systems
I	integral
I_0, K_0	modified Bessel functions of the first and second kind, order 0
j	index for grid points
k	thermal conductivity of air (W/mK)
k_c	thermal conductivity of air in core (W/mK)
k_f	thermal conductivity of air in axial throughflow (W/mK)
k_s	thermal conductivity of disc (W/mK)

K_q	modified Bessel function of the second kind, order q
l	spatial length scale, parameter for Matérn covariance
L	characteristic length (m)
$\dot{m}_f$	mass flow rate of the axial throughflow (kg/s)
M	number of temperature measurements
Ma_c	Mach number in core ($= \Omega_c b/c$)
n	integer
N	number of grid points
Nu	Nusselt number
Nu'	Nusselt number defined in published literature
Nu_a	Nusselt number for the inner surface of the cob ($= h_a a/k$)
Nu_c	Nusselt number based on h_c ($= h_c r/k$)
Nu_f	Nusselt number based on h_f ($= h_f r/k$)
Nu_{av}	radially-weighted average Nusselt number
Nu_{sh}	shroud Nusselt number ($= q_{sh}(s/2)/k(T_{sh} - T_{c,b})$)
p	pressure; probability density
P	probalility
Pr	Prandtl number
q_o	heat flux from disc to air
$q_{o,av}$	radially-weighted average heat flux from disc to air
q_{sh}	heat flux from shroud to air

$\dot{Q}_a$	heat flow rate from the inner surface of the disc cob
$\dot{Q}_d$	heat flow rate from the downstream surface of the disc
$\dot{Q}_u$	heat flow rate from the upstream surface of the disc
$\dot{Q}_{sh}$	heat flow rate from the shroud
r	radius (m)
r_s	radius of inner shaft (m)
R	gas constant
Ra	Rayleigh number ($= PrGr$)
Ra'	Rayleigh number defined in published literature
Re_T	Reynolds number for the throughflow
Re_z	axial Reynolds number ($= 2\rho_f W d_h / \mu$)
Re_ϕ	rotational Reynolds number based on ρ_f and μ_f ($= \rho_f \Omega b^2/\mu_f$)
$Re_\phi{}'$	rotational Reynolds number based on $\rho_{c,b}$ and $\mu_{c,b}$ ($= \rho_{c,b} \Omega b^2/\mu_{c,b}$)
Ro	Rossby number ($= W/\Omega a$)
s	axial space between discs in cavity (m)
S	surface area of disc (m^2)
t	disc thickness (m)
T	static temperature (K)
T_{sh}	shroud temperature (K)
V	velocity (m/s)
W	axial component of velocity of throughflow (m/s)

x	nondimensional radius ($= r/b$)
x_a	radius ratio ($= a/b$)
$x_a{}'$	radius ratio ($= a'/b$)
z	axial distance from disc (m)

Greek symbols

α	angle of gradient of disc surface
β	volume expansion coefficient ($= 1/T_{ref}$) (K^{-1})
γ	ratio of specific heats
Γ	gamma function
ΔT	appropriate temperature difference (K)
ϵ	standard deviation of the experimental data obtained from the Bayesian method
θ	nondimensional temperature ($= (T_o - T_c)/(T_{o,b} - T_{c,b})$)
Θ	nondimensional disc temperature ($= (T_o - T_f)/(T_{o,b} - T_f)$)
μ	dynamic viscosity (m^2/s)
ρ	density (kg/m^3)
σ	standard deviation, parameter for Matérn covariance
τ	non-dimensional disc thickness ($= t/2b$)
Φ	parameters in inverse problems
$\overline{\Phi}$	mean of Φ
Ω	angular speed of rotor (s^{-1})

Ω_c	angular speed of core (s^{-1})

Subscripts

a	value at $r = a$
a'	value at $r = a'$
av	radially-weighted average value
b	value at $r = b$
c	value in core
exp	experimental value
f	value in axial throughflow
i	values for the i^{th} disc in a multi-cavity system
$i - 1/2$	values for half a cavity upstream away from the i^{th} disc
$i + 1/2$	values for half a cavity downstream away from the i^{th} disc
j	grid point
MAP	values obtained from the Bayesian method using maximum a posteriori
o	value on disc surface
ref	reference value
s	values for inner shafts
th	theoretical value
ϕ, r, z	circumferential, radial, axial direction

Acknowledgements

This thesis is principally supervised by Professor JM Owen. I would like to express my deepest gratitude to Professor J.M. Owen for his continuous guidance and support throughout my PhD. I would like to thank Professor G.D. Lock for always being there and giving me advice and support. Dr M Wilson is thanked for always being supportive. My gratitude is extended to Dr T Shardlow for offering guidance on using the statistical method in the report.

I would like to thank GE Global Research for the technical input and Mark Puttock-Brown from University of Sussex for allowing me to use the experimental data from his thesis.

The Chinese Scholarship Council is acknowledged for supporting me during my study as a PhD student at University of Bath.

I would also like to thank my colleagues in Turbomachinery Research Centre and friends in Bath who made my life so enjoyable. I would like to thank Sonia for proof reading some parts of my thesis.

Finally, my thanks go to my family for the support and encouragement.

Chapter 1 – Introduction

Fig. 1.1 is a typical modern civil turbofan engine. Good performance goes with high thermal efficiency, high thrust-to-weight ratio and low specific fuel consumption, which are achieved by high pressure ratios (as high as 50 for contemporary aeroengines, e.g. Trent 1000) and high by-pass ratios (above 10 for Trent 1000). This in turn shortens the blades in high pressure (HP) compressors. As a result, the relative blade tip clearance becomes proportionally large and hence the tip clearance flow is severe, which could lead to huge loss of efficiency. Therefore, it is vital to predict this tip clearance correctly in engine design processes.

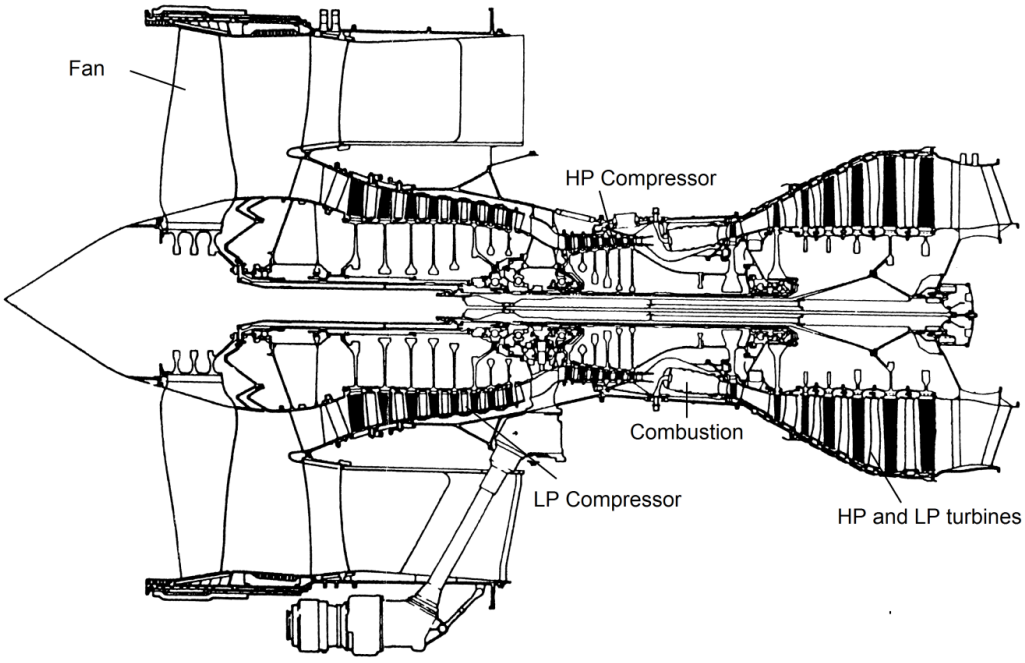

Fig. 1.1 Rolls-Royce Trent 884 (fan tip diameter 2.79m) (Cumpsty [2003])

The compressor tip clearance is determined by several sources, which include: radial growth, blade untwist and nonaxisymmetry. The compressor exit temperature of modern HP compressors goes above 800K and the rotational speed exceeds 10000 rpm. The combination of

high temperatures and high rotational speeds causes stresses on rotating discs, which leads to significant radial growth and in turn affects the blade tip clearance. The calculation of the rotational stress is quite straightforward, but the prediction of the thermal stress is much more complex, as it is determined by the temperature distribution on the disc. Therefore, to predict the tip clearance, it is necessary to predict the disc temperature, and as described below, this requires the prediction of the buoyancy-induced flow and heat transfer inside the cavities between the compressor discs.

The HP turbine inlet temperature of modern aeroengines is about 1800K, which is much higher than the melting point temperature of the component materials. Such engines would not be able to work without internal air systems. The internal air system as a whole may take up to 20% of the mainstream air flow for the use of ventilation (mostly cooling but also heating for some components), sealing, purging, etc. (*Rolls-Royce, [1986]*). Typical cooling and sealing airflow patterns are shown in Fig. 1.2. It is seen that the air is extracted from the compressors and then flows through the internal space of the compressor to cool and seal the turbine stages. On the internal path, the cold air will be heated by the compressor.

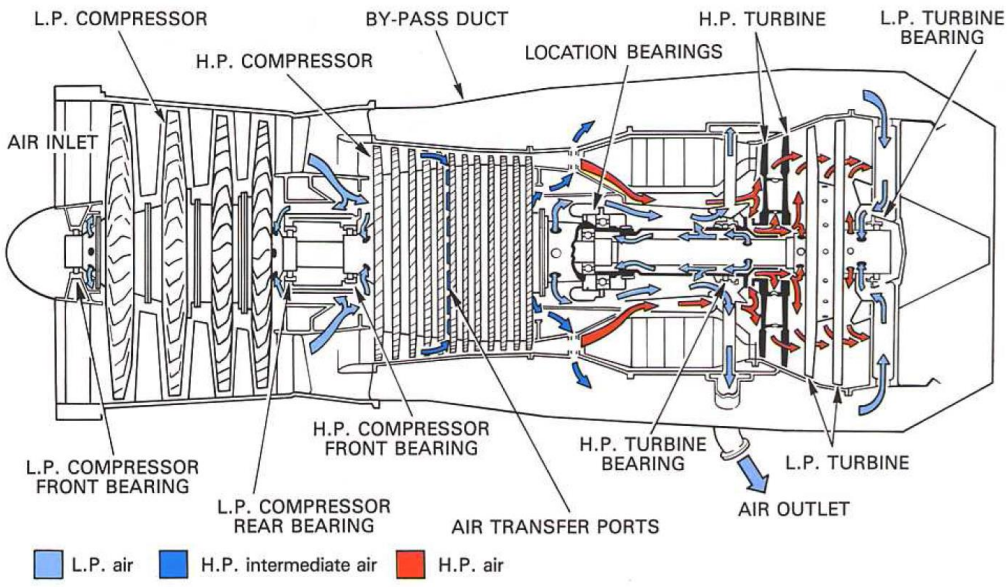

Fig. 1.2 General internal airflow pattern (Rolls-Royce [1986])

Fig. 1.3 is a schematic diagram of a typical HP compressor. The blade tip clearance can be found between the rotational parts and the stationary parts. The rotating disc can be found beneath the rotor blades. The cob is the bulbous hub of the disc. The shaft of the low pressure stages rotates in the axial centre. The cold air, which is bled from the mainstream, flows through the inner space between the HP compressor and the inner shaft.

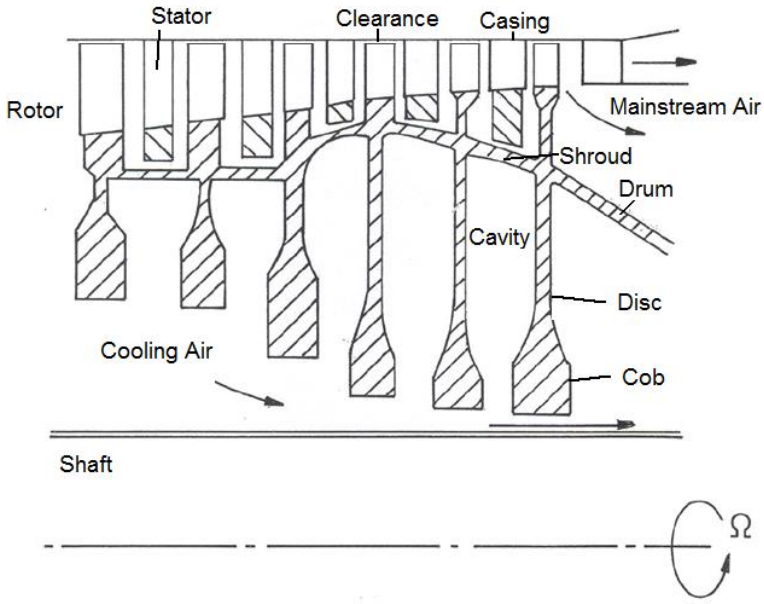

Fig. 1.3 Schematic diagram of a typical HP compressor

Rotating cavities are formed between adjacent co-rotating discs and the rotating shroud. The cold axial throughflow and the hot discs create buoyancy-induced flow and heat transfer inside the cavities. The heat transfer from the disc depends on the disc temperature, and the temperature depends on the heat transfer. Consequently this is a conjugate heat transfer problem.

The buoyancy-induced flow is the so-called 'Everest' of the rotating-disc problems. From the flow observation by *Farthing et al. [1992b]* and *Bohn et al. [2000]*, etc., the flow is highly three-dimensional, unsteady and unstable, which is extremely difficult and very expensive to compute using computational fluid dynamics (CFD). During the engine design process, the calculation will be done repeatedly. Hence a theoretical model for the buoyancy-induced flow,

which is much faster and of acceptable accuracy, is required for the engine design process. *Owen and Tang [2015]* proposed such a model for buoyancy-induced flow, which could be incorporated to predict the disc temperature and the temperature increase of the axial throughflow.

Therefore, the purpose of this research is to study the buoyancy-induced flow and heat transfer inside rotating cavities and to develop a theoretical model to predict the temperature distribution on the discs and the temperature increase of the axial throughflow.

First, a statistical method will be employed, in conjunction with a fin equation for conduction in the disc, to obtain distributions of the Nusselt numbers from disc temperature measurements. Then, the buoyancy model proposed by *Owen and Tang* will be used to predict the Nusselt numbers and temperatures of the discs as well as the temperature rise of the axial throughflow. Finally, the predictions will be compared with measurements made in multi-cavity experimental rigs.

In Chapter 2, the current research on the buoyancy-induced flow and the heat transfer in rotating cavities with axial throughflow is reviewed. The basic geometry and the important flow parameters are provided. Chapter 3 introduces the Bayesian method, the statistical method that is used to calculate Nusselt numbers from disc temperature measurements. Chapter 4 discusses the fin equation, which provides the model for the conduction in rotating discs. The fin equation can be solved directly to calculate disc temperatures from Nusselt numbers and inversely using the Bayesian method to obtain Nusselt numbers from the temperature measurements. Chapter 5 presents the methodology for the theoretical predictions. First, the buoyancy model proposed by *Owen and Tang* is introduced. Then the process of applying the buoyancy model in conjunction with the fin equation to predict the disc temperature, which is referred to as the 'theoretical model', is illustrated. After that, an extension of the theoretical model included correlations for cob heat transfer and shroud heat transfer is used to predict the temperature increase of the axial

throughflow. Chapter 6 compares the prediction of the disc temperatures with the measurements of *Atkins and Kanjirakkad [2014]*. Chapter 7 compares the prediction of the disc temperatures as well as the temperature increase of the axial throughflow with the measurements of *Puttock-Brown [2016]*. Chapter 8 summarises the conclusions of the thesis and suggests future research.

Chapter 2 – Literature Review

The literature review is focused on the published research on buoyancy-induced flow and heat transfer in rotating cavities with axial throughflow. A more general review can be found in *Owen and Long [2015]*. In this chapter, the typical geometry is presented, and the relevant nondimensional parameters are defined. The flow in isothermal cavities and the buoyancy-induced flow in heated cavities are presented. Then, an investigations of the heat transfer in rotating cavities are overviewed. Starting with the studies on the heat transfer in closed rotating cavities, the research on the heat transfer for the shroud is presented. After that, the studies on the disc heat transfer are listed. Finally, relevant CFD studies are reviewed.

2.1 Definition of important parameters

2.1.1 Geometry

A simplified geometry of a rotating cavity with axial throughflow in HP compressors is shown in Fig. 2.1. The terms 'cob', 'diaphragm' and 'shroud' are used to denote the bulbous hub at the centre of the disc, the thin section of the disc and the rotating outer casing. The discs and the shroud all rotate at one angular speed, Ω. The inner shaft rotates independently of the rotation of the discs. A rotating cavity is formed by two neighbouring co-rotating discs and the rotating shroud. There is axial throughflow of cooling air flowing between the cobs and the inner shaft.

The symbols used for the dimensions are also shown in the figure. The inner and outer radii of the rotating cavity are 'a' and 'b', respectively; 'r', 'ϕ' and 'z' are the coordinates in the radial, circumferential and axial direction, and the value of z is taken as the axial distance from

the upstream disc; 's' is the axial distance between two adjacent discs; the disc thickness is represented by 't'; 'r_s' denotes the radius of the inner shaft.

In this thesis, the subscript 'a' and 'b' are used to denote values at $r = a$ and b.

Nondimensional geometrical parameters are defined. The ***nondimensional radii***, x and x_a, are defined as

$$x = r/b \tag{2.1}$$

$$x_a = a/b \tag{2.2}$$

and the gap ratio

$$G = s/b \tag{2.3}$$

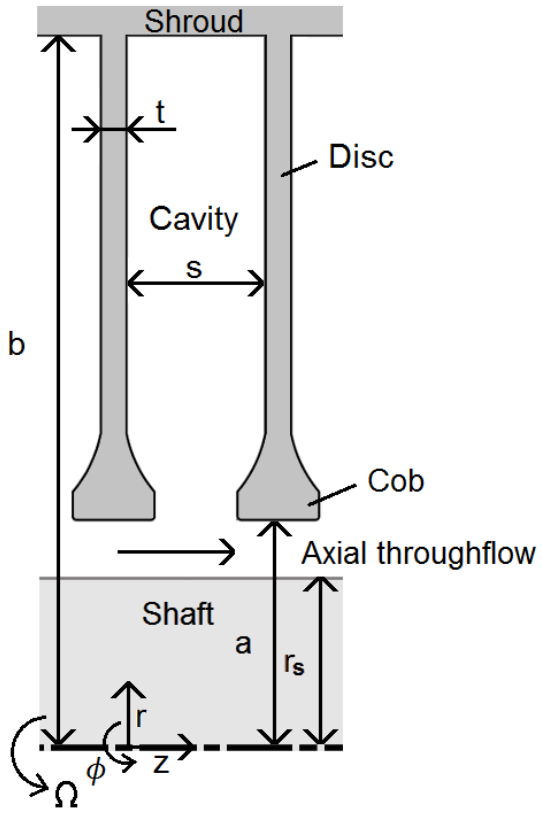

Fig. 2.1 Simplified diagram of a rotating cavity with axial throughflow

2.1.2 Nondimensional working parameters

The working condition of an experiment for the geometry in Fig. 2.1 is given by a group of nondimensional parameters. The air properties of the axial throughflow are used to define all the parameters, which are denoted using the subscript 'f'.

The parameter appropriate to the axial throughflow is the ***axial Reynolds number, Re_z,*** which is defined as:

$$Re_z = \frac{\rho_f W d_h}{\mu_f} \tag{2.4}$$

where W is the bulk-average axial velocity of the throughflow and it can be calculated from the mass flowrate of the axial throughflow, $\dot{m}_f$:

$$W = \frac{\dot{m}_f}{\rho_f \pi (a^2 - r_s^2)} \tag{2.5}$$

d_h is the hydraulic diameter calculated by

$$d_h = 2(a - r_s) \tag{2.6}$$

ρ_f and μ_f are the density and viscosity of the throughflow air.

The parameter involving the speed of rotation is the ***rotational Reynolds number, Re_ϕ,*** which is defined as

$$Re_\phi = \frac{\rho_f \Omega b^2}{\mu_f} \tag{2.7}$$

To compare the axial velocity and the rotational velocity, the ***Rossby number, Ro,*** is defined:

$$Ro = \frac{W}{\Omega a} \tag{2.8}$$

It can be rewritten in the form of the ratio of Re_z to Re_ϕ:

$$Ro = \frac{b^2}{d_h a}\frac{Re_z}{Re_\phi} \tag{2.9}$$

When the cavity is heated, buoyancy-induced flow can occur. The ***Grashof number, Gr,*** is defined considering the buoyancy effects in rotating cavities.

$$Gr = \frac{\rho_f^2 \Omega^2 b \beta \Delta T L^3}{\mu_f^2} \tag{2.10}$$

where L is the appropriate characteristic length. Regarding to the heat transfer for discs, the frequently-used characteristic length is the radial extent of the disc, $b - a$. β is the volume expansion coefficient of the axial throughflow air. For a perfect gas, $\beta = T_f^{-1}$. ΔT is the temperature difference between the shroud and the axial throughflow. In most cases, the disc temperature at $r = b$, $T_{o,b}$ can be taken as the shroud temperature. Hence $\boldsymbol{\beta \Delta T}$, which is named as the ***buoyancy parameter***, can be calculated by

$$\beta \Delta T = \frac{T_{o,b} - T_f}{T_f} \tag{2.11}$$

Eq. (2.10) can be rewritten in terms of the buoyancy parameter and the rotational Reynolds number as

$$Gr = \left(\frac{L}{b}\right)^3 Re_\phi^2 \beta \Delta T \tag{2.12}$$

An alternative parameter is the ***Rayleigh number***, $\boldsymbol{Ra}$, defined as

$$Ra = PrGr \tag{2.13}$$

where Pr is the Prandtl number defined as

$$Pr = \frac{\mu_f c_p}{k_f} \tag{2.14}$$

The group of the parameters, $Re_z, Re_\phi, Ro, Gr\ (or\ Ra)$ and $\beta\Delta T$ defines the working condition of the rotating cavities. As Ro is proportional to the ratio of Re_z to Re_ϕ and Gr is proportional to the product of Re_ϕ and $\beta\Delta T$, the working condition can be defined by three independent parameters, e.g. Re_z, Re_ϕ and $\beta\Delta T$ or Ro, Re_ϕ and $\beta\Delta T$.

2.1.3 Nondimensional disc temperatures and Nusselt numbers

To study the heat transfer in rotating cavities, the ***nondimensional disc temperature*** and the ***Nusselt number*** are necessary. Again, the air properties of the axial throughflow are used in these definitions.

The nondimensional disc temperature, Θ, is defined as

$$\Theta = \frac{T_o - T_f}{T_{o,b} - T_f} \tag{2.15}$$

The Nusselt number, Nu, is defined to quantify the heat transfer for the disc:

$$Nu = \frac{h_f r}{k_f} \tag{2.16}$$

where h_f is the heat transfer coefficient using T_f as the reference temperature, which can be calculated by

$$h_f = \frac{q_o}{T_o - T_f} \tag{2.17}$$

where q_o is the heat flux from the disc to the air.

It is also useful to define the average disc Nusselt number, Nu_{av}:

$$Nu_{av} = \frac{q_{o,av} b}{k_f (T_{o,av} - T_f)} \tag{2.18}$$

where av is used to define the radially-weighted average value over the disc surface. $q_{o,av}$ and $T_{o,av}$ can be calculated from

$$q_{o,av} = \frac{\int_a^b 2\pi r q_o dr}{\int_a^b 2\pi r dr} \tag{2.19}$$

$$T_{o,av} = \frac{\int_a^b 2\pi r T_o dr}{\int_a^b 2\pi r dr} \tag{2.21}$$

Thus Nu_{av} can be calculated from Nu and Θ:

$$Nu_{av} = \frac{\int_{x_a}^1 Nu\Theta dx}{\int_{x_a}^1 \Theta x dx} \tag{2.20}$$

2.2 Flow structure in rotating cavities

2.2.1 Isothermal rotating cavities with axial throughflow

Before discussing the buoyancy-induced flow, the flow in isothermal cavities with axial throughflow is reviewed.

Owen and Pincombe [1979] used flow visualization and laser-Doppler anemometry (LDA) to study the flow structure in isothermal rotating cavities with $G = 0.53, x_a = 0.1$ at different Rossby numbers (from 0.8 to ∞). An inner shaft was not included. The approximate ranges of Reynolds numbers were: $5 \times 10^3 < Re_z < 10^5$ and $4 \times 10^4 < Re_\phi < 3 \times 10^5$. A toroidal vortex generated by the axial flow was identified in the cavities near the central axial flow, which can be seen in Fig. 2.2. The region of the toroidal vortex was reduced with Ro decreasing. The ratio of the measured tangential velocity to the disc rotational speed, $V_\phi/\Omega r$, exceeded unity inside the toroidal vortex region, and it decreased as Ro decreases, which is shown in Fig. 2.3. In the outer part of the toroidal vortex, the flow is close to solid-body rotation.

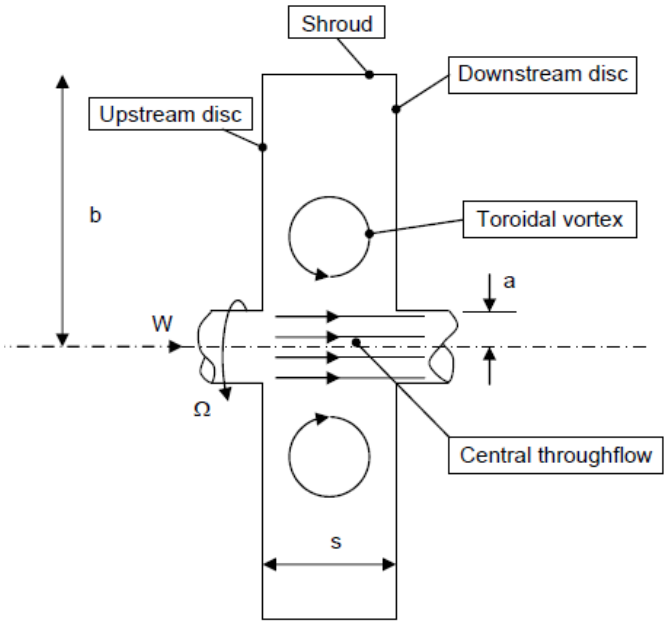

Fig. 2.2 Simplified diagram of axial throughflow in an isothermal rotating cavity

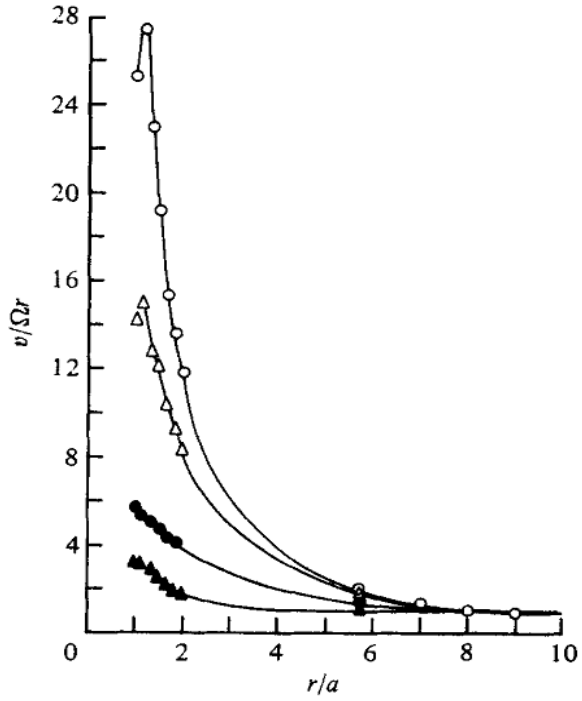

($Re_z = 3.1 \times 10^4, z/s = 0.189$: —○—, Ro = 128; —Δ—, Ro = 64; —●—, Ro = 28; —▲—, Ro = 16)

Fig. 2.3 Ratios of tangential velocities (v) to disc velocities in turbulent flow at different Rossby number (Owen and Pincombe [1979])

Similar phenomena were found by *Farthing et al. [1992b]* using flow visualization and LDA in four different isothermal rotating rigs (rig a, b, c and d) at a constant axial Reynolds number ($Re_z = 5000$) and different Rossby numbers ($1 < Ro < \infty$). The rigs were all with $x_a = 0.1$ but different gap ratios (G), which are 0.533, 0.400, 0.267 and 0.133. An inner shaft was not included. The visual impressions of smoke patterns showed that the radial extent of the toroidal vortex decreased when Ro and G decreased. The measured tangential velocities showed that $V_\phi/\Omega r$ in the toroidal vortex region exceeded unity and decreased as Ro decreased and the gap ratio, G, decreased.

2.2.2 Buoyancy-induced flow

In *Farthing et al. [1992b]*, flow visualization and LDA were also made in heated rotating cavity rigs with $x_a = 0.1$ and different gap ratios. The cavity could be heated symmetrically (both discs were heated) and asymmetrically (only one disc was heated). Three disc temperature profiles -- constant, increasing and decreasing temperatures-- were tested. The flow visualization in rotating cavities with G = 0.12, 0.267 and 0.27 showed that the buoyancy-induced flow was highly 3-D and unsteady for all the cases. A similar flow regime was observed for all the heated cavities and it was depicted using the schematic in Fig. 2.4. In the core between the Ekman-layers, the cold air flows radially outward inside a 'radial arm', on either side of which there is a vortex. On the forward side (along the direction of the rotation), the vortex circulates cyclonically (that is, it rotates in the same direction as the disc), and on the other side, the vortex circulates anti-cyclonically. This entire structure rotates at a slightly lower speed than the disc. The number of radial arms increased with cobs added in a cavity heated by an increasing disc temperature profile. LDA measurements were made in rotating cavities with a constant disc temperature distribution at $x = 0.63$, for $G = 0.12, 0.24$ and 0.36, $0℃ < \Delta T < 80℃$, $5 \times 10^3 < Re_z < 10^4, 0.5 < Ro < 7$ and $5 \times 10^4 < Re_\phi < 9.5 \times 10^5$. The measured tangential velocities were all less than the velocity of the disc. The effects of G, ΔT, Re_ϕ and Ro on $V_\phi/\Omega r$

are presented in Fig. 2.5. Fig. 2.5a shows that at $Re_\phi = 4 \times 10^5$ and $Re_z = 10^4$, $V_\phi/\Omega r$ decreases approximately linearly as ΔT increases, and larger decreases occur when G increases. Fig. 2.5b shows that at $Re_z = 10^4$ and $\Delta T = 60$℃, $V_\phi/\Omega r$ decreases as Re_ϕ increases and G increases when $Re_\phi < 2 \times 10^5$. However, when $Re_\phi > 2 \times 10^5$ there are no further reductions and there is even an increase for larger gap ratios. Fig. 2.5c shows the effect of Ro for a cavity with $G = 0.24$. $V_\phi/\Omega r$ decreases as Ro increases at $0.5 < Ro < 2$ but it increases with Ro increasing when Ro > 2. The reasons for these effects were not clear and no final correlation for $V_\phi/\Omega r$ was obtained.

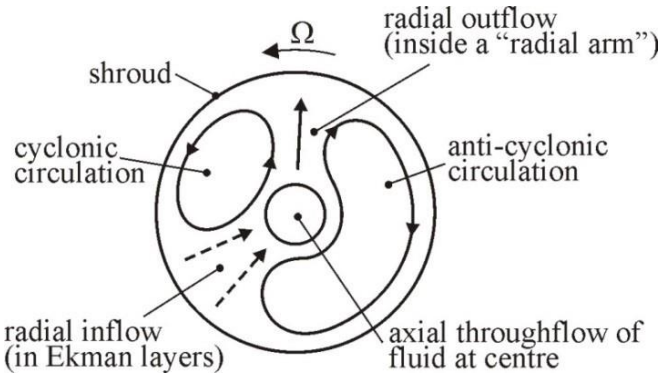

Fig. 2.4 Schematic of buoyancy-induced flow in heated rotating cavities (Farthing et al. [1992b])

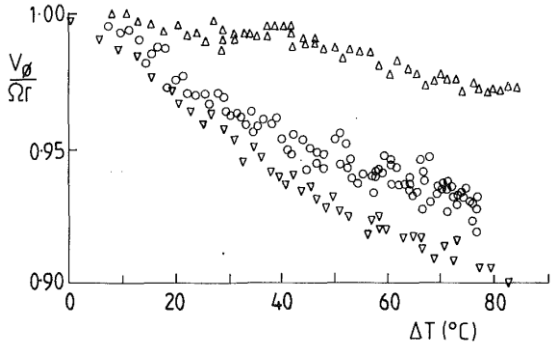

Fig. 2.5a Variation of $V_\phi/\Omega r$ with ΔT for a heated rotating cavity at $Re_z = 10^4, Re_\phi = 4 \times 10^5, Ro = 1.4, z/s = 0.5$ and $x = 0.63$. $\Delta: G = 0.12$; ○ : $G = 0.24$; ∇: $G = 0.36$.

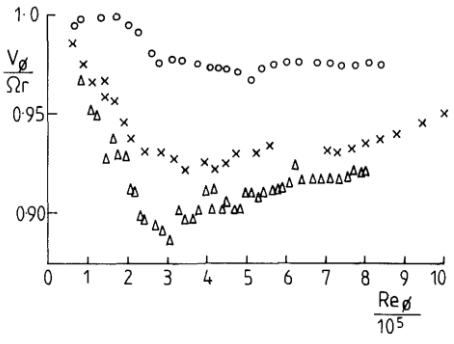

Fig. 2.5b Variation of $V_\phi/\Omega r$ with Re_ϕ for a heated rotating cavity at $Re_z = 10^4, \Delta T = 80K, z/s = 0.5$ and $x = 0.63$. ○ : $G = 0.12$; x : $G = 0.24$; Δ : $G = 0.36$.

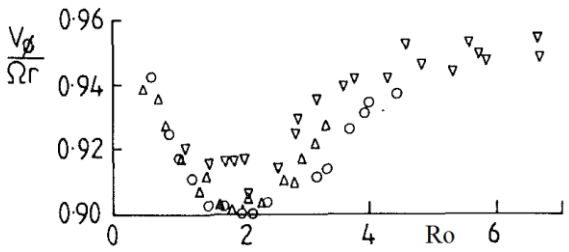

Fig. 2.5c Variation of $V_\phi/\Omega r$ with Ro for a heated rotating cavity with $G = 0.24, \Delta T = 80K, z/s = 0.5$ and $x = 0.63$. $\nabla : Re_\phi = 4 \times 10^5$; $\circ : Re_\phi = 6 \times 10^5$; Δ: $Re_\phi = 8 \times 10^5$.

Fig. 2.5 Effects of $\beta\Delta T$, Re_ϕ and Ro on $V_\phi/\Omega r$ (Farthing et al. [1992b])

Bohn et al. [2000] made flow visualization of a symmetrically heated rotating cavity rig with axial throughflow and a co-rotating inner shaft (see Fig. 2.6), for $x_a = 0.3, G = 0.2$ and $d_h/b = 0.09$. The ranges of the working parameters were $2 \times 10^4 < Re_z < 7 \times 10^4, 2 \times 10^5 < Re_\phi < 8 \times 10^5$ and $\beta\Delta T \approx 0.3$. Similar flow structure to that in *Farthing et al. [1992b]* was observed. Fig. 2.7 shows the presence of a 'radial arm'. The visualisation results showed that the flow structure rotated at 88%-90% of the speed of the discs and oscillated periodically. Furthermore, laminar behaviour was seen in all the experimental conditions.

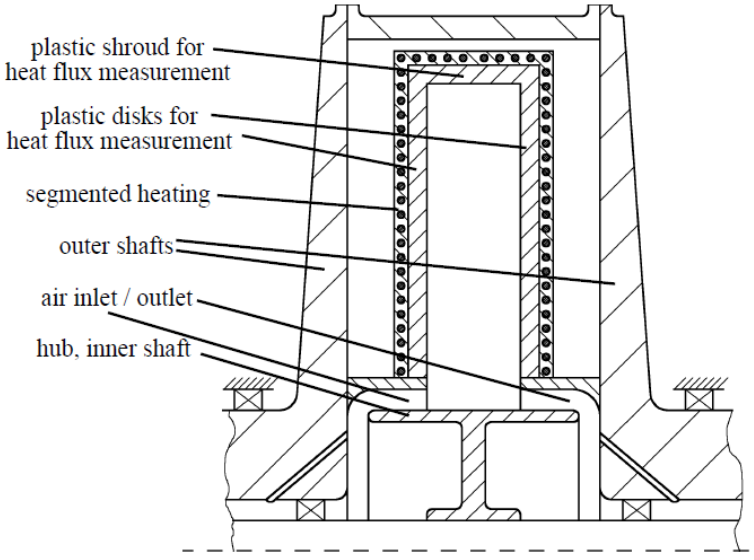

Fig. 2.6 Rotating cavity rig used by Bohn et al. [2000]

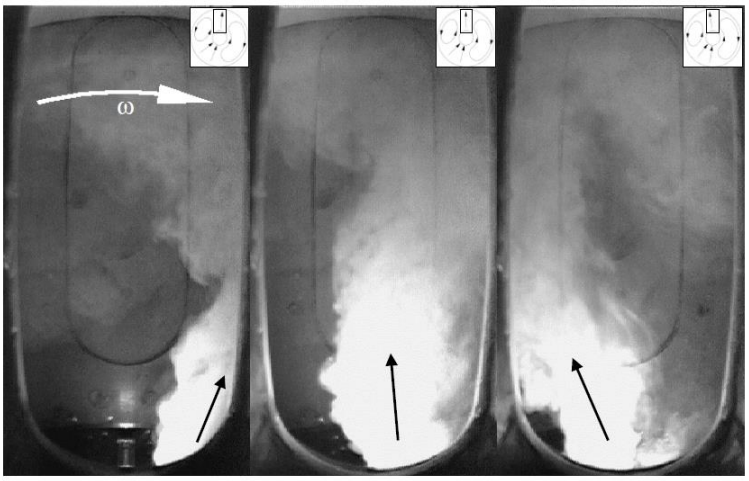

Fig. 2.7 Visualisation of a radial arm by Bohn et al. [2000]

Owen and Powell [2006] used LDA to measure the velocity inside an asymmetrically heated rotating cavity rig (only downstream disc was heated) with axial throughflow and an inner rotating shaft, for $x_a = 0.40$, $G = 0.20$ and $d_h/b = 0.013$. The rig is shown in Fig. 2.8. The range of the working condition was: $1.4 \times 10^3 < \mathrm{Re_z} < 5 \times 10^4, 4 \times 10^5 < Re_\phi < 3.2 \times 10^6$ and $0.05 < Ro < 14$. Fig. 2.9a Shows the time-average radial variation of $V_\phi/\Omega r$ at $z/s = 0.5$ for $Re_\phi = 4.3 \times 10^5, Re_z = 3 \times 10^3$ and $\beta\Delta T \approx 0.25$. It can be seen that $0.96 < \mathrm{V_\phi}/\Omega r < 0.99$ for $0.67 < x < 0.97$. Fig. 2.9b shows that, at the same Reynolds number, $\mathrm{V_\phi}/\Omega r$ decreases with increasing ΔT, and that the value of $\mathrm{V_\phi}/\Omega r$ exceeds unity when ΔT is small, indicating the presence of the toroidal vortex. The spectral analysis of the velocity measurements showed a multi-cell flow structure comprising one, two or three pairs of cyclonic and anti-cyclonic vortices.

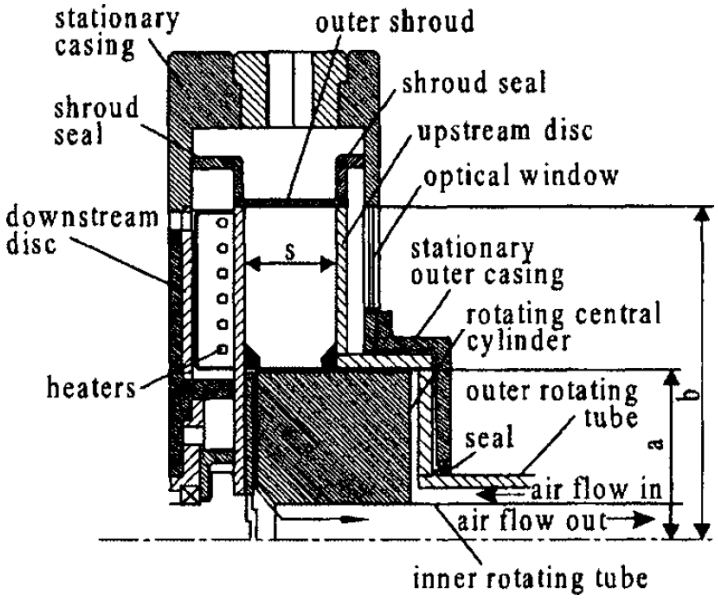

Fig. 2.8 Schematic diagram of rotating cavity rig in Owen and Powell [2006]

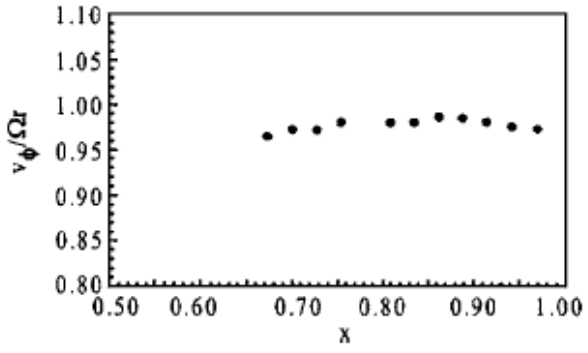

Fig. 2.9a Steady-state radial variation of $V_\phi/\Omega r$ at $Re_\phi = 4.3 \times 10^5, Re_z = 3 \times 10^4$ and $z/s = 0.5$

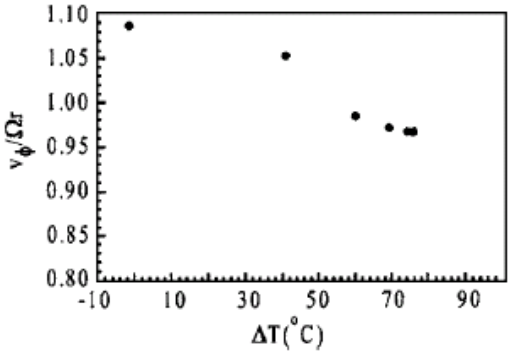

Fig. 2.9b Transient variation of $V_\phi/\Omega r$ with ΔT at $Re_\phi = 4.3 \times 10^5, Re_z = 3 \times 10^4, z/s = 0.5$ and $x = 0.674$

Fig. 2.9 Experimental data of $V_\phi/\Omega r$ in Owen and Powell [2006]

Long et al. [2007] presented LDA velocity measurements inside a multiple cavity rig with axial throughflow and with two different stationary inner shafts, for $x_a = 0.318, G = 0.195$ and $d_h/b = 0.092$ and 0.164. The rig, which was designed to be a 70% full scale replica of a high pressure compressor internal air system, is shown in Fig. 2.10. The shroud of the cavity was heated with pressurised external hot air. The velocities in cavities 3 and 4 were measured. Fig. 2.11 shows the radial distribution of the measured tangential velocity in cavity 3, and under the

cob of disc 2, for $d_h/b = 0.164, Re_\phi = 4.9 \times 10^5, \beta\Delta T = 0.23$ and $Ro = 3.57$. The solid line is the rotational speed of the discs, and vertical bars on the symbols denote the uncertainty of the measurements. It can be seen that, in the inner part of the cavity where $r/b < 0.5$, $V_\phi/\Omega r$ is above unity, which indicates the existence of the toroidal vortex; in the outer part of the cavity where $r/b > 0.6$, $V_\phi/\Omega r$ is close to 1, which shows the buoyancy region. This suggests that, for this Rossby number, the toroidal vortex region in the inner region extends to $x \approx 0.6$ and that the outer region is dominated by buoyancy-induced flow. Fig. 2.12 shows the values of $V_\phi/\Omega r$ for different Rossby numbers and different clearance ratios, d_h/b. 'Wide' and 'narrow' annular clearance denote $d_h = 0.164$ and 0.092. It is shown that, for both configurations, $V_\phi/\Omega r$ increases as Ro increases in the inner region and tends to 1 in the outer region. d_h/b has a strong effect on $V_\phi/\Omega r$: the narrow clearance case has much lower value of $V_\phi/\Omega r$ in the inner region. For all the narrow clearance cases and the wide clearance cases with lower Rossby numbers, $V_\phi/\Omega r$ in the inner region is less than 1, which indicates that the toroidal vortex region was suppressed. Besides, it was shown that the axial velocities inside the cavity were close to zero and the radial velocities were comparable to the relative tangential velocity, $V_\phi - \Omega r$.

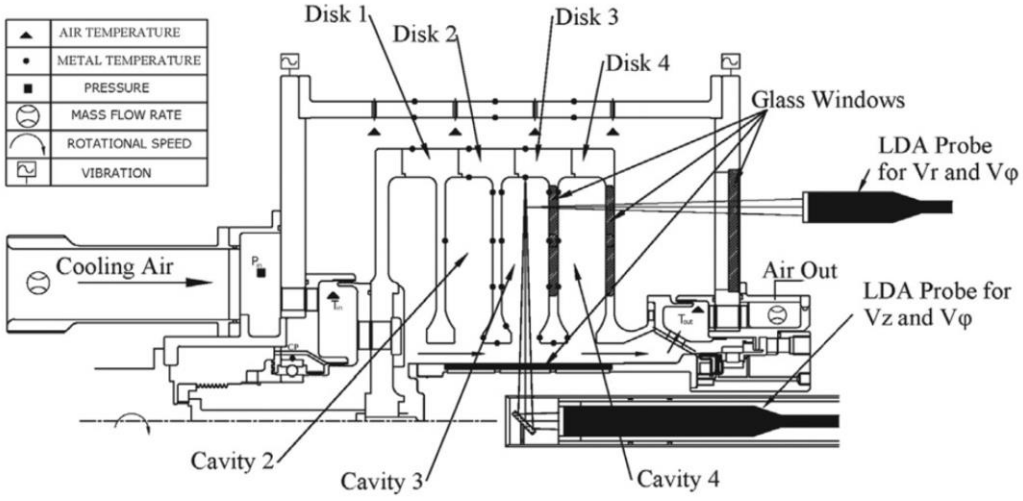

Fig. 2.10 Multi-cavity rig used by Long et al. [2007]

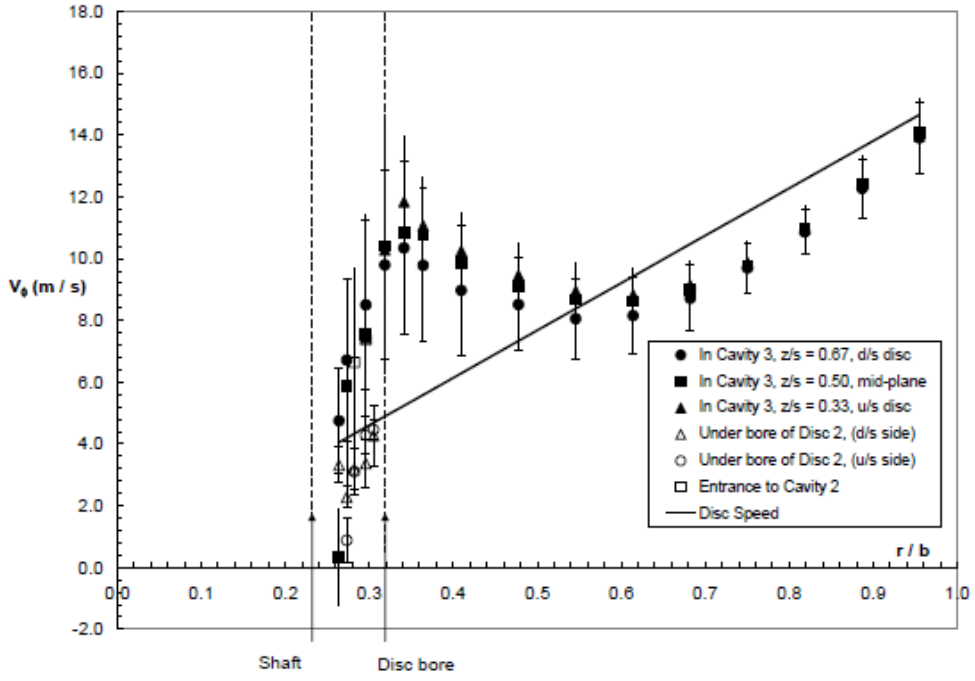

Fig. 2.11 Radial distribution of the rotational speed at different axial positions. (d_h / b = *0.164, Ro = 3.57*) (Long et al. [2007])

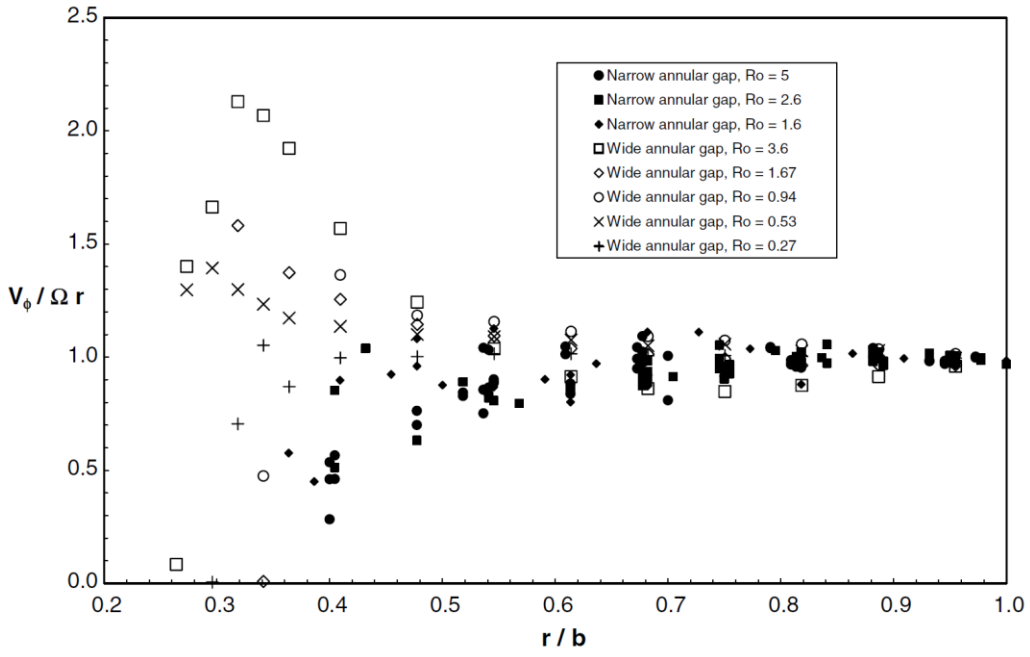

Fig. 2.12 Radial variation of normalised tangential velocity, $V_\phi/\Omega r$ *at z/s = 0.5*, with Rossby number for two clearance ratios: narrow gap: d_h / b = *0.092,* and wide gap: d_h / b = *0.164* (Long et al. [2007])

Owen [2010] explained the buoyancy-induced flow structure in rotating cavities with axial throughflow as a self-organising system where the principle of ***Maximum Entropy Production*** (MEP) could be applied. The number of vortex pairs is associated with the maximum production of entropy, which corresponds to the maximum transfer of heat and work in rotating cavities with axial flow. It was shown from CFD results by *Bohn et al. [2006]* (see Section 2.4) that the flow can change periodically between one, two and three pairs. Based on the MEP theorem, it is probable that the magnitudes of the Nusselt numbers, which corresponds to the rates of entropy production, associated with the multi states were similar.

2.3 Heat transfer in rotating cavities

2.3.1 Shroud heat transfer

2.3.1.1 Closed rotating cavity

When the cavity is closed, the flow will be purely buoyancy-induced. Hence to study the heat transfer for the shroud near which the buoyancy-induced flow dominates, it is useful to discuss the heat transfer in closed rotating cavities. The geometry of a closed rotating cavity can be represented by Fig. 2.13.

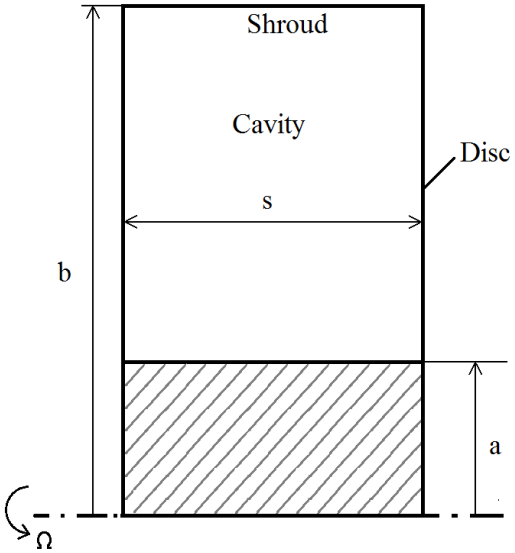

Fig. 2.13 Schematic of a closed rotating cavity

When the shroud is heated, this configuration is analogous to that of two parallel horizontal cold upper and hot lower plates, where the Rayleigh-Bénard-type convection can occur. The Rayleigh-Bénard convection can be shown by Fig. 2.14.

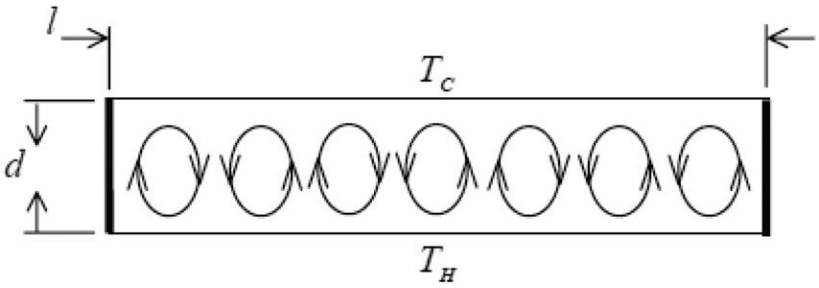

Fig. 2.14 Rayleigh-Bénard convection between horizontal plates

The Rayleigh-Bénard convection is the free convection induced by gravity. In a gravitational field, the Rayleigh number is defined as

$$Ra' = Pr\beta\Delta T\frac{gd^3}{\nu^2} \tag{2.21}$$

where d and ΔT are the distance and temperature difference between the cold upper plate and the hot lower plate. The Rayleigh-Bénard convection, which is unstable in the pattern of counter-rotating vortices pairs, occurs when Ra' reaches a critical value, 1708. *Grossmann and Lohse [2000]* proposed a semi-empirical correlation for the heat transfer:

$$Nu' = 0.27Ra'^{1/4} + 0.038Ra'^{1/3} \tag{2.22}$$

where Nu' is defined as the ratio of the heat flux for the convection to that for the conduction. The 1/4 exponent is usually associated with laminar convection at low Ra', and the 1/3 exponent corresponds to turbulent convection at high Ra'. An alternative correlation was given by *Hollands et al. [1975]*

$$Nu' = 1 + 1.44\max\left[1 - \frac{1708}{Ra'}, 0\right] + \max[\left(\frac{Ra'}{5830}\right)^{\frac{1}{3}} - 1, 0] \tag{2.23}$$

When the free convection is applied to the configuration of the closed rotating cavities, the gravitational term in Eq. (2.23) should be replaced by the rotational term. Then a similar form of correlation for free convection in closed rotating cavities with a heat shroud could be obtained. *Bohn et al. [1995]* made heat transfer experiments in closed rotating cavities with a heated shroud. The experiments were performed on three different geometric configurations A, B and C. For cavity A, $x_a = 0.35$ and $G = 0.34$; for cavity B, $x_a = 0.52$ and $G = 0.50$; for cavity C, similar to B, $x_a = 0.52$ and $G = 0.50$, but there were eight radial partitions extending axially across the cavity to create eight 45 degree segments. Their definition of the Rayleigh number was:

$$Ra' = Pr\beta\Delta T\frac{\Omega^2 r_m(b-a)^3}{\nu^2} \tag{2.24}$$

where r_m is the mean radius. ΔT is the temperature difference between the hot shroud and the cold inner surface. Empirical correlations were obtained for the heat transfer from the shroud of three cavities A, B and C, and for Ra' up to 10^{12} and $\beta\Delta T$ up to 0.3:

$$Nu' = 0.246Ra'^{0.228} \tag{2.25}$$

$$Nu' = 0.317Ra'^{0.211} \tag{2.26}$$

$$Nu' = 0.365Ra'^{0.213} \tag{2.27}$$

where Nu' is the Nusselt number on the shroud, which is defined as the ratio of the convection to conduction:

$$Nu' = \frac{\ln(b/a)\, q_{sh} b}{k\Delta T} \tag{2.28}$$

The power of Ra' are all close to that for laminar flow, $1/4$, rather than that for turbulent flow, 1/3. Hence they are similar to the laminar part of the correlation for Rayleigh-Bénard convection.

2.3.1.2 Rotating cavity with axial throughflow

Long and Tucker [1994] measured the heat transfer from the shroud in the rig shown in Fig. 2.15 with axial throughflow and without inner shaft, for $x_a = 0.1$ and $G = 0.13$. Experiments were conducted for a range of parameters; $\beta\Delta T \leq 0.3; 2 \times 10^3 \leq Re_z \leq 1.6 \times 10^5$ and $2 \times 10^5 \leq Re_\phi \leq 2 \times 10^6$. The heat fluxes in the shroud were measured using two thermopile fluxmeters at $z/s = 1/2$ and $z/s = 1/3$. They also measured the air temperature inside the cavity by three thermocouple probes at $z/s = 1/2$. The measured air temperature was also used as the reference temperature to define the Grashof number and the Nusselt number. Due to the large uncertainty of the measurements and the limited range of the Grashof number, no correlation was obtained, but it was suggested that an established correlation for free convection from horizontal surfaces can be used to predict the shroud heat transfer in a rotating cavity with axial throughflow.

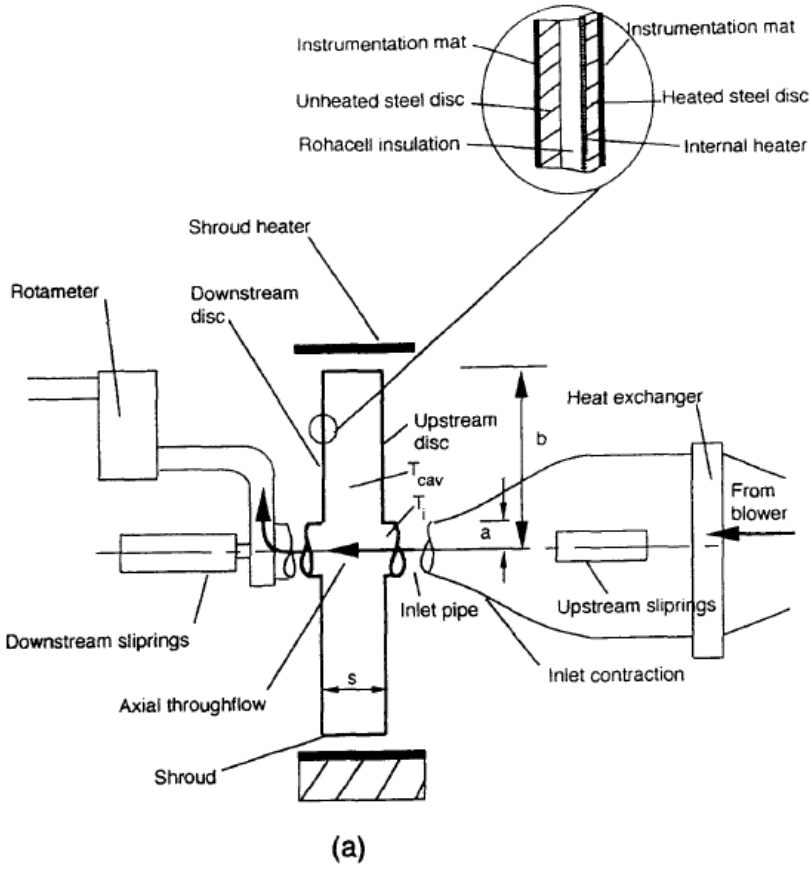

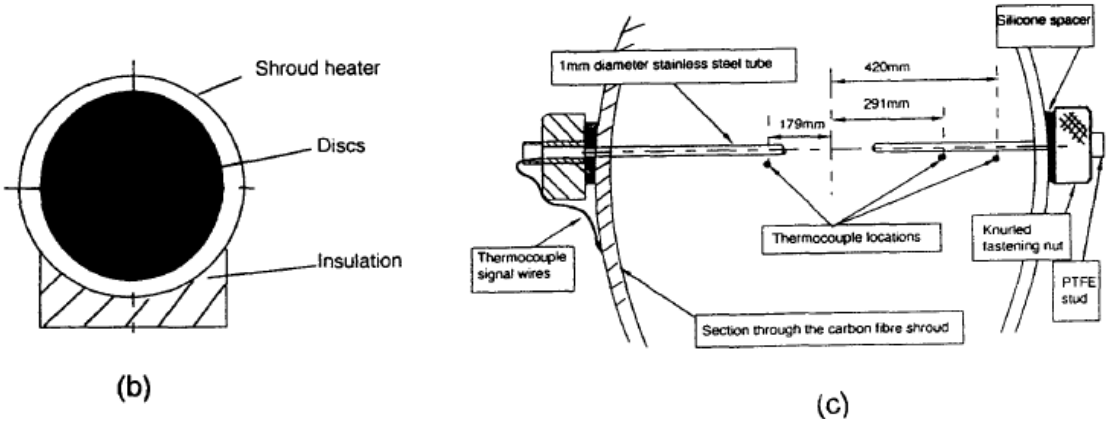

Fig. 2.15 Schematic diagram of the rotating test rig used by Long and Tucker [1994]: *b = 0.4845m, a = 0.045m, s = 0.065 (G = 0.13)* or *0.174m (G = 0.36)*: (a) side view; (b) end view; (c) cavity air temperature probe

Long and Childs [2007] measured the shroud Nusselt numbers for cavity 2 and 3 in the multi-cavity rig shown in Fig. 2.10 for both $d_h/b = 0.092$ and 0.164. Heat flux through the titanium shroud was determined from the measured temperature difference across the shroud, then the 1-D conduction equation for the shroud was solved to calculate Nu_{sh}. The variation of Nu_{sh} with the shroud Grashof number, Gr_{sh}, for $d_h/b = 0.164$ is presented in Fig. 2.16. Their definitions of Nu_{sh} and Gr_{sh} were

$$Nu_{sh} = \frac{q_{sh}(s/2)}{k_f(T_{sh} - T_f)} \tag{2.29}$$

$$Gr_{sh} = \frac{\rho_f^2 \Omega^2 b}{\mu_f^2} \beta \Delta T \left(\frac{s}{2}\right)^3 \tag{2.30}$$

The characteristic length is chosen to be the value of shroud area over perimeter, $s/2$.

It is shown in Fig. 2.16 that Nu_{sh} is mainly dependent on Gr_{sh} and that there is no systematic effect of Reynolds number on Nu_{sh}. *Long and Childs* also mentioned that the shaft rotation does not have any systematic effect on the shroud Nusselt number. Also there was no conspicuous difference between the results for cavities 2 and 3. The curves for the laminar free convection

and turbulent free convection for horizontal plates (*Incropera and DeWitt, [1996]*) are also shown in the figure. The correlation for laminar free convection is

$$Nu_{sh} = 0.54(Gr_{sh}Pr)^{1/4} \tag{2.31}$$

and that for turbulent free convection is

$$Nu_{sh} = 0.15(Gr_{sh}Pr)^{1/3} \tag{2.32}$$

Moreover, the semi-empirical correlation of *Grossman and Lohse [2000]* for Rayleigh-Bénard convection was provided in Eq. (2.22). Based on the definition of Gr_{sh} and Nu_{sh}, it can be rewritten in terms of the convection for the shroud as

$$Nu_{sh} = 0.166(Gr_{sh}Pr)^{1/4} + 0.038(Gr_{sh}Pr)^{1/3} \tag{2.33}$$

The form of Eq. (2.33) was used to correlate the experimental results, namely,

$$Nu_{sh} = A_1(Gr_{sh}Pr)^{1/4} + A_2(Gr_{sh}Pr)^{1/3} \tag{2.34}$$

where A_1 and A_2 are the two constants adjusted to get the closest Nu_{sh}.

For $d_h/b = 0.092$,

$$Nu_{sh} = 0.216(Gr_{sh}Pr)^{1/4} + 0.0494(Gr_{sh}Pr)^{1/3} \tag{2.35}$$

and for $d_h/b = 0.164$,

$$Nu_{sh} = 0.25(Gr_{sh}Pr)^{1/4} + 0.057(Gr_{sh}Pr)^{1/3} \tag{2.36}$$

Eq. (2.36) is shown in the Fig. 2.16 (Eqn. (20) in the figure). It can be seen that the correlation is closer to the laminar free convection than the turbulent one. However, the Nusselt numbers for $d_h/b = 0.164$ were much greater than those for $d_h/b = 0.092$. The difference was attributed to the difference in the flow structure for the two clearance ratios. As shown in Fig. 2.12, the swirl for $d_h/b = 0.164$ is higher, which indicates that more fluid is drawn into the

cavity. Therefore the air temperature near the shroud could be lower, which results in higher Nusselt numbers.

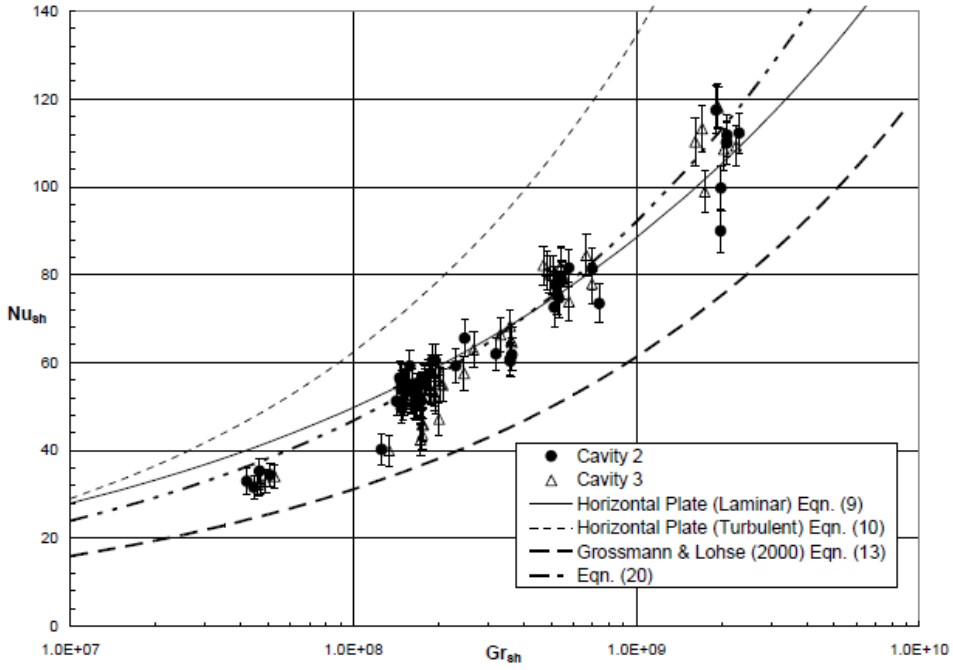

Fig. 2.16 Measured variation of shroud Nusselt number with Grashof number for rotating cavity rig with axial throughflow, $d_h/b = 0.164$, $4.1 \times 10^4 < Re_z < 2.0 \times 10^5$, $0.27 < Ro < 5.8$ (Long and Childs [2007])

2.3.2 Disc heat transfer

Farthing et al. [1992a] made heat transfer measurements for two rotating cavity rigs with axial throughflow of cooling air and without an inner shaft, for $x_a \approx 0.1$ and $G = 0.138$ and 0.267. The schematic of the rig is shown in Fig. 2.17. The range of the working condition was $2.0 \times 10^5 \leq Re_\phi \leq 5.0 \times 10^6, 2 \times 10^4 \leq Re_z \leq 1.6 \times 10^5$ and $0.25 \leq \beta\Delta T \leq 0.3$. The discs could be heated symmetrically and asymmetrically. The temperature of the disc either increased with radius or decreased. It was shown that, for symmetrically heated cases, the Nusselt numbers on both discs were similar, which indicated symmetry of the flow about the mid axial plane. For asymmetrically heated cases, the Nusselt number distribution on the heated disc was similar to that in the symmetrical case, and the distribution on the unheated disc had a similar trend but lower magnitude. Radiation heat transfer for symmetrical cases was small but for

asymmetrical cases was significant and could be as high as the convection. Different disc temperature profiles would cause different Nusselt number shapes: the local Nusselt number increased with radius for increasing temperature profiles and decreased for decreasing temperature profiles. From the comparison between the Nusselt number of the two rigs (only the downstream disc was heated and a radially increasing temperature was used), it was shown that the central shaft and the gap ratio had no significant effect on the Nusselt numbers. Fig. 2.18 shows the variation of average Nusselt numbers for the discs, Nu_{av}, with Re_ϕ in the rig symmetrically heated with an increasing temperature profile, for $G = 0.138$ and $Re_z = 2, 4, 8$ and 16×10^4. It is shown that there is little difference between the average Nusselt numbers on the upstream and downstream discs, and that Nu_{av} increases with increasing Re_z. It can also be seen that, at low Re_ϕ, Nu_{av} for all the cases increases with increasing Re_ϕ, but at high Re_ϕ ($> 3 \times 10^6$), Nu_{av} for the cases with lower Re_z starts to decrease. For the symmetrically heated cavity $G = 0.138$ with disc temperature increasing with radius, the authors found a correlation between the local Nusselt number and the local Grashof number, Gr'.

$$Nu = 0.0054 Re_z^{0.30} Gr'^{0.25} (x^{-1} - 1)^{0.25} \tag{2.37}$$

where $Gr' = ((\Omega^2 r^4)/v^2)(T_o - T_f)/T_f$. A comparison between the experimental values and the correlation is shown in Fig. 2.19. It can be seen that the Nusselt number increases with radius. Also it is worth noting that, in Eq. (2.37), the power for Gr, 1/4, is that for laminar flow instead of that for turbulent flow, 1/3.

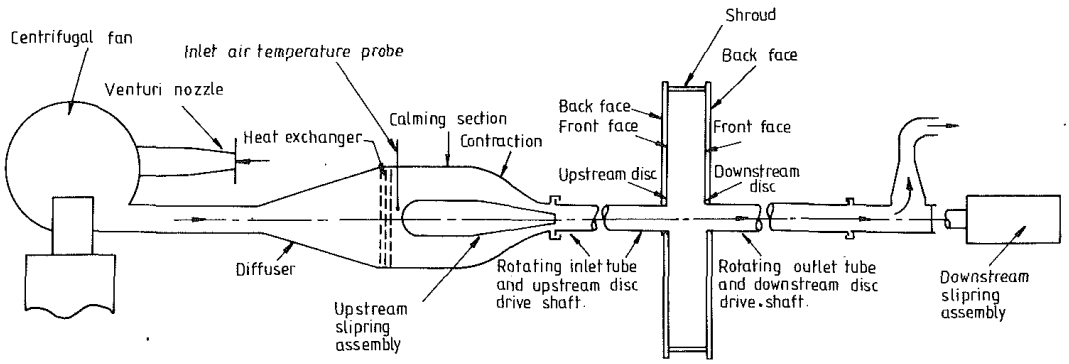

Fig. 2.17 Schematic of the experimental rig used by Farthing et al. [1992a]

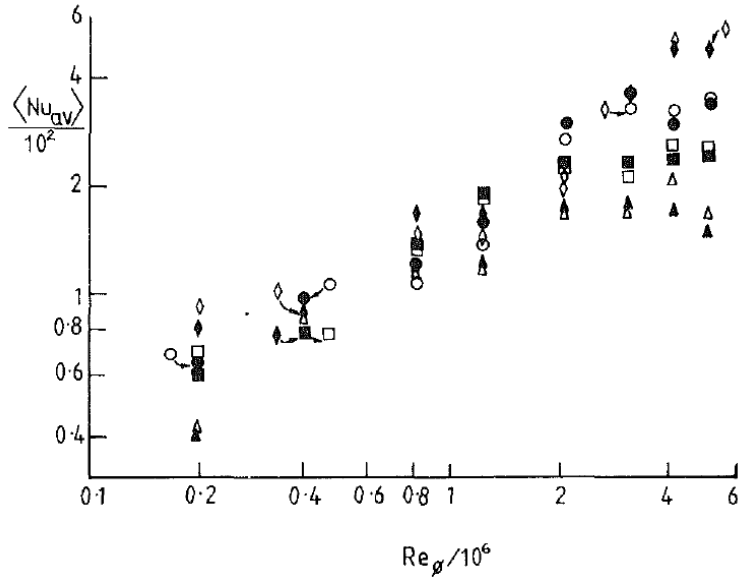

Empty symbols denote results for the upstream disc and solid symbols denote results for the downstream disc. Δ, ▲: $Re_z = 2 \times 10^4$; □, ■: $Re_z = 4 \times 10^4$; ○, ●: $Re_z = 8 \times 10^4$; ◊, ♦: $Re_z = 1.6 \times 10^5$

Fig. 2.18 Variation of average Nusselt number with Re_ϕ and Re_z for a symmetrically heated cavity with an increasing temperature distribution for *G = 0.138* (Farthing et al. [1992a])

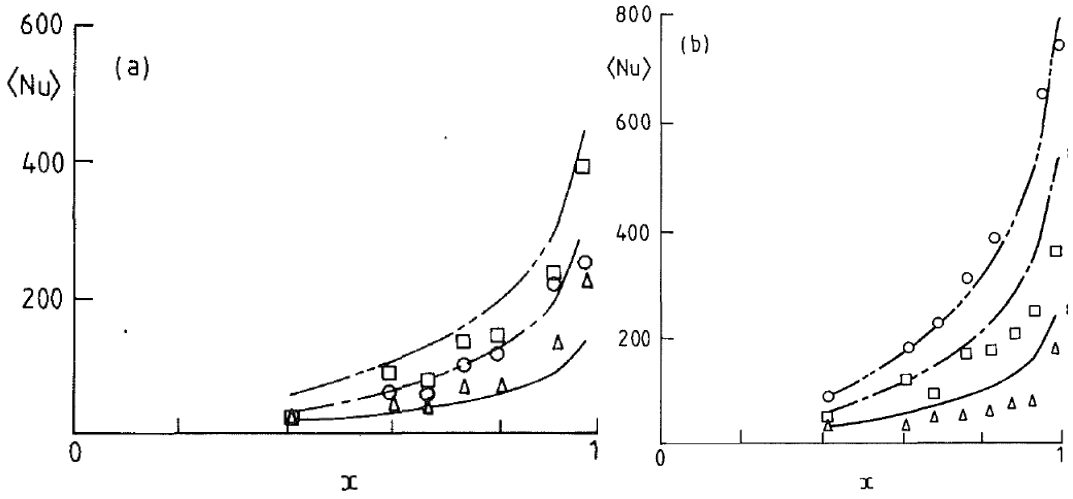

(a) $Re_z = 2 \times 10^4$, Δ, — : $Re_\phi = 0.4 \times 10^6$ and $Ro = 2.2$; □, — ▪ —: $Re_\phi = 2.0 \times 10^6$ and $Ro = 0.45$; ○, — ▪ ▪ —: $Re_\phi = 5.0 \times 10^6$ and $Ro = 0.18$.

(b) $Re_z = 16 \times 10^4$, Δ, — : $Re_\phi = 0.4 \times 10^6$ and $Ro = 18$; □, — ▪ —: $Re_\phi = 2.0 \times 10^6$ and $Ro = 3.6$; ○, — ▪ ▪ —: $Re_\phi = 5.0 \times 10^6$ and $Ro = 1.4$

Fig. 2.19 Comparison of radial variations of local Nusselt numbers between experiment (symbols) and Eq. (2.37) (curves) for the downstream disc of a symmetrically heated cavity (*G = 0.138*) with an increasing temperature distribution (Farthing et al. [1992a])

Kim et al. [1994] measured the disc Nusselt numbers in a rotating cavity with axial throughflow and without an inner shaft for $x_a = 0.25$ and $G = 0.4$. The cavity was heated symmetrically with either uniform heat flux (case A) or uniform temperature (case B). The test rig is shown in Fig. 2.20. The two cases have similar maximum disc temperature. The tests were carried out for four axial Reynolds numbers ($Re_z = 2.5 \times 10^3, 5.0 \times 10^3, 1 \times 10^4$ and 2.5×10^4) and four rotational Reynolds numbers ($Re_\phi = 0, 1.7, 3.9$, and 5.11×10^5). Fig. 2.21 presents the effects of the rotational Reynolds number and the axial Reynolds number on the averaged Nusselt numbers for both cases. It is shown that Nusselt numbers increase with increasing Re_z. In addition, for $Re_z = 2.5 \times 10^3$, Nusselt numbers on both discs are similar and initially increase and then decrease with increasing Re_ϕ; for $Re_z = 2.5 \times 10^4$, Nusselt numbers on the downstream disc are higher than those on the upstream disc and initially decrease and then increase with increasing Re_ϕ.

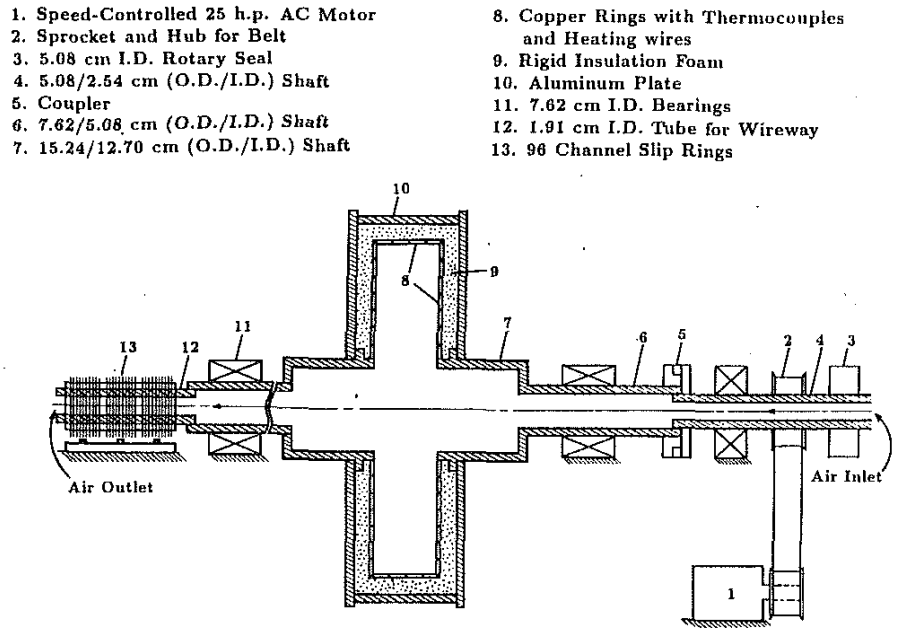

Fig. 2.20 Schematic of the rotating test rig used by Kim et al. [1994]

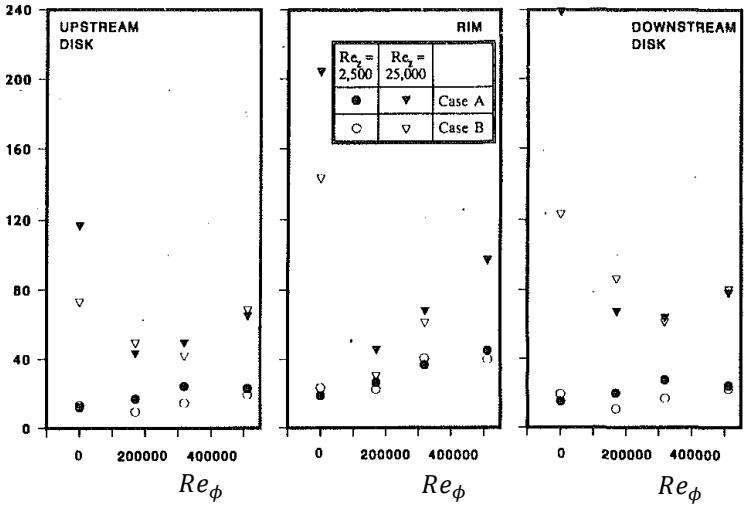

Fig. 2.21 Effect of rotational Reynolds number and axial Reynolds number on the averaged Nusselt number of the disc and the shroud for case A and B (left: upstream disc, Nu_{av}; mid: shroud , Nu_{sh}; right: downstream disc, Nu_{av}) (Kim et al. [1994])

Long [1994] measured the disc heat transfer in a single rotating cavity rig with $x_a = 0.1$ and two gap ratios, $G = 0.13$ and 0.36. No inner shaft was included. The test rig was shown in Fig. 2.15. The range of working conditions was $0.03 \leq \beta\Delta T \leq 0.3; 2 \times 10^3 \leq Re_z \leq 1.6 \times 10^5$ and $2 \times 10^5 \leq Re_\phi \leq 5 \times 10^6$. The cavities were all heated symmetrically with an radially increasing temperature profile and the shroud could be heated or unheated. It was shown that Nusselt number increased with increasing radius, and, for $Ro < 4$, the value was not significantly affected by the gap ratio. Also, the disc heat transfer was not significantly affected by the shroud heat transfer. Furthermore, the Nusselt number increased with increasing $\beta\Delta T$. Although no correlation was obtained for the Nusselt numbers, its dependence on $Re_\phi\sqrt{\beta\Delta T}$, namely, $\sqrt{Gr}$, was verified. Besides, the air temperatures inside the cavity at three radial locations were measured and they were used to estimate the fraction of throughflow entering the cavity. It was shown that the percentage decreased with increasing Ro.

Bohn et al.[2000] also measured the disc heat transfer in the symmetrically heated rig shown in Fig. 2.6 for six cases. The nondimensional parameters for these cases are given in Table 2.1. The outer radius, b, is used as the characteristic length to define Gr, hence here

$$Gr = Re_{\phi}^{2}\beta\Delta T \tag{2.38}$$

For the six cases, the shroud was unheated and the discs were heated with quasi-linearly increasing temperature profiles. The measured Nusselt numbers for the six test cases were consistent with the experiments by *Sri Kantha [1987]*. Case 1 and case 2 have similar nondimensional parameters but different inlet pressure and rotating speeds. There was no apparent difference between the Nusselt number for these two cases. The results for cases 3-6 are shown in Fig. 2.22. It can be seen that, for both the upstream and downstream disc, the Nusselt number tends to increase radially, and its maximum value (at $x = 1$) increases as Re_{ϕ} and hence Gr increases. In addition, the Nusselt number increases with increasing Re_z. Also it is seen that the Nusselt number on the downstream disc is higher than that on the upstream one, particularly at low radius where there are more effects from the axial throughflow.

Case	1	2	3	4	5	6
Ro	0.28	0.28	0.56	1.1	0.56	0.97
$Re_{\phi}/10^5$	8.0	8.0	4.0	2.0	8.0	8.0
$Re_z/10^4$	2.0	2.0	2.0	2.0	4.0	7.0
$\beta\Delta T$	0.27	0.27	0.27	0.27	0.27	0.27
$Gr/10^{11}$	1.7	1.7	0.43	0.11	1.7	1.7

Table 2.1 Nondimensional parameters for Bohn et al. [2000]

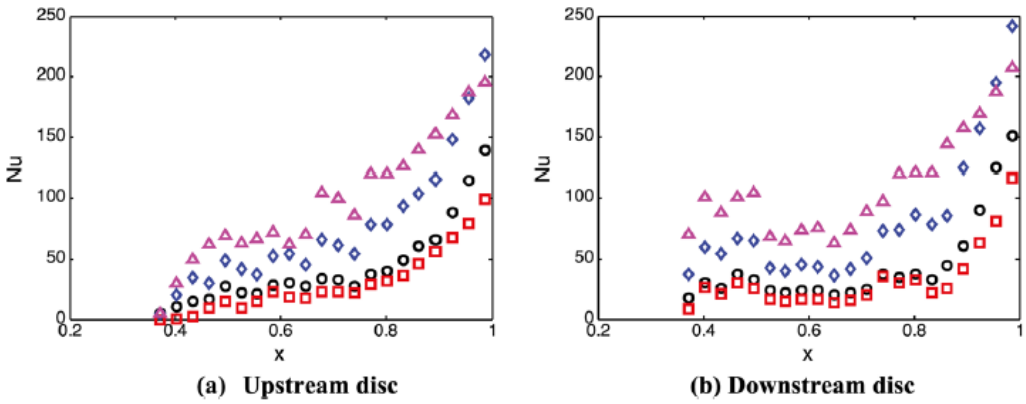

○, case 3; □, case 4; ◊, case 5; Δ, case 6

Fig. 2.22 Radial distribution of Nusselt numbers for (a) upstream and (b) down stream discs (from Bohn et al. [2000])

Owen and Powell [2006] also measured the Nusselt numbers on the heated downstream disc in the rig described in Fig. 2.8 for Re_ϕ up to 3.2×10^6, Re_z up to 4.8×10^4 and Rossby numbers between 0.05 and 14. It was shown that when Ro was small, Nu increased with increasing radius, which corresponds to the effects of buoyancy-induced flow, and that when Ro was large, Nu decreased radially, which is consistent with the effects of the throughflow.

Günther et al. [2014] measured the disc temperature from a two cavity test rig with an inner stationary shaft, for $G \approx 0.31, x_a = 0.21$ and $d_h/b = 0.062$ (see Fig. 2.23). Tests were carried out for the range of $2.1 \times 10^4 \leq Re_z \leq 1.2 \times 10^5, 2.7 \times 10^4 \leq Re_\phi \leq 1.1 \times 10^7$ and $0.2 \leq Ro \leq 136$. The temperature measurements were interpolated first by a spline and then by a fourth-order polynomial, then these were used as the boundary condition for a 2D conduction solver to calculate the disc heat flux. Radial distributions of the calculated heat flux showed that, at $x < 0.6$, on the left side of the middle disc, the heat was transferred out from the disc to the air in the cavity, while on the right side, it was transferred into the disc from the cavity. Also the magnitude of both heat fluxes was close to one another. At $x > 0.6$, the heat was transferred out on both sides with similar magnitudes and increased with radius, a result which indicates the buoyancy-induced convection. It was also shown that the heat flux increased with increasing Re_z, while the influence of rotation on the heat flux was complex. The highest heat flux was measured at medium Re_ϕ. The authors also measured the air temperatures at two radial locations, and they used these temperatures and a heat balance to estimate the percentage of the axial throughflow ingested into the cavity. Similar to *Long [1994]*, it was revealed that the percentage of ingestion increased with increasing Ro.

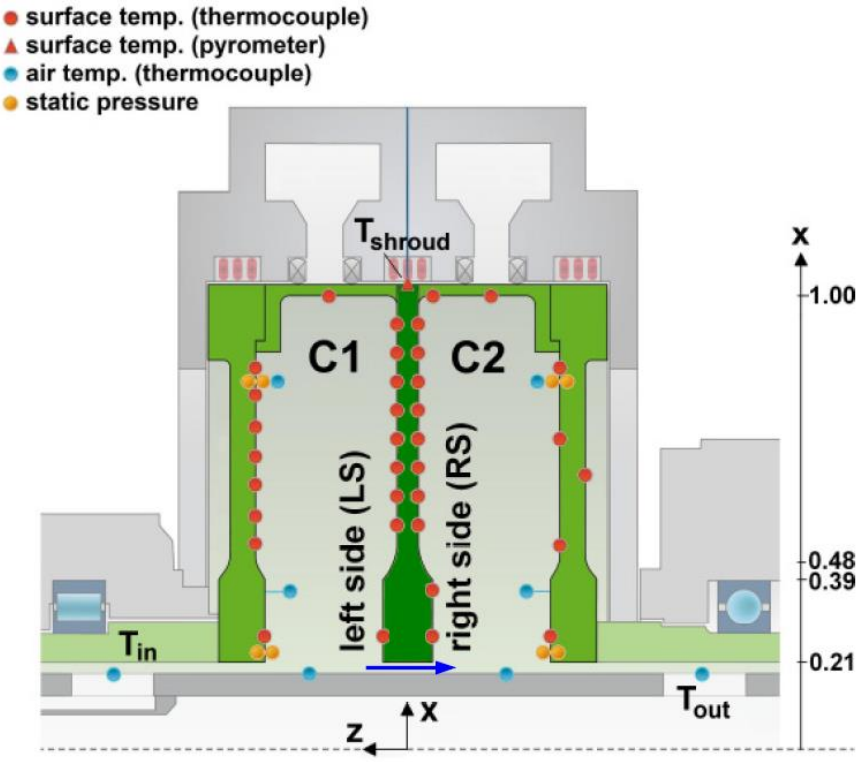

Fig. 2.23 Scheme of the test rig used by Günther et al. [2014]

Atkins and Kanjirakkad [2014] measured the disc Nusselt numbers in a similar rig to the one with the wide gap in Long and Childs [2007] (see Fig. 2.10), for $\frac{a}{b} = 0.318, G = 0.195$ and $\frac{d_h}{b} = 0.164$). The flow path of the rig used by *Atkins and Kanjirakkad* is shown in Fig. 2.24. The range of the working conditions is $7.8 \times 10^4 < Re_\phi < 3.5 \times 10^6, 2 \times 10^4 < Re_z < 1.1 \times 10^5, 0.3 < Ro < 5, 1.5 \times 10^9 < Gr < 9 \times 10^{11}, 0.05 < \beta\Delta T < 0.32$. Nineteen cases were presented and the nondimensional parameters are shown in Table 2.2. In their definition of Gr, $(b - a)$ is used as the characteristic length, hence

$$Gr = (1 - a/b)^3 Re_\phi^2 \beta\Delta T \tag{2.39}$$

The measured nondimensional disc temperatures, Θ, are shown in Fig. 2.25.

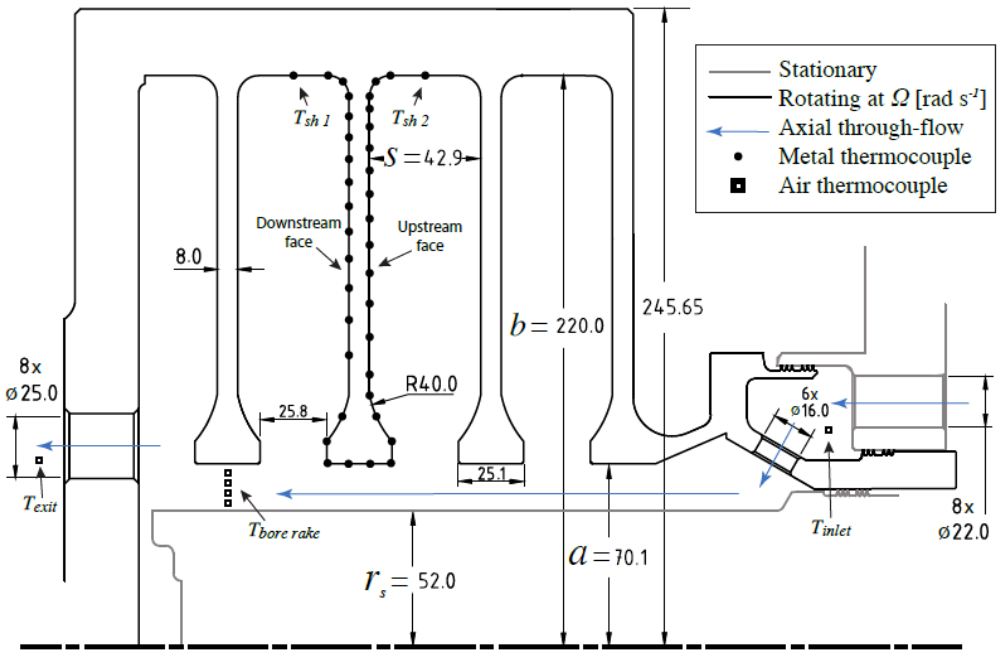

Fig. 2.24 Flow path of rotating cavity rig from Atkins and Kanjirakkad [2014]

	Ro ≈ 5						Ro ≈ 1							Ro ≈ 0.6		Ro ≈ 0.3			
Case No	1a	1b	1c	1d	1e	1f	2a	2b	2c	2d	2e	2f	2g	3a	3b	4a	4b	4c	4d
Ro	4.7	4.7	4.9	4.9	4.5	4.5	0.8	0.8	0.9	0.9	1.0	1.0	1.0	0.6	0.6	0.3	0.3	0.3	0.3
$Gr/10^{11}$	0.0017	0.003	0.0085	0.015	0.062	0.14	0.065	0.1	0.44	0.84	1.7	2.5	3.9	5.7	9.1	0.4	1.0	3.7	7.8
$\beta\Delta T$	0.08	0.17	0.05	0.11	0.09	0.24	0.09	0.16	0.11	0.23	0.13	0.19	0.32	0.15	0.32	0.06	0.16	0.12	0.29
$Re_\phi/10^6$	0.078	0.077	0.19	0.19	0.46	0.45	0.46	0.45	1.13	1.1	2.1	2.1	2.1	3.5	3.1	1.4	1.4	3.1	3.0
$Re_z/10^5$	0.19	0.19	0.5	0.5	1.1	1.1	0.19	0.18	0.51	0.5	1.1	1.1	1.1	1.1	1.1	0.2	0.2	0.48	0.48

Table 2.2 Nondimensional parameters for experiments of Atkins and Kanjirakkad [2014]

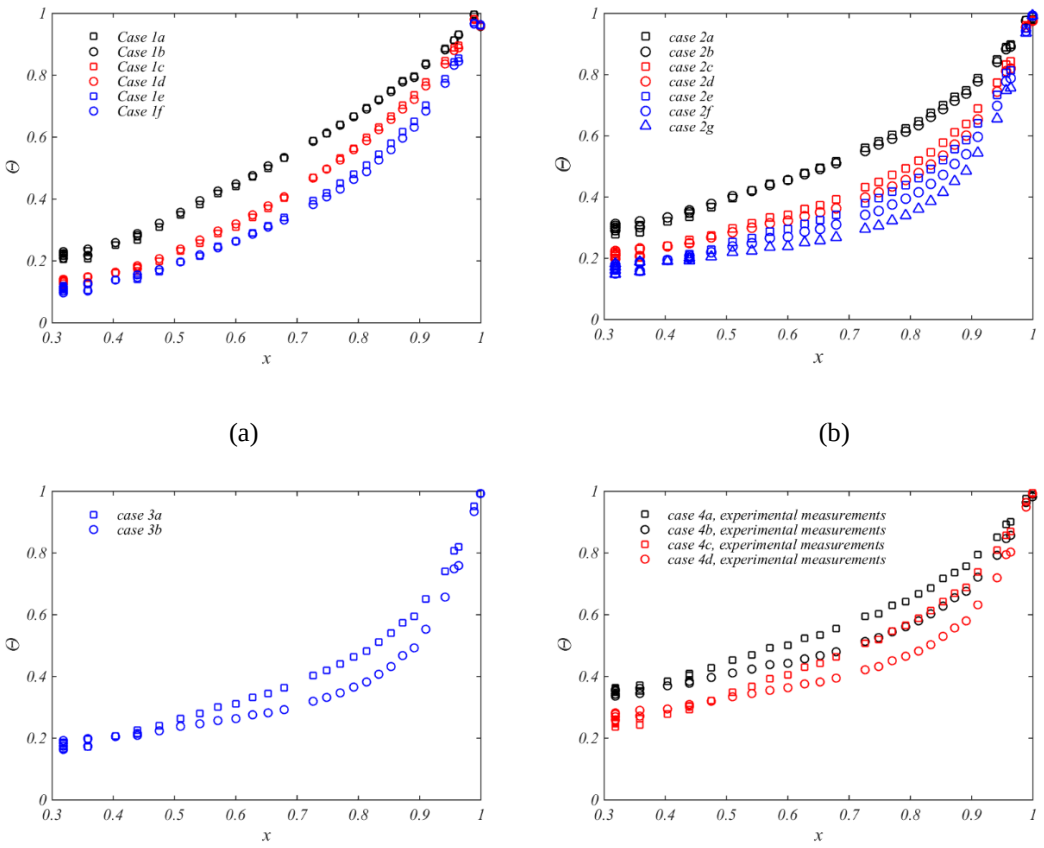

Fig. 2.25 Radial distribution of disc temperatures for experiments of Atkins and Kanjirakkad [2014]: (a) *Ro* ≈ *5*; (b) *Ro* ≈ *1*; (c) *Ro* ≈ *0.6*; (d) *Ro* ≈ *0.3*;

Tang et al. [2015] used these measured disc temperatures to determine the radial distribution of the Nusselt number. The thin section of the rotating disc was treated as a circular fin and the fin equation was solved inversely using Bayesian statistics to calculate Nu from Θ. The calculated Nu as well as their 95% confidence intervals (shaded regions around the curves) are presented in Fig. 2.26 for cases 2a to 2g in Table 2.2. It can be seen that, at $Ro \approx 1$, Nu increases with increasing radius and with increasing Grashof number.

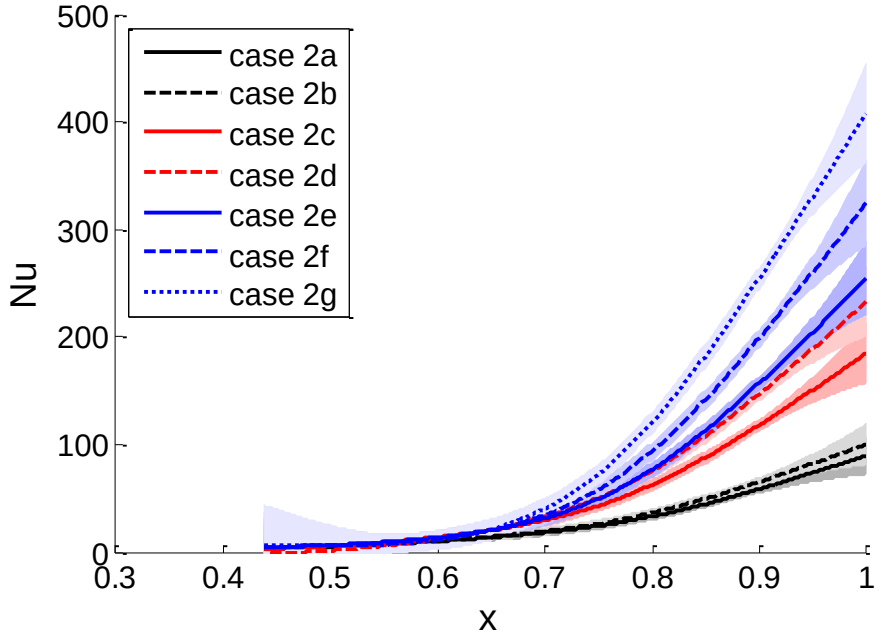

Fig. 2.26 Radial distribution of Nusselt numbers by Tang et al. [2015]

2.4 CFD

Tucker [1993] and *Long and Tucker [1994b]* used 3-D unsteady laminar CFD on a heated rotating cavity similar to the rig used by *Farthing et al. [1992b]* (Rig a) with $a/b = 0.1$ and $G = 0.267$ for fairly low values of axial and rotational Reynolds numbers ($Re_z = 2180$ and $Re_\phi = 1.3 \times 10^4$). The two discs were heated symmetrically and four different temperature profiles with approximately the same maximum temperatures at different radii were investigated. The calculated flow structure showed that flow entered the cavity in one or more radial arm and then formed regions of cyclonic and anticyclonic circulation, which was consistent with the observation by *Farthing et al. [1992b]*. In addition, the flow was unsteady and underwent periodic changes of the number of the radial arms. Moreover, the flow structure was affected by the shape of the disc temperature: the number of 'radial arms' and circulation pairs increased from one to three as the maximum disc temperature moved radially outward.

Long et al. [1997] applied 2-D and 3-D unsteady CFD using a mixing length turbulence model to predict the flow and heat transfer in two rotating cavity rigs (rig (a) was used by *Long*

[1994] and rig (b) was used by *Tucker [1993]*). Only 3-D calculations were made for to rig (a), for $x_a = 0.1$, $G = 0.13$, $Re_z = 2 \times 10^3$ and $Re_\phi = 2 \times 10^5$; both 2D and 3D calculations were made for rig(b), for $x_a = 0.29$, $G = 0.25$, $Re_z = 2 \times 10^4$ and $Re_\phi = 3 \times 10^6$. It was shown that the 2-D axisymmetric solution could not model the rotating cavity flow faithfully. The 3-D calculation for rig (a) predicted the trend of the Nusselt number distribution but underpredicted the magnitude. The agreement between the prediction and the experiments for rig(b) was less satisfactory.

Sun et al. [2004] used 3-D unsteady CFD to simulate the buoyancy-induced flow in the closed rotating cavity B used by *Bohn et al. [1995]*, for $G = 0.50$, $x_a = 0.52$ and $1.95 \times 10^8 < Ra' < 1.10 \times 10^{10}$, with no Reynolds averaging or turbulence modelling. Good agreement between the calculated Nusselt numbers and the experimental values was obtained.

Tian et al. [2004] implemented 3-D steady CFD calculations with low Reynolds k-ε turbulence model on the flow in a rotating cavity with axial throughflow and without inner shaft, for $x_a = 0.229$ and $G = 0.229$. The isothermal case and the cases with heated shroud and adiabatic discs were studied. The range of the working conditions was $\beta\Delta T = 0 \; or \; 0.17, Re_z = 5.4 \times 10^4$ and $0.958 < Ro < 40$. The numerical results showed that, under isothermal conditions, the flow in the cavity was axisymmetric and stable, and the region for the toroidal vortex was indicated correctly. The vortex became weaker as Ro decreased. There was a critical Rayleigh number (approximately at $Ra = 6.583 \times 10^5$), above which the flow became non-axisymmetric and time-dependent. It was suggested that the flow could be divided into two parts: buoyancy-induced flow in the outer region and toroidal vortex in the inner region. In *Tian et al. [2008]*, similar CFD calculations captured the flow structures with one, two, three and four pairs of vortices. It was shown that the number of vortex pairs decreased as Re_ϕ and Gr increased and as Re_z decreased.

Bohn et al. [2006] performed 3-D unsteady laminar CFD simulations for one experimental case by *Bohn et al. [2000]* at $Re_z = 2 \times 10^4$ and $Re_\phi = 2 \times 10^5$ (case 4 in Table 2.1). Similar flow structure to the experimental observation was obtained. The numerical results also revealed a flow pattern changing periodically between single, double and triple pairs of circulations (Fig. 2.27).

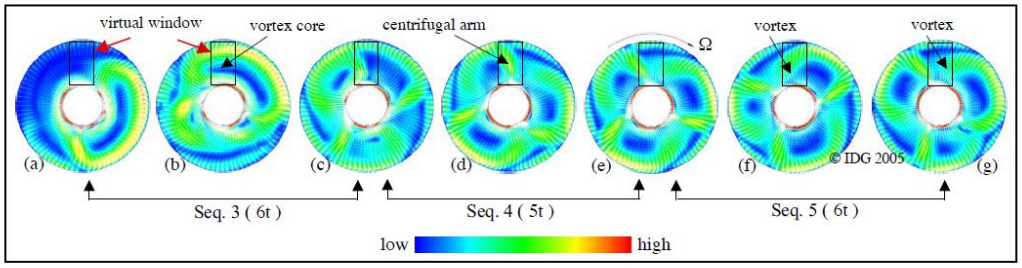

Fig. 2.27 Computed flow structure in the core of a heated rotating cavity with axial throughflow from Bohn et al. [2006]

Owen et al. [2007] made 3-D unsteady CFD computations using the renormalized group (RNG) k-ε turbulence model to experiments 2, 5 and 6 in *Owen and Powell [2006]*. For experiment 2, $Re_z = 3.03 \times 10^3$ and $Re_\phi = 4.3 \times 10^5$; for experiment 5, $Re_z = 1.64 \times 10^3$ and $Re_\phi = 1.57 \times 10^6$; for experiments 6, $Re_z = 1.73 \times 10^3$ and $Re_\phi = 1.63 \times 10^6$. The numerical results illustrated the multi-cell flow structure. Fig. 2.28 shows the comparison between the predicted $V_\phi/\Omega r$ and the measurements. Reasonable agreement was obtained for experiment 2, but the values for experiments 5 and 6 were overpredicted.

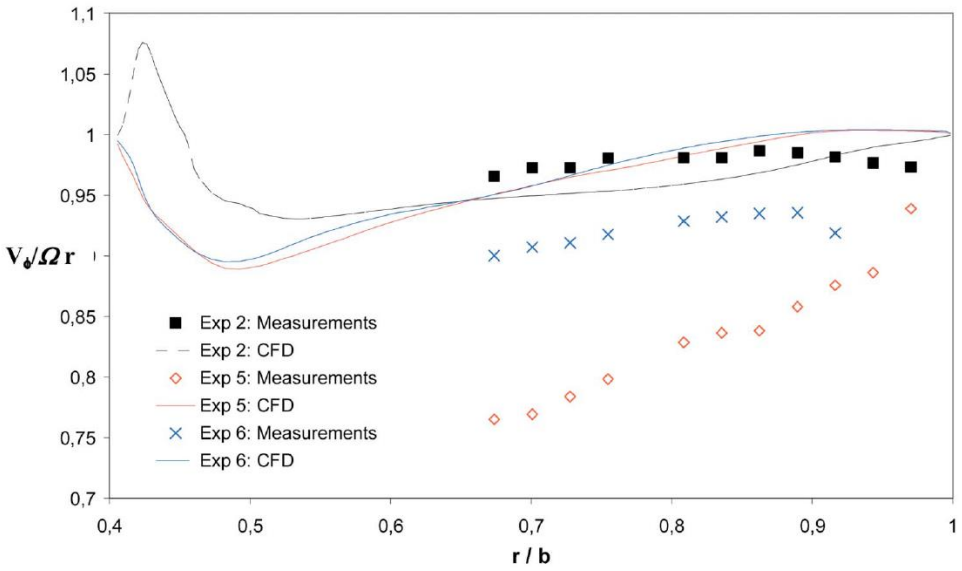

Experiment 2: $Re_\phi = 0.43 \times 10^6, Re_z = 0.303 \times 10^4$, experiment 5: $Re_\phi = 1.57 \times 10^6, Re_z = 0.164 \times 10^4$ and experiments 6: $Re_\phi = 1.63 \times 10^6, Re_z = 0.173 \times 10^4$

Fig. 2.28 Comparison of radial distribution of $V_\phi/\Omega r$ between CFD and experiment (Owen et al. [2007])

Sun et al. [2007] compared their 3-D unsteady large eddy simulations (LES) and 3-D unsteady RANS (using RNG k-ε turbulence model) solutions to the experiments by *Alexious [2000]* and *Long et al. [2003]* for an engine-representative multi-cavity rig. Fig. 2.29 shows the schematic of the cavity which is the instrumented cavity of build 2 in *Long et al. [2003]*. In Fig. 2.30, the calculated shroud Nusselt numbers and the calculated ratios of the relative tangential velocity to the disc velocity ($\frac{V_\phi - \Omega r}{\Omega r}$) using LES and RANS were compared to the experimental measurements at one case where $Re_z = 1.53 \times 10^5, Re_\phi = 1.29 \times 10^6, Ro = 4.04, \beta\Delta T = 0.19$ (the experimental Re_ϕ was slightly lower, but it didn't affect the comparison.) It was shown that the core flow rotated slower than the disc and that both the velocity and the shroud Nusselt numbers were well predicted by LES but underpredicted by RANS.

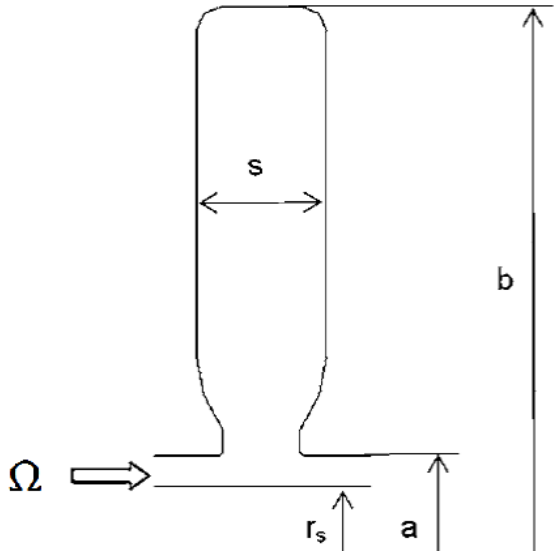

Fig. 2.29 Schematic of the rotating cavity used by Sun et al. [2007]

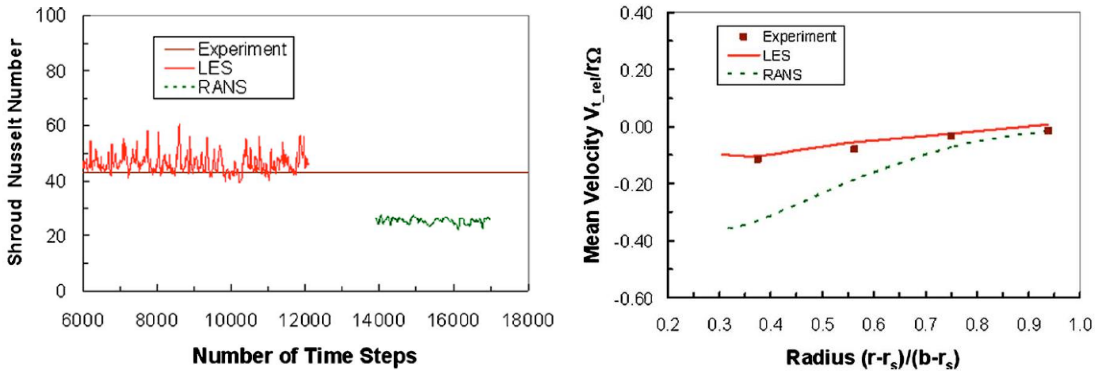

Fig. 2.30 Comparison of shroud Nusselt numbers (left) and velocity measurements ($V_\phi/\Omega r$ - *1*) (right) between LES, RANS, and experiment (Sun et al. [2007])

Tan et al. [2009] applied 3-D CFD simulations on cases 2-4 of *Bohn et al. [2000]* (See Table 2.1) using a steady RANS method, an unsteady RANS method and LES. For the unsteady RANS method, it was shown that the standard k-ε model with an enhanced wall treatment gave the best results. The flow structure and the radial distributions of the Nusselt numbers for all the methods were compared. The unsteady RANS and LES could capture the flow structure and the heat transfer well, but steady RANS failed to obtain a reasonable flow structure but provided acceptable prediction of the heat transfer. The expenses for the three methods were also

compared. It took 4 hours and 30 hours to calculate one case using steady and unsteady RANS respectively, while it cost 840 hours using LES.

Tian and Zhu [2012] used 3-D unsteady RANS calculation using RNG k-ε model on case 2 and case 4 in *Bohn et al. [2000]* (see Table 2.1). Two different models were applied. For model 1, only the fluid domain was solved, temperature profiles were given to the two radial walls of the fluid domain and the outer wall was set to be isothermal with the maximum temperature; for model 2, the fluid domain with thick-walled adiabatic discs and isothermal shroud were solved simultaneously. There was little difference between the results for the two models. All the calculations obtained good agreement with the experimental Nusselt numbers. It took about one and eight weeks on a PC cluster of 8 CPUs to calculate case 4 using model 1 and model 2 respectively.

Tan et al. [2014] made 3-D unsteady CFD calculations on case 4 in Table 2.1 using the finite volume method, the discontinuous Galerkin method and laminar/Spalart-Allmaras turbulence model /SST transition model. The comparison demonstrated that the transition turbulence model fitted the experimental Nusselt numbers better. The laminar results for the downstream disc were the closest prediction to the experimental data but that for the upstream disc overpredicted the experimental value.

Atkins and Kanjirakkad [2014] also used 3-D unsteady hybrid RANS/LES CFD method (standard Spalart-Allmaras RANS layers for near wall modelling and LES for region away from the walls) to illustrate the flow structure of the rotating cavities for two cases at $Re_\phi = 3.1 \times 10^6, Re_z = 1.1 \times 10^5, \beta\Delta T = 0.15$ and 0.32 (cases 4a and 4b in Table 2.2). Each solution took 10 days on 16 GPUs (1 GPU was roughly equivalent to 20 CPUs). Fig. 2.31 showed the radial velocity on the mid cavity face for the two cases. As it can be seen, with $\beta\Delta T$increased, the flow turned from relatively stable stratification to unstable Rayleigh-Bénard like structure and the mixture of the cavity flow and axial flow was enhanced.

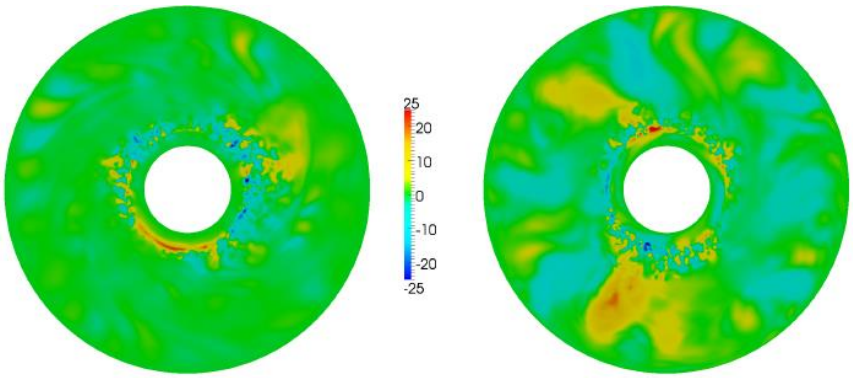

Left side: Ro = 0.58, $Re_z = 1.1\times10^5$, $Re_\phi = 3.5\times10^6$, $\beta\Delta T = 0.15$; right side: Ro = 0.65, $Re_z = 1.1\times10^5$, $Re_\phi = 3.1\times10^6$, $\beta\Delta T = 0.32$

Fig. 2.31 CFD results of V_r for two cases of Aktins and Kanjirakkad [2014]

Pitz et al. [2016] did 3-D direct numerical simulation (DNS) using a spectral element-Fourier method on the buoyancy induced flow in the closed cavity B used by *Bohn et al. [1995]*($G = 0.50, x_a = 0.52$). The calculations took 7 days to reach a statistically steady state using 64 processors. The range of Ra' for the calculation was $10^{5.5} \leq Ra' \leq 10^9$. It was shown that, when the traditional Boussinesq approximation was used, the calculated Nusselt numbers were much higher than the measurements, but they were close to the correlation proposed by *Hollands et al. [1975]* for natural convection in a rectangular enclosure heated below. When the extended Boussinesq approximation, which was proposed by *Lopez et al. [2012]*, was used, the calculated Nusselt numbers agreed well with the experiments.

Chapter 3 – Statistical Method for Solving Inverse Problems

Experiments by *Atkins and Kanjirakkad [2014]* and *Puttock-Brown [2016]* will be used to study the heat transfer in rotating cavities. In these experiments, heat transfer parameters, for example, Nusselt numbers (Nu) or Biot numbers (Bi), cannot be measured directly and are usually calculated from temperature measurements. The temperature measurements and the heat transfer parameters are referred to as the ***observation*** and the ***parameters*** of a heat transfer problem respectively. Analysing the temperature measurements corresponds to calculating the parameters from the observation, which is referred to as an ***inverse problem***. The observation or the experimental data, which is usually of random experimental errors, can be interpreted and analysed statistically. Therefore, this chapter introduces a statistical process for solving the inverse problem in this thesis, that is, calculating Nusselt numbers or Biot numbers from disc temperature measurements.

First, the definition of the general inverse problem is introduced and then the specific inverse problem for this thesis is stated. Next, the fundamental theory for solving inverse problems – Bayes' theorem – is presented and expressed in terms of the specific problem here. After that, one of the most commonly-used statistical methods – the Bayesian method – is illustrated and the typical form of the Bayesian terms are presented. Finally, brief ideas of using this method to solve the inverse heat transfer problem for rotating cavities are discussed.

3.1 Inverse problem

The inverse problem is defined as the reverse process of a ***forward problem*** or ***direct problem***. The ***forward problem*** is the process of calculating data based on some physical or mathematical models with given parameters. It can be illustrated schematically in Fig. 3.1.

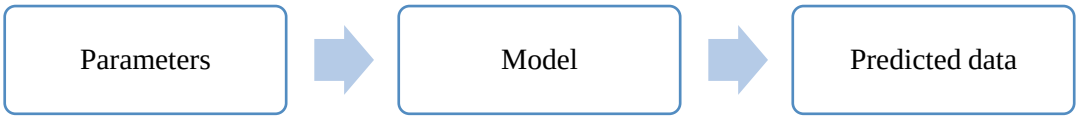

Fig. 3.1 Forward problem

The inverse process of the forward problem is called the ***inverse problem***, which is depicted in Fig. 3.2.

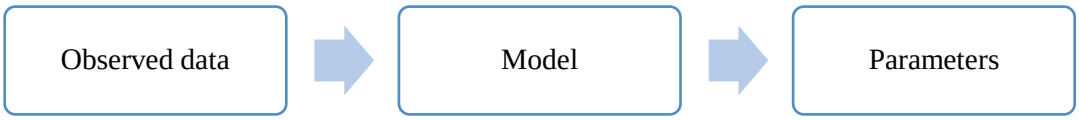

Fig. 3.2 Inverse problem

The observed data or the observation, the parameters and the model all vary with problems. For the inverse problem in this thesis, the heat convection in rotating cavities, which is quantified by Nusselt numbers (Nu), or equivalently, Biot numbers (Bi), are estimated from the temperature measurements on rotating discs. So the temperature measurements are the observation, the Nusselt numbers or the Biot numbers are the parameters, and the conduction model on rotating discs will be the model. This is a typical inverse heat transfer problem and it can be illustrated by Fig. 3.3.

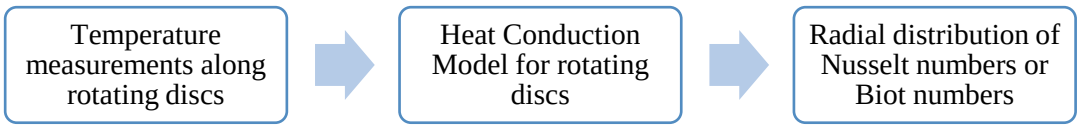

Fig. 3.3 Inverse problem for heat transfer in rotating cavities

As mentioned before, the temperature measurements can be treated as experimental data which have random experimental errors, so they can be interpreted statistically using probability theory. Thus the theorem of inverse probability – the Bayes' theorem – could be used.

3.2 Bayes' theorem

The Bayes' theorem is the fundamental of the statistical interpretation of inverse problems. This theorem can be found in most statistical books (For example *O'Hagan [1994]* and *Kaipio and Somersalo [2006]*). The general formula of this theorem is given in Eq. (3.1).

Considering two related events, A and B, the Bayes' theorem can be written as

$$P(A)P(B|A) = P(B)P(A|B) \tag{3.1}$$

It can be rearranged as

$$P(B|A) = \frac{P(B)P(A|B)}{P(A)} \tag{3.2}$$

The formula can be interpreted in the following way: if we are interested in event B but we observed event A, when the *prior probability* of event B ($P(B)$), the information of how event A depends on event B ($P(A|B)$) and the probability of event A ($P(A)$) are provided, we could estimate how likely B is when A is known, i.e., $P(B|A)$.

Considering the inverse problem of heat transfer in rotating cavities in this thesis, what we are interested in is the heat transfer parameters Nu or Bi, and what we observed is the solid surface temperature measurements, Θ. Therefore event A in Eq. (3.2) will be the observed Θ which is denoted as Θ_{exp} and event B will be the unknown heat transfer parameters Nu or Bi, which are denoted as Φ here. So the Bayes' theorem can be rewritten in terms of the inverse heat transfer problem here in Eq. (3.3).

$$P\left(\Phi\middle|\Theta_{exp}\right) = \frac{P(\Phi)P(\Theta_{exp}|\Phi)}{P(\Theta_{exp})} \tag{3.3}$$

As mentioned before, Θ are the temperature measurements which have random experimental errors, so Θ can be treated as independent continuous random variables. Therefore, the probability distributions of Θ can be expressed in terms of probability densities. Φ are unknown

and can also be constructed as continuous random variables with probability density distributions. So all the terms in Eq. (3.3) can be expressed as probability densities (*Kaipio and Somersalo*). If the probability density distribution is denoted as p, the ***Bayes' theorem of inverse problems*** can be written as

$$p(\Phi|\Theta_{exp}) = \frac{p(\Phi)p(\Theta_{exp}|\Phi)}{p(\Theta_{exp})} \tag{3.4}$$

where $p(\Phi|\Theta_{exp})$ is called the ***posterior distribution***, which expresses the probability of Φ out of the observation Θ_{exp}; $p(\Phi)$ is the ***prior probability density function*** of heat transfer parameters Φ, and it expresses what we know about the unknown parameters prior to the experiment; $p(\Theta_{exp}|\Phi)$ is called the ***likelihood function*** as it expresses the likelihood of the different measurements with Φ given. The denominator $p(\Theta_{exp})$ is a weighted average of the likelihood $p(\Theta_{exp}|\Phi)$ with weights being the prior probability density function $p(\Phi)$. It can be calculated using Eq. (3.5).

$$p(\Theta_{exp}) = \int p(\Phi)p(\Theta_{exp}|\Phi)d\Phi \tag{3.5}$$

Eq. (3.4) forms the Bayesian framework. Construction of the framework to find the targeted conditional probability distribution (or the posterior distribution) – $p(\Phi|\Theta_{exp})$– is called the ***Bayesian method*** (*Kaipio and Somersalo*).

3.3 Bayesian method

In the last section, the essentials for the Bayesian method are introduced. Here the process to apply the Bayesian method is discussed.

According to *Kaipio and Somersalo*, the denominator $p(\Theta_{exp})$ in Eq. (3.4) plays the role of a norming constant and it is usually of little importance. Therefore, Eq. (3.6) can be used in the Bayesian method.

$$p(\Phi|\Theta_{exp}) \propto p(\Phi)p(\Theta_{exp}|\Phi) \tag{3.6}$$

Thus the Bayesian method applied to the inverse heat transfer problem in this thesis comprises the following three steps:

1. Based on all the known information of the heat transfer parameters, find a prior probability density $p(\Phi)$.
2. According to the knowledge on the heat transfer experiments, construct the likelihood density function $p(\Theta_{exp}|\Phi)$ that describes the interrelation between the temperature measurements and the heat transfer parameters.
3. Use an appropriate method to explore the posterior probability density $p(\Phi|\Theta_{exp})$, e.g., finding out what are the most probable values of Φ and estimating the 95% confidence intervals for the estimated Φ.

3.3.1 Estimator

Step 3 of the Bayesian method is to explore the posterior probability density $p(\Phi|\Theta_{exp})$. There are two commonly used estimators to find the most probable values of Φ:

1. Posterior mean of Φ ;
2. Maximizing a posteriori $(\Phi|\Theta_{exp})$.

If the number of unknown parameters are small, it is possible to get the full picture of $p(\Phi|\Theta_{exp})$ to calculate the posterior mean of Φ using Eq. (3.4). However, if there are many unknown parameters, the feasible way will be calculating $p(\Phi|\Theta_{exp})$ at discrete points to find the optimum solution, which is referred to as ***maximum a posteriori (MAP).*** This process can be expressed as

$$\Phi_{MAP} = \arg\max_{\Phi} p(\Phi|\Theta_{exp}) \tag{3.7}$$

Numerical optimisation methods are usually employed to obtain this maximum. This will be introduced in detail in Chapter 4.

3.3.2 Likelihood function

The likelihood function $p(\Theta_{exp}|\Phi)$ can be regarded as the function of Φ for Θ_{exp}, or, the process of generating temperature data from given Φ. It is usually assumed that the temperatures are measured independently and that they have random experimental errors above the true values of Θ. Thus the distribution of Θ_{exp} is

$$\Theta_{exp} \sim \mathcal{N}(\Theta_{true}, \epsilon^2) \tag{3.8}$$

where ϵ is the standard deviation of the random experimental error. In Eq. (3.8), Θ_{true} is related to the parameters Φ. Hence the forward model is needed to calculate the true Θ from Φ. So in some literature (for example, *Gnanasekaran and Balaji [2011]*), the likelihood function is also called the forward model. The relationship of Θ_{true} to Φ can be denoted as $\Theta(\Phi)$. Then the likelihood function for the heat transfer problems can be written in the general form:

$$p(\Theta_{exp}|\Phi) = \frac{1}{(2\pi\epsilon^2)^{M/2}} exp\left(-\frac{\sum_{j=1}^{M}\left(\Theta_{exp,j} - \Theta(\Phi)_j\right)^2}{2\epsilon^2}\right). \tag{3.9}$$

where M is the number of the experimental measurements.

The form of $\Theta(\Phi)$ varies with problems. For the heat transfer in rotating cavities, the steady temperature measurements on the rotating disc are used to calculate the Nusselt number distribution, so the forward model should be the steady conduction model for the disc.

3.3.3 Prior density function

The form of the prior density function also varies from case to case. The most common used form of the prior density function is the normal distribution and it is usually called the '***Gaussian prior***'. Based on the prior information of the parameter set Φ, the mean value $\bar{\Phi}$ and the

covariance matrix C can be constructed into the Gaussian prior, then the general normal distribution form of the prior density function can be written as

$$p(\Phi) = \frac{1}{(2\pi)^{N/2}|C|^{1/2}} exp\left(-\frac{1}{2}(\Phi - \bar{\Phi})^T C^{-1}(\Phi - \bar{\Phi})\right). \quad (3.10)$$

where N is length of the vector Φ, or, the number of parameters and the covariance matrix C has $N \times N$ entries. $|C|$ is the determinant of the covariance matrix C.

When the prior information of Φ is not required for an inverse problem, a uniform prior could be used, which means the probabilities for all possible values of Φ are identical. In this condition the Bayesian method Eq. (3.6) could be reduced to

$$p(\Phi|\Theta_{exp}) \propto p(\Theta_{exp}|\Phi). \quad (3.11)$$

Thus maximizing the posteriori will be equivalent to maximizing the likelihood function. The process is referred to as ***Maximum Likelihood Estimation (MLE)*** *and* it is a classic statistical method (*Kaipio and Somersalo [2006]*). This method is used by the author in *Cho et al. [2016]* to estimate heat transfer parameters from transient heat transfer experiments in a wind tunnel and in a 1.5 stage rotor-stator rig. It is often treated as a non-Bayesian statistical method, but as shown in Eq. (3.11), it can be related to the Bayesian method and it coincides with the MAP of the Bayesian for a uniform prior distribution. This also shows the flexibility of the Bayesian method.

3.4 Application of Bayesian method

To illustrate the heat convection in rotating cavities, the temperature measurements of *Atkins and Kanjirakkad* are analysed to calculate the Nusselt numbers. As discussed in Section 3.1, this is a typical inverse problem. Section 3.3 shows that the Bayesian method can be employed to solve this inverse problem and that there are three mains steps to apply this method. For these three steps, Eq. (3.10) can be used as the prior density function, Eq. (3.9) can be used in

conjunction with the conduction equation for the rotating discs to construct the likelihood function, and MAP (Eq. (3.7)) can be used as the estimator. For the prior density function, the prior information of the Nusselt numbers (or Biot numbers) is required to assume the appropriate mean value $\overline{\Phi}$ and covariance matrix *C*. For the heat transfer in rotating cavities, a profile of Nusselt numbers will be obtained and it should be physically smooth. The smoothness of the Nusselt numbers could be constructed in the form of the Gaussian Prior (Eq. (3.10)), and then it could be included in the process of MAP. The detailed form of the Prior function will be shown in Section 4.3 where the Matérn covariance is used for smoothing Nusselt numbers. The Bayesian method can only be applied if a forward model to connect Φ to $\Theta - \Theta(\Phi)$ – is provided for the likelihood function. Chapter 4 will use the fin equation to model the conduction on rotating discs, so the fin equation can be used as the forward model. After that, the MAP point, namely, the optimum Nusselt numbers or Biot numbers, can be computed. The detailed application and examples will be shown in Chapter 4.

3.5 Summary

The inverse problem in this thesis is to calculate Nusselt numbers from temperature measurements along rotating discs. To solve this inverse heat transfer problem, starting from the definition of the inverse problem and its fundamental statistical theory, a statistical process, which is referred to as the Bayesian method, is provided. Three main steps to apply this Bayesian method and the key ideas to apply this method to experiments are described. The detailed application will be shown in Section 4.3 and 4.4.

Chapter 4 – Circular Fin Equation

Prediction of the disc temperature involves calculation of the conduction on the disc and the convection in the cavity flow. Thus this chapter is to show how the conduction in compressor discs is modelled. The compressor discs are usually relatively thin and, from the measurements of *Atkins and Kanjirakkad [2014]* (see Fig. 2.25), the axial temperature differences are much smaller than the radial ones. Therefore, in principal, the 1-D circular fin equation could be used. The fin equation connects the disc temperature to the heat convection from the cavity, which can be quantified by Nusselt numbers (Nu), or equivalently, Biot numbers (Bi). Therefore, there are two ways to apply the fin equation: When Nusselt numbers are given, the fin equation can be used to calculate disc temperatures, which is called the ***direct solution*** of the fin equation; When Nusselt numbers are unknown, the fin equation can be solved inversely to estimate Nu from disc temperatures, and this is a typical inverse problem and referred to as the ***inverse solution***. The direct solution is accurate, or statistically called, well-conditioned, while the inverse solution will cause large uncertainty on Nu and it is statistically described as 'ill-conditioned'.

The fin equation is introduced in Section 4.1: the fin equation for compressor discs is deduced; the two different boundary conditions are presented; the direct and the inverse solution of the fin equation are introduced. In Section 4.2, the fin equation is solved directly. Both the analytical solution and the numerical solution are presented. The analytical solution exists when the thickness, the thermal conductivity and the Biot numbers are constant along the radius. The analytical solutions at different Biot numbers are used to illustrate the effects of the convection on disc temperatures. For general use of the fin equation, a numerical scheme is required. It is validated by the analytical solution and the energy balance checking. The fin equation is solved

inversely to calculate Nusselt numbers from the measurements of the disc temperatures. In Section 4.3, the Bayesian method, which is introduced in Chapter 3, is adopted to solve this inverse problem. First, its ill-conditioned nature is shown. Then the Bayesian method is applied. Next, it is validated by the simulated experiments. In Section 4.4, the inverse solution using the Bayesian method is applied to temperature measurements of *Atkins and Kanjirakkad* in a multi-cavity rig, and the results are discussed.

4.1 Fin equation

4.1.1 Derivation of fin equation for compressor discs

The derivation of the 1D fin equation can be found in most heat transfer text books (for example, *Incropera and Dewitt [1996]*). The general form can be expressed as

$$\frac{d}{dr}\left(k_s A \frac{dT_o}{dr}\right) - h\left(T_o - T_{ref}\right)\frac{dS}{dr} = 0 \tag{4.1}$$

where A and S are the cross-sectional and surface areas respectively, T_o is the surface temperature, T_{ref} is the appropriate reference temperature, h is the heat transfer coefficient based on T_{ref} ($h = q_o/(T_o - T_{ref})$) and k_s is the solid thermal conductivity.

Fig. 4.1 shows a simplified version of the rotating disc used by *Atkins and Kanjirakkad* with varying thickness t and inner and outer radii a and b. (For simplicity, there is no fillet at $r = b$.)

It follows that

$$A = 2\pi r t \tag{4.2}$$

$$dS = 4\pi r dr / \sin\alpha \tag{4.3}$$

where α is the angle of the gradient of the disc surface and t is the thickness of the disc. Both α and t vary with radius.

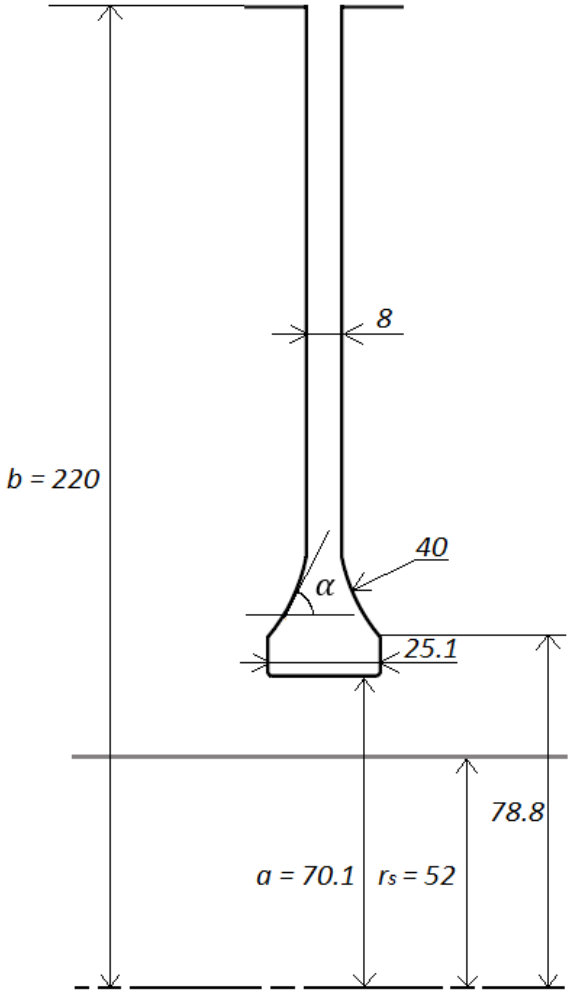

Fig. 4.1 Simplified diagram of instrumented disc of Atkins and Kanjirakkad [2014] (Dimension in mm).

From Fig. 4.1, it can be seen that the greater part of the rotating disc is relatively thin. Moreover, in the experiments by *Atkins and Kanjirakkad* (also see Fig. 2.25), the axial temperature difference between the two radial disc surfaces was negligible compared to the radial differences. So in principle, the fin equation can be employed to model the heat transfer on rotating discs. The variety of the thermal conductivity and the geometry of the disc needs to be taken into account, so the general form of the fin equation is required, which is presented as Eq. (4.4). Note: t is treated as a function of radius r, k_s is regarded as a function of temperature,

that is, $k_s = f(T_o)$, and the temperature in axial through flow, T_f, is used as the reference temperature, i.e. $T_{ref} = T_f$.

$$\frac{d^2T_o}{dr^2} + \left(\frac{1}{r} - \frac{2}{t}\frac{cos\alpha}{sin\alpha} + \frac{1}{k_s}\frac{dk_s}{dT_o}\frac{dT_o}{dr}\right)\frac{dT_o}{dr} - \frac{2h}{k_s t sin\alpha}\left(T_o - T_f\right) = 0 \tag{4.4}$$

In the rig used by *Atkin and Kanjirakkad*, the discs were made from a titanium Alloy (Ti-6Al-4V), the thermal conductivity of which is given in Table 4.1.

Temperature $T_o[K]$	Thermal conductivity k_s $[Wm^{-1}K^{-1}]$
293	6.6
366	7.3
478	9.1

Table 4.1 Thermal conductivity of Ti-6Al-4V

The non-dimensional temperature, radial location and disc thickness and Biot number can be defined as following:

$$\Theta = \frac{T_o - T_f}{T_{o,b} - T_f} \tag{4.5}$$

$$x = \frac{r}{b}, \tau = \frac{t}{2b} \tag{4.6}$$

$$Bi = \frac{h_f b}{k_s} \tag{4.7}$$

where $T_{o,b}$ is the disc temperature at the outer radius of the disc and $h_f = q_o/(T_o - T_f)$.

So Eq. (4.4) can be rewritten in the non-dimensional form as

$$\frac{d^2\Theta}{dx^2}+\left(\frac{1}{x}-\frac{2}{\tau}\frac{cos\alpha}{sin\alpha}+\frac{1}{k_s}\frac{dk_s}{d\Theta}\frac{d\Theta}{dx}\right)\frac{d\Theta}{dx}-\frac{Bi}{\tau sin\alpha}\Theta=0 \tag{4.8}$$

This is referred to as the ***general fin equation***.

The Biot number, Bi, denotes the relative importance of convection compared with conduction within the disc. The Nusselt number (Nu_f), which denotes the strength of convection over conduction of the air can be worked out from Bi through Eq. (4.9) and Eq. (4.10).

$$Nu=\frac{h_f r}{k} \tag{4.9}$$

$$Nu=\frac{k_s}{k_f}xBi \tag{4.10}$$

When the thickness t and thermal conductivity k_s are constant (and hence $\alpha=\pi/2$), the general non-dimensional fin equation Eq. (4.8) reduces to the ***special fin equation***:

$$\frac{d^2\Theta}{dx^2}+\frac{1}{x}\frac{d\Theta}{dx}-Bi^*\Theta=0 \tag{4.11}$$

where Bi^* is the modified Biot number:

$$Bi^*=\frac{2b^2h_f}{k_s t}=\frac{2b}{t}Bi \tag{4.12}$$

Eq. (4.11) was used in *Tang et al. [2015]* for the diaphragm section (constant thin thickness section) of the disc.

4.1.2 Boundary conditions

To solve the fin equation for rotating discs, the boundary conditions at both ends of the disc are required. In this thesis, the fin equation is applied to the whole disc. So both the boundary conditions at $x=x_a$ and $x=x_b=1$ are needed. The boundary condition at $x=1$ is quite straightforward: as the $T_{o,b}$ is always given, by definition, $\Theta=\Theta_b=(T_{o,b}-T_f)/(T_{o,b}-T_f)=1$. While at $x=x_a$, different kinds of boundary conditions should be discussed.

1. Temperature boundary condition

If the temperature at $r = a$ is known, the first kind of the boundary condition, the temperature boundary condition, could be used. This could be shown as: at $x = x_a$, $\Theta = \Theta_a = (T_{o,a} - T_f)/(T_{o,b} - T_f)$.

2. Convective boundary condition

When the temperature at the inner radius of the disc is unknown, but the heat transfer between the inner surface of the disc and the axial throughflow is known as convection, Θ_a can be computed using the convective boundary condition. The convective boundary condition can be illustrated as

$$h_a\,(T_{o,a} - T_f) = k_s \frac{dT_o}{dr}|_{r=a} \tag{4.13}$$

where h_a is the heat transfer coefficients between the cob and the axial throughflow and T_f here is the temperature of the throughflow below the cob. The nondimensional form of Eq. (4.13) will be

$$\frac{h_a b}{k_s}\Theta_a = \frac{d\Theta}{dx}|_{x=x_a} \tag{4.14}$$

4.1.3 Direct and inverse solutions

The fin equation connects the disc temperature Θ and the heat convection on the disc (Bi or Nu). Depending on which of them is unknown, there are two paths to solve the fin equation, which can be illustrated by Fig. 4.2.

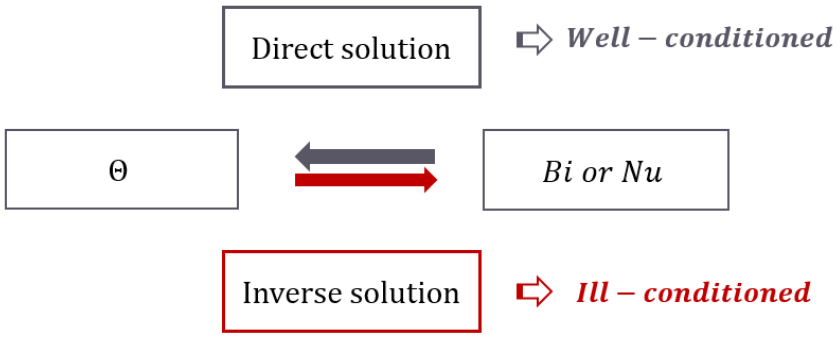

Fig. 4.2 Direct and inverse solutions of the fin equation

When Bi(or Nu) is known, the unknown temperature Θ can be calculated. As mentioned in Chapter 3, this process is straightforward and accurate and it is statistically called a well-posed or well-conditioned problem. It is referred to as the ***direct solution*** of the fin equation. The detail will be discussed in Section 4.2.

When Bi is unknown and needs to be calculated from the known disc temperature Θ, it is no longer a well-posed process and it is an ill-posed or ill-conditioned inverse problem, which means a small error in Θ will result in much larger errors in Bi. This process is referred to as the ***inverse solution*** of the fin equation. To obtain reliable results, the ill-conditioned problem needs to be solved through additional assumptions, such as assuming a specific form for the solution or, more generally, giving the smoothness of the solution. This can be realized by the Bayesian method and it will be shown in detail in Section 4.3.

4.2 Direct solution

There are analytical direct solutions for the special fin equation Eq. (4.11) when Bi^* is constant along the disc. When Bi^* is known, the special fin equation could be solved directly to calculate disc temperatures Θ. By comparing analytical results of radial temperature profiles at different Biot numbers, it can be seen how the disc temperature is affected by the heat convection in rotating cavities.

In general cases, the heat flux, disc thickness and thermal conductivity all vary along the disc, so the general fin equation Eq. (4.8) needs to be solved. Thus a numerical method is required for solving the general fin equation. A finite central difference scheme will be employed for the general use of the fin equation. When Bi profiles are known, this numerical solution can be solved directly to calculate disc temperatures Θ. This process is accurate and reliable. This scheme is validated by comparing the results to the analytical solution.

4.2.1 Analytical solution

The special fin equation (Eq. (4.11)) is a modified form of Bessel's equation (*Chapman [1974]*). Hence for constant Bi^* numbers, there are analytical solutions:

$$\Theta = C_1 I_0(Bi^{*1/2}x) + C_2 K_0(Bi^{*1/2}x) \tag{4.15}$$

where C_1 and C_2 are constants and I_0 and K_0 are modified Bessel functions of the first and second kind with zero order.

When the temperature boundary conditions are used, which means $\Theta = \Theta_a$ at $x = x_a = a/b$ and $\Theta = \Theta_b$ at $x = x_b = 1$, it follows that

$$C_1 = \frac{K_0(Bi^{*1/2})\Theta_a - K_0(Bi^{*1/2}x_a)\Theta_b}{I_0(Bi^{*1/2}x_a)K_0(Bi^{*1/2}) - I_0(Bi^{*1/2})K_0(Bi^{*1/2}x_a)} \tag{4.16}$$

$$C_2 = \frac{I_0(Bi^{*1/2}x_a)\Theta_b - I_0(Bi^{*1/2})\Theta_a}{I_0(Bi^{*1/2}x_a)K_0(Bi^{*1/2}) - I_0(Bi^{*1/2})K_0(Bi^{*1/2}x_a)} \tag{4.17}$$

Similar forms can be deduced for the convective boundary condition. For simplicity, they are not presented here.

When the constant Bi^* is known, Eq. (4.15) can be used to calculate disc temperature profiles.

The heat convection, which is quantified by the Nusselt number, Nu, or the Biot number, Bi, determines the disc temperature through the fin equation. But how does it affect the temperature

profile? This can be illustrated by the analytical solution of the special fin equation at different Bi^*.

Fig. 4.3 shows the normalized variation of Θ v. x according to Eq. (4.15) for a range of modified Biot numbers with $\Theta_a = 0$ at $x_a = 0.3$ and $\Theta_b = 1$ at $x_b = 1$. From Fig. 4.3, it is shown that, with Bi^* increasing, the gradient near the outer radius increases, while that near the inner radius decreases. The effect of Bi^* on Θ is similar to that of Grashof number from Fig. 2.25, which indicates that stronger buoyancy effects lead to stronger convection and hence lower disc temperature and it could be quantified through the fin equation.

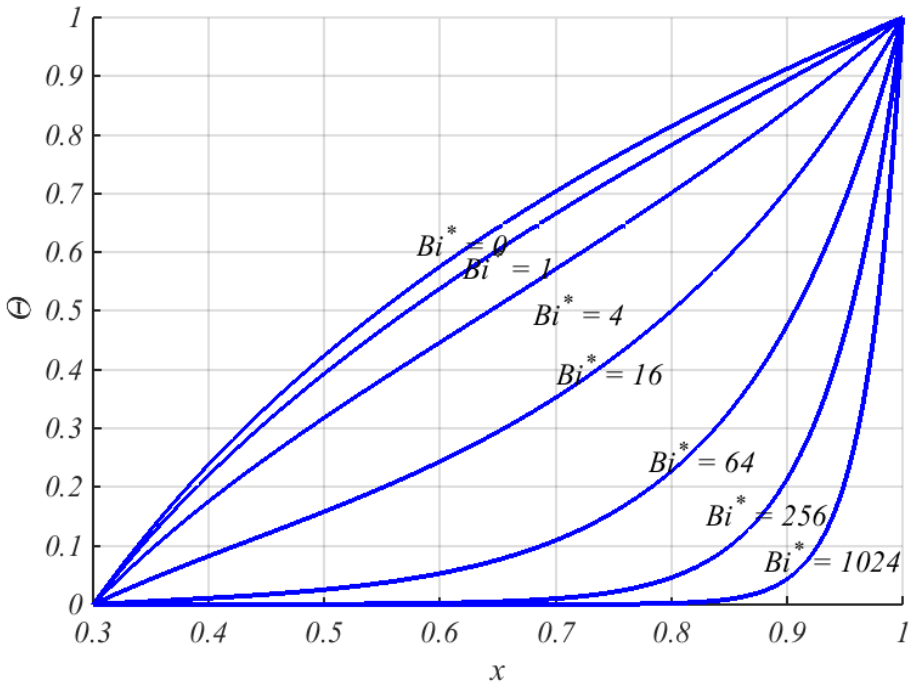

Fig. 4.3 Effect of Bi^* on theoretical variation of Θ *v.* x

4.2.2 Numerical solution

Section 4.2 solves the special fin equation with constant Bi^* analytically. However, in general, the Biot number, the disc geometry and the thermal properties all vary with radius. Therefore, the general fin equation (Eq. (4.8)) should be used. It can only be solved numerically.

The general fin equation presents a second-order, nonlinear, boundary-value problem. It can be approximated using second-order finite differences, which is shown in Eq. (4.18), where x_j for $j = 1, \dots, N$ denotes a grid of N uniformly-spaced grid points between $x = x_a$ and $x = 1$, and Δx is the constant step length. N is the total number of grid points.

$$\frac{\Theta_{j+1} - 2\Theta_j + \Theta_{j-1}}{\Delta x^2} + \left(\frac{1}{x_j} - \frac{2}{\tau_j}\frac{cos\,\alpha_j}{sin\,\alpha_j} + \frac{1}{k_s(\Theta_j)}\frac{k_s(\Theta_{j+1}) - k_s(\Theta_{j-1})}{2\Delta x}\right) \times \frac{\Theta_{j+1} - \Theta_{j-1}}{2\Delta x} - \frac{Bi_j}{\tau_j\,sin\,\alpha_j}\Theta_j = 0 \quad (2 \le j \le N-1) \tag{4.18}$$

As the efficiency of solving linear equations is much higher than that of solving non-linear ones, Eq. (4.18) is solved through tri-diagonal matrix method assuming initial thermal conductivities. Then it is solved iteratively until the temperature converges. The criterion of convergence (maximum of the difference of Θ between the last two iterations) is 10^{-6}.

The analytical solution of the special fin equation can be used to validate this discretized form. To solve both the special fin equation and the general fin equation directly, it is assumed that constant $Bi = 0.4$, constant $t = 0.008m$, b = 0.22 and constant $k_s = 7Wm^{-1}K^{-1}$. The boundary conditions are $\Theta_a = 0.1$ at $x_a = 0.3$ and $\Theta_b = 1$ at $x_b = 1$. Eq. 4.15 is used to calculate the analytical direct solution of the special fin equation. The same geometry and boundary conditions are assumed for Eq. (4.18) and N is taken to be 301. Fig. 4.4 compares the numerical results to the analytical solution. The differences between the numerical and analytical Θ are less than 10^{-4} and the energy balance of the integrated heat fluxes was checked with a relative error less than 2×10^{-4}.

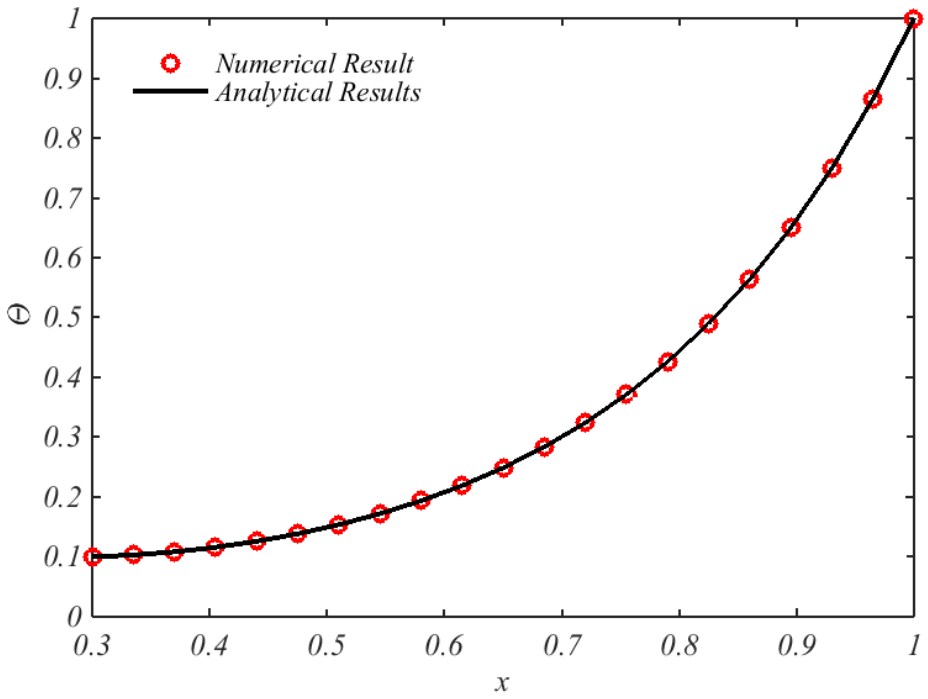

Fig. 4.4 Validation of numerical solution of the general fin equation (constant $Bi = 0.4$, $t = 0.008\ m$, constant $b = 0.22$ and constant $k_s = 7\ W/m/K$)

4.3 Inverse solution

In this section, firstly, the nature of the ill-conditioning of this inverse problem is illustrated, then the Bayesian method, which was introduced in Chapter 3, is employed to solve this inverse problem. Then, the Bayesian method is validated by 'simulated experiments'. In simulated experiments, the 'experimental temperatures' are generated by adding random noises to the 'true temperatures' which are calculated from the direct solution using Eq. (4.18). Then the Bayesian method is used to obtain Nu, or alternatively here, Bi, and its confidence intervals from the 'experimental temperatures'. The method is validated by comparing the calculated Bi to its true distribution. The results are also compared to that calculated from the conventional curve-fitting methods.

4.3.1 Illustration of the ill-conditioned nature

The straightforward way to solve the inverse solution is to rearrange Eq. (4.18) to calculate the local Bi values. To show the 'ill-conditioned' nature this process, 'simulated experiments' are used. A random noise of 0.005 is added to 21 uniformly distributed true temperature, which can be denoted as $\Theta_{exp} \sim \mathcal{N}(\Theta, 0.005)$. The same Bi values, disc geometry, thermal properties and boundary conditions with Section 4.2.2 are used. The noisy data are shown in Fig. 4.5a in red symbols. The calculated Bi profile from rearranging Eq. (4.18) are shown in Fig. 4.5b in red broken lines.

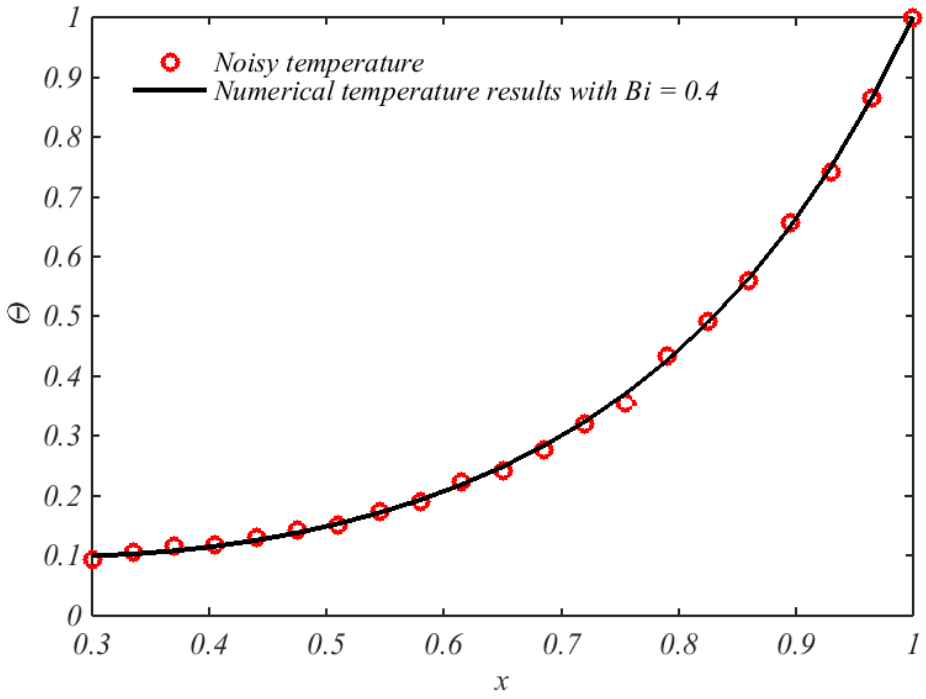

(a) Temperature

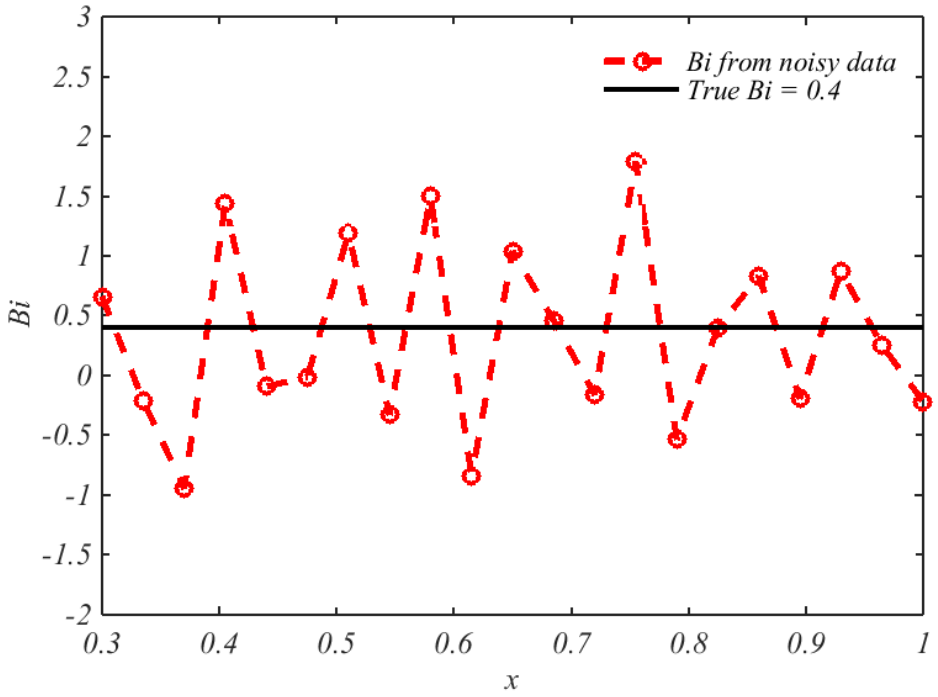

(b) Biot number

Fig. 4.5 Comparison of noisy temperature data and calculated Biot numbers with true values

From Fig. 4.5, it can be seen that small errors of temperature measurements can cause large errors in computed Biot numbers. This is a typical 'ill-conditioned' inverse problem for heat transfer experiments. Conventionally, the temperatures are smoothed with certain functions (e.g., polynomial functions) and then the Biot numbers are calculated from the smoothed temperatures using the fin equation. This approach, which is referred to as the 'curve-fitting method', will generate extra errors from smoothing and miss some information in temperatures, hence it will result in unreliable Biot number profiles.

Physically, the profiles of Biot numbers (or Nusselt numbers) correspond to the radial distribution of convection in rotating cavities, so the profiles of the Biot numbers should be smooth. Hence, instead of smoothing the temperature, it is more reasonable to assume the smoothness of the Biot number. The smoothness of the Biot number can be treated as known information of the parameters for this inverse problem. As mentioned in Chapter 3, the Bayesian

method is ideal for solving inverse problem with prior information. Therefore, it is employed here in conjunction with the fin equation to obtain the inverse solution. The detailed process will be introduced in Section 4.3.2.

4.3.2 Use of Bayesian method

This section is to recall the statistical theory of the Bayesian method introduced in Chapter 3 and to illustrate how this method is used for the inverse solution of the fin equation.

Bayes' theorem of inverse solution of fin equation

Eq. (3.4) shows the Bayes' theorem of inverse problems. For the inverse solution of the fin equation, that is, calculation Bi from Θ, the parameter Φ will be Bi. Then the form relating the observable Θ and the parameters Bi can be written as follows:

$$p(Bi|\Theta_{exp}) = \frac{p(\Theta_{exp}|Bi)p(Bi)}{p(\Theta_{exp})} \tag{4.19}$$

where, $p(Bi|\Theta_{exp})$ is the ***posterior probability density function*** of the non-observable Bi given the measurements of disc temperature Θ_{exp}. $p(Bi)$ is the ***prior probability density function*** of the non-observable heat transfer quantity -- Bi, where the known information about Bi prior to the experiments can be given. $p(\Theta_{exp}|Bi)$ is the ***likelihood function*** or the probability density distribution of temperature measurements Θ_{exp} given Bi, which describes the noisy or inaccurate relation between the measurements Θ_{exp} and the true temperatures. The true temperatures are calculated directly from Bi and can be denoted as $\Theta(Bi)$. According to Chapter 3, $p(\Theta_{exp})$ is the normalization constant and it can be given as

$$p(\Theta_{exp}) = \int p(\Theta_{exp}|Bi)p(Bi)\, dBi. \tag{4.20}$$

As discussed in Chapter 3, this constant is of little importance during the Bayesian approach. Then the equation for Bayesian method for the inverse solution of the fin equation can be written as

$$p\left(Bi\middle|\Theta_{exp}\right) \propto p(Bi)p(\Theta_{exp}|Bi) \tag{4.21}$$

Likelihood function

The likelihood function is the probability density distribution of Θ_{exp} given Bi. According to Section 3.3.2, the measurements are assumed to be normally distributed about the true temperature value, that is, $\Theta_{exp} \sim \mathcal{N}(\Theta(Bi),\ \epsilon^2)$. ϵ can be regarded as the uncertainty of the temperature measurements. As mentioned in Chapter 3, a forward model is needed to construct the relationship between Bi and Θ, namely $\Theta(Bi)$. Here the fin equation is used to model the conduction, hence $\Theta(Bi)$ denotes the direct solution of the fin equation. Based on Eq. (3.9), the likelihood function follows

$$p\left(\Theta_{exp}\middle|Bi\right) = \frac{1}{(2\pi\epsilon^2)^{M/2}} exp\left(-\frac{\sum_{j=1}^{M}\left(\Theta_{exp,j} - \Theta(Bi)_j\right)^2}{2\epsilon^2}\right). \tag{4.22}$$

where M is the number of temperature measurements on the disc.

Prior density function

The most commonly used prior density function for inverse problems is the Gaussian prior, for Bi:

$$Bi \sim \mathcal{N}(\overline{Bi}, C) \tag{4.23}$$

where $\overline{Bi}$ is the mean Bi distribution and C is the $N \times N$ covariance matrix based on the known information. The prior probability density function of the N-variate Bi is

$$p(Bi) = \frac{1}{(2\pi)^N |C|^{1/2}} \exp(-\frac{1}{2}(Bi - \overline{Bi})^T \mathrm{C}^{-1}(Bi - \overline{Bi})) \tag{4.24}$$

where |C| denotes the determinant of the covariance matrix. According to the definition of the Gaussian distribution, C should be a symmetric positive definite matrix.

As it is discussed in Section 4.3.2, the prior information of the smoothness of Bi can be used in Bayesian method to solve the ill-conditioned inverse problem. The prior distribution should express realistic assumptions on smoothing the field of Biot numbers, such as its smoothness or typical size of the length scale on which it varies. This smoothness of Bi can be implemented through the covariance matrix in the Gaussian prior function. Thus the mean-zero multivariate Gaussian distribution ($\overline{Bi} = 0$) with a practical covariance matrix C taken from the Matérn covariance class is chosen.

Matérn covariance

The Matérn class of covariance models is used widely in spatial statics and was introduced by *Matérn [1960] and Stein [1999]*. Then the prior distribution will be

$$P(Bi) = \frac{1}{(2\pi)^N |C|^{1/2}} \exp(-\frac{1}{2}(Bi)^T C^{-1}(Bi)) \tag{4.25}$$

where the covariance matrix C is in the form of the Matérn covariance which is shown in Eq. (4.26). The Matérn covariance class has three parameters – σ^2, l and q. σ^2 gives the variance of the diagonal terms of C which is referred to as the variance of each single Bi value, and it also controls the variability of the Bi distribution; l is the spatial length scale; q is the smoothness parameter as it gives the smoothness level, that is, the order of derivatives of Bi profiles. For any integer n, the sample profile of Bi from the prior probability density function Eq. (4.25) will be n times differentiable if and only if $q > n$ (*Stein[1999]*).

The matrix has (i, j) entries

$$C(x_i, x_j) = \frac{\sigma^2}{2^{q-1}\Gamma(q)}\left(\frac{|x_i - x_j|}{l}\right)^q K_q\left(\frac{|x_i - x_j|}{l}\right) \tag{4.26}$$

Here K_q denotes the modified Bessel function of the second kind of order q and Γ is the gamma function. x_i and x_j are the spatial location of Bi_i and Bi_j.

Determination of smoothing parameters

For the rotor disc, q is taken as 2 always, so that the Bi profile has two derivatives; l is taken to be the total nondimensional length of the disc, that is, $l = x_b - x_a$ always. σ is taken to be twice of maximum Bi number, so it is changed during the process until the convergence is reached. Increasing σ, decreasing l and decreasing q will increase the oscillation of the Bi profile. This is because Bi from the Bayesian method is in some sense the result from a balance between accuracy of the temperature measurements and the smoothness of the Biot numbers. Increase of σ and decrease of l and q reduce the relative weight of the smoothess of Bi so that more oscillating Bi will be obtained. Therefore the smoothing parameters need to be carefully selected to achieve good agreement with experiments and ideal smoothness of Bi at the same time. The validation of the Bayesian model presented in Section 4.3.3 shows that the selection of the parameters are sensible.

Estimator

A Bi profile will be calculated here, so the number of the parameters is huge. Thus, as mentioned in Chapter 3, the suitable estimator will be 'maximum a posteriori (MAP)'. The solution to the MAP $p(Bi|\Theta_{exp})$ will be the most probable value of Bi out of the measured temperature and it is denoted as Bi_{MAP}.

$$Bi_{MAP} = \arg\max_{Bi} p(Bi|\Theta_{exp}) \tag{4.27}$$

Based on Eq. (4.25) and (4.26), the posterior function of Bi has

$$P\left(Bi\middle|\Theta_{exp}\right) \propto \frac{1}{(2\pi\epsilon^2)^{\frac{M}{2}}} exp\left(-\frac{\sum_{j=1}^{M}\left(\Theta_{exp,j}-\Theta(Bi)_j\right)^2}{2\epsilon^2}\right) \times \frac{1}{(2\pi)^N|C|^{1/2}}\exp(-\frac{1}{2}(Bi)^T C^{-1}(Bi)) \tag{4.28}$$

where $\propto$ indicates that we have omitted the constant of proportionality. This function can be maximized to find the MAP point by the choice of Bi, which is shown in Eq. (4.27). For the convenience of numerical optimisation, instead of maximizing the posterior function, the negative logarithm of $P\left(Bi\middle|\Theta_{exp}\right)$ is minimized:

$$Bi_{MAP} = \arg\min_{Bi}(-\ln(P\left(Bi\middle|\Theta_{exp}\right))) \tag{4.29}$$

As the uncertainty of Θ is usually not accurately given, so in Eq. (4.28), ϵ is also treated as an unknown during the minimization. M and N will be known and chosen after the experiments and the three Matérn parameters will be given before the minimization. So minimizing $-\ln(P\left(Bi\middle|\Theta_{exp}\right))$ is equivalent to minimizing so-called posterior potential, F, which is given by

$$F = M\ln(\epsilon) + \frac{\left(\Theta_{exp}-\Theta(Bi)\right)^T\left(\Theta_{exp}-\Theta(Bi)\right)}{2\epsilon^2} + \frac{1}{2}Bi^T C^{-1} Bi \tag{4.30}$$

The first term depends on temperature data variance only; the second is the data-fitting term; and the third is a smoothing term for the profile of Biot numbers.

The MAP estimator is realized by numerical minimisation of the posterior potential F over the choice of Bi and the adjustment of ϵ. During this process, $\Theta(Bi)$ is calculated repeatedly to compare with the experimental measurements until the minimum of F is reached. The MAP points of Bi and ϵ can be denoted as

$$(Bi_{MAP}, \epsilon_{MAP}) = \arg\min_{Bi,\epsilon}(F) \tag{4.31}$$

Meanwhile, the Θ_{true} will be obtained from $\Theta(Bi_{MAP})$ which is a smooth disc temperature distribution from Bayesian method.

Confidence intervals

The MAP estimator is in some sense the most likely profile for the Biot numbers and the most probable value of the variance of the temperature data. The posterior probability density function of the Bayesian model actually gives a probability distribution on the Biot numbers and ϵ rather than just a single set of Biot numbers and a single value of ϵ. Hence further information about the reliability of the MAP estimator, i.e. the confidence intervals of Bi, could be obtained. Note: The confidence intervals that are shown below are approximate and depend on a Gaussian approximation to the posteriori distribution.

For convenience $\Phi = [Bi, \epsilon]$ and $\Phi_{MAP} = [Bi_{MAP}, \epsilon_{MAP}]$. The Taylor expansion of the posterior potential around the Map point Bi_0 and ϵ_0

$$F(\Phi) = F + \frac{\partial F}{\partial \Phi}(\Phi - \Phi_{MAP}) + \frac{1}{2}(\Phi - \Phi_{MAP})^T \frac{\partial^2 F}{\partial \Phi^2}(\Phi - \Phi_{MAP}) + higher\ order\ terms \tag{4.32}$$

where all the F terms on the right-hand side are evaluated at Φ_{MAP}. If $\Phi - \Phi_{MAP}$ is small, the higher-order terms can be dropped. Also as Φ_{MAP} is from the MAP estimator, it minimizes F and the first-order necessary condition is

$$\left.\frac{\partial F}{\partial \Phi}\right|_{\Phi = \Phi_{MAP}} = 0. \tag{4.33}$$

According to the Gaussian approximation, it is the second-order terms that define both the covariance and the confidence intervals of Φ.

$$\Phi \sim \mathcal{N}(\Phi_{MAP}, \frac{\partial^2 F}{\partial \Phi^2}^{-1}) \tag{4.34}$$

Let σ_k denotes the k^{th} square root of the leading diagonal element of the matrix $(\partial^2 F)/(\partial \Phi^2)^{-1}$. Then the corresponding 95% confidence intervals for the k^{th} of Φ_{MAP} are taken to be

$$CI(\Phi_k) = \Phi_{MAP} \pm 1.96\, \sigma_k \tag{4.35}$$

4.3.3 Validation of Bayesian method

To demonstrate the Bayesian model, the calculated Bi from the simulated experimental disc temperatures are compared to the true Bi profile. The Bi profile similar to the ones typically found on compressor discs is chosen to be the true profile. The numerical form of the general fin equation, Eq. (4.18), is used to calculate the true disc temperature. A uniformly distributed random noise is added to true temperatures and these noisy temperatures are used as the simulated experimental disc temperatures. In *Alexious [2000], Miché [2009] and Günther et al. [2014],* the Nusselt numbers are calculated by using curve-fits of the experimental temperature measurements on the disc. This approach, which creates large and unrealistic oscillations in the computed distribution of the Biot number and is referred to as the 'curve-fitting method', is also compared to the Bayesian method.

First, a true Bi profile, $Bi = 2x^5$, is used to calculate the true profile of the disc temperature using Eq. (4.18). The same disc geometry and thermal properties with Section 4.2.2 are used. $N = 301$ is used and the boundary conditions are $\Theta_a = \Theta_1 = 0.2$ at $x_1 = x_a = 0.3$ and $\Theta_b = \Theta_N = 1$ at $x_N = x_b = 1$. The true temperature is presented with black solid lines in Fig. 4.6a.

Then, 20 (that is, M = 20) of the 300 data points (only x_N is excluded, because Θ_N is always equal to 1 according to the definition of Θ) are uniformly selected, and noisy data are generated by adding independent normally-distributed random errors with mean zero and standard deviation equal to 5×10^{-3}, which is denoted as $\Theta_{exp} \sim \mathcal{N}(\Theta, 0.005)$, and. The simulated 20 data together with $\Theta_b = 1$ are shown in red circles is Fig. 4.6a.

Finally, both the Bayesian method and the conventional curve-fitting method are applied to the simulated experimental data. For the Bayesian method, the MAP estimator is computed, and Bi and ϵ are adjusted to minimise the posterior potential Eq. (4.30). The parameters for the Matérn covariance used here were $\sigma = 3.8,\ l = x_b - x_a = 0.7$ and $q = 2$, and the optimum value of ϵ was found to be 5.5×10^{-3}. This value of ϵ is similar to the original standard deviation of 5×10^{3}. Fig. 4.6b shows the calculated Bi profile and its 95% confidence intervals in a red broken line and a red shade respectively, and the calculated temperature profile is shown in a red broken line in Fig. 4.6a.

For the curve-fitting method, a 5^{th} order polynomial and a 8^{th} order polynomial function are used to fit the simulated temperature measurements. The fitted curves are shown in Fig. 4.6a in blue dash and dash-dot lines. Then the Eq. (4.18) is used to calculate Bi profiles, which are shown in Fig. 4.6b.

Although all the methods give a good approximation to the temperature distribution, only the Bayesian method provides a good estimate of Biot numbers. It is true that there is an optimum order of polynomial fitting, but in the experiments, we often lack of information of data, which make it difficult to judge the choice of the polynomial function. Another big advantage of the Bayesian method is that the confidence intervals can be computed, and it can be seen from Eq. (4.18)b that true solution of Bi lies within the 95% confidence intervals. Comparing the internal points, the confidence intervals at both ends are greatest. This is because the points near both the ends have less information to determine the Biot number.

Similar tests are done for different cases, for example, $Bi = 3x^7$(see Fig. 4.2). It is illustrated that the Bayesian could compute the Bi from temperature measurements reliably. Hence in the next section, it is applied to the actual experimental data from *Atkins and Kanjirakkad*.

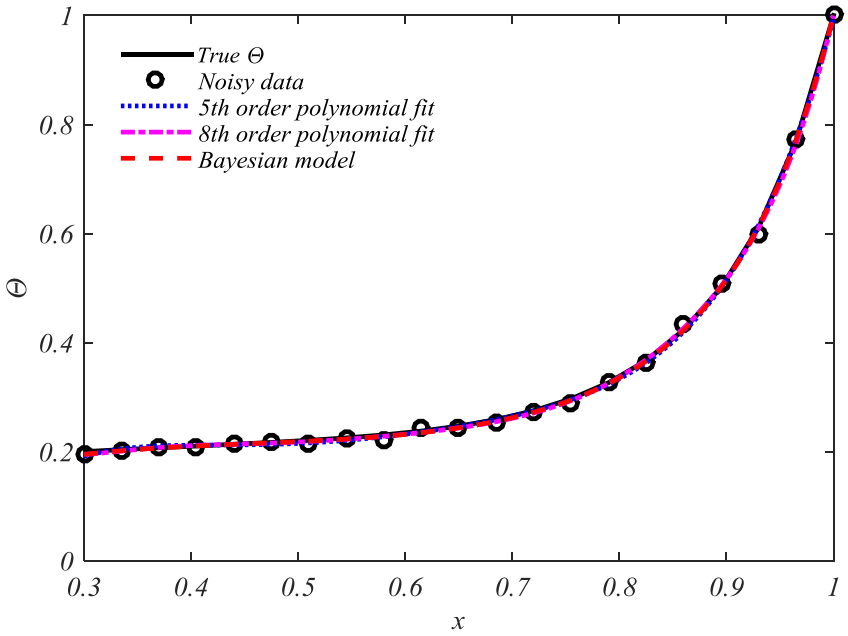

(a) Temperature distribution

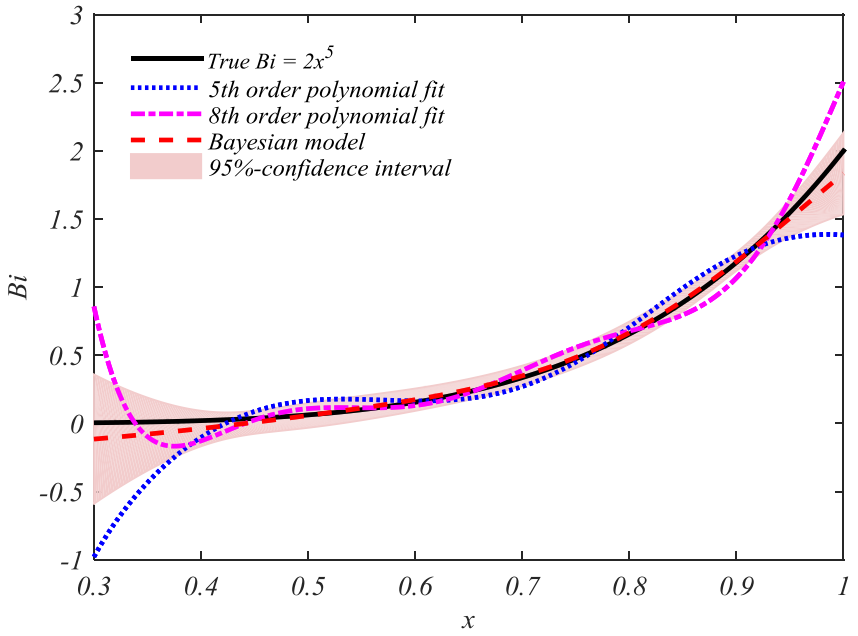

(b) Biot number distribution

Fig. 4.6 Demonstration of the Bayesian method with true $Bi = 2x^5$

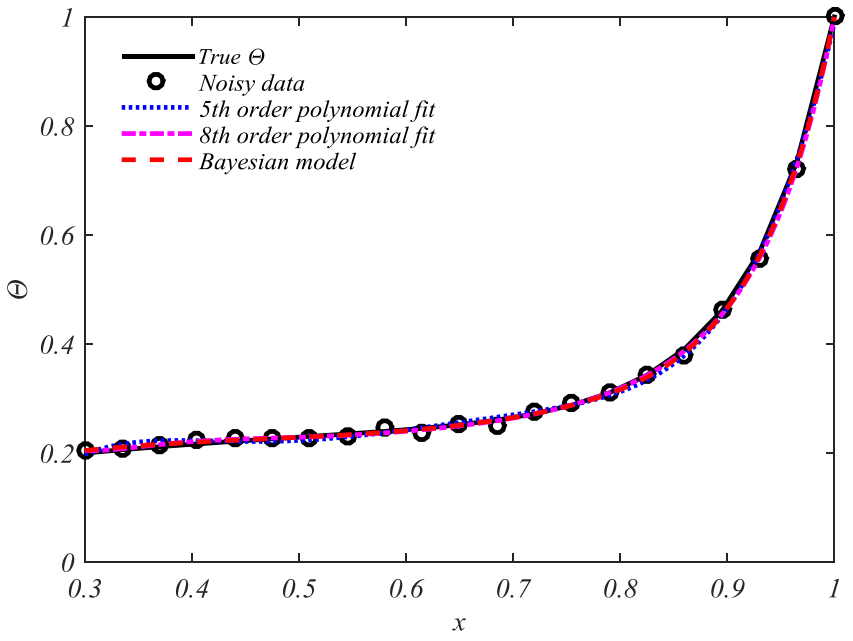

(a) Temperature distribution

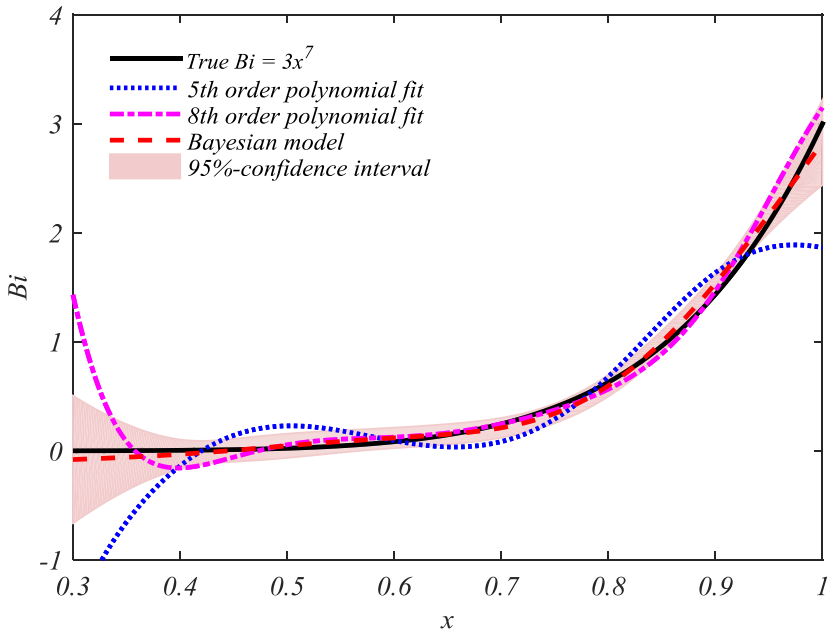

(b) Biot number distribution

Fig. 4.7 Demonstration of the Bayesian method with true $Bi = 3x^7$

4.4 Application of Bayesian method to Atkins and Kanjirakkad data

The Bayesian method of the inverse solution of the fin equation is applied to the actual temperature measurements from a multi-cavity rig used by *Atkins and Kanjirakkad*. The Nusselt numbers are obtained for all the 19 cases. The calculated Nusselt numbers (Nu), though not measured directly, are referred to as the '***experimental Nusselt numbers***'. These experimental Nusset numbers illustrate the heat convection in rotating cavities, which will be discussed in the end of this section.

4.4.1 Calculation of 'experimental Nusselt numbers'

Atkins and Kanjirakkad measured the temperatures on a rotating disc in a multi-cavity rig (Fig. 2.25) at $1.8 \times 10^4 < Re_z < 1.1 \times 10^5$, $7.7 \times 10^4 < Re_\phi < 3.5 \times 10^6$, $1.7 \times 10^8 < Gr_f < 9.1 \times 10^{11}, 0.3 < Ro < 4.9$. Fig. 2.24 is the multi-cavity rig used by *Atkins and Kanjirakkad*. The axial throughflow flows from the right to the left. The third disc is the instrumented disc where the temperature is measured on both faces. The inner and outer radii of the disc is 70.1 mm and 220 mm respectively and the disc thickness in the diaphragm section is 8 mm. The general fin equation is applied to the compressor disc shown in Fig. 4.1. The Bayesian method is used in conjunction with the general fin equation to calculate the 'experimental Nusselt numbers'. All the measurements of upstream and downstream surfaces are used (if there are more than one measurement at any radius, the averaged value is used), so the determined Nu is an average value for the two surfaces of the disc. In practice, the different flows in the upstream and downstream cavities could create different values of Nu for the two surfaces.

The temperature boundary condition is used for the fin equation. Θ_a is taken to be the average values of upstream and downstream temperature measurements at the inner radius of the disc. N is taken to be 301.

$$\Theta_1 = \Theta_a \; at \; x = x_a \,, \tag{4.36}$$

$$\Theta_N = 1 \; at \; x = 1$$

There are 25 temperature measurement points between the two limits. As the measurement points are not uniformly distributed, the closest discretization positions between $j = 1$ and $j = N$ are taken instead. Initially the Biot number profile is calculated from the Bayesian method, then Eq. (4.9) is used to work out Nusselt numbers. Recall Eq. (4.9)

$$Nu = \frac{h_f r}{k_f} \tag{4.37}$$

where $h_f = \dot{q}/(T_o - T_f)$ and k_f is the thermal conductivity of the axial through flow air. The relation between Nu_f and Bi follows

$$Bi = \frac{k_f}{k_s}\frac{b}{r}Nu \tag{4.38}$$

All 19 test cases were analysed, and details of the flow parameters are given in Table 4.1. For each of the four approximate Rossby numbers, the cases are presented in order of ascending Grashof number. Table 4.1 also shows the values of ϵ and averaged Nusselt numbers obtained from the Bayesian method. As discussed in Chapter 3, ϵ can be regarded as the standard deviation between the computed and measured value of Θ. The suggested uncertainty for Θ from *Aktins and Kanjirakkad* could be as high as 0.025. From Table 4.1, ϵ varies from 3.6×10^{-3} to 6.2×10^{-3}, which are much lower than the suggested values. This is also the reason why ϵ should be a parameter in the Bayesian process. In Table 4.1, the calculated radially-weighted average Nusselt number, Nu_{av}, which is calculated by Eq. (2.20), is shown.

	Ro ≈ 5						Ro ≈ 1							Ro ≈ 0.6		Ro ≈ 0.3			
Case No	1a	1b	1c	1d	1e	1f	2a	2b	2c	2d	2e	2f	2g	3a	3b	4a	4b	4c	4d
Ro	4.7	4.7	4.9	4.9	4.5	4.5	0.8	0.8	0.9	0.9	1.0	1.0	1.0	0.6	0.6	0.3	0.3	0.3	0.3
$Gr/10^{11}$	0.0017	0.003	0.0085	0.015	0.062	0.14	0.065	0.1	0.44	0.84	1.7	2.5	3.9	5.7	9.1	0.4	1.0	3.7	7.8
$\beta\Delta T$	0.08	0.17	0.05	0.11	0.09	0.24	0.09	0.16	0.11	0.23	0.13	0.19	0.32	0.15	0.32	0.06	0.16	0.12	0.29
$Re_\phi/10^6$	0.078	0.077	0.19	0.19	0.46	0.45	0.46	0.45	1.13	1.1	2.1	2.1	2.1	3.5	3.1	1.4	1.4	3.1	3.0
$Re_z/10^5$	0.19	0.19	0.5	0.5	1.1	1.1	0.19	0.18	0.51	0.5	1.1	1.1	1.1	1.1	1.1	0.2	0.2	0.48	0.48
$\epsilon \times 10^3$	5.4	5.1	4.4	3.9	4.7	4.3	3.6	3.3	4.3	4.5	4.5	5.0	6.2	4.8	6.1	4.2	3.9	43	5.2
Nu_{av}	31.5	32.9	55.7	61.8	97.0	113	48.2	53.4	97	126	132	170	232	128	224	45.4	81.0	73.2	143

Table 4.1 Flow parameters and standard deviation and average Nusselt numbers for experiments of Atkins and Kanjirakkad [2014].

The distributions of Θ and Nu are shown in Fig. 4.3 to Fig. 4.6 by groups of Ro. On the left is the temperature distribution: the symbols denote the experimental measurements in *Atkins and Kanjirakkad*; the curves are the temperature distributions obtained from the Bayesian method. The temperature curves are the direct solution of Eq. (4.18) with the calculated Nu profile from MAP and they are considered as 'true curves' of disc temperatures during the Bayesian process. From Fig. 4.3 to Fig. 4.6, it can be seen that they agree very well with the experimental measurements. On the right are the calculated Nusselt numbers and the 95% confidence intervals from the Bayesian method, which are shown in curves and shades respectively. For most cases, the Nu increases with radius and converges to zero near the cob region. The confidence intervals are relatively larger near both ends as there are less information compared to the middle. The discussion on the results will be given in Section 4.4.2.

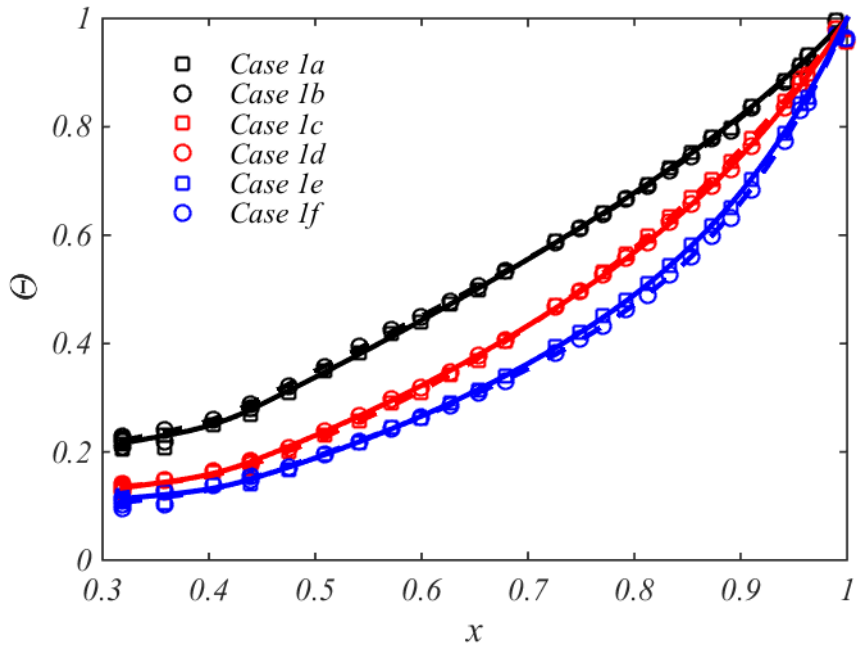

(a) Temperature distributions

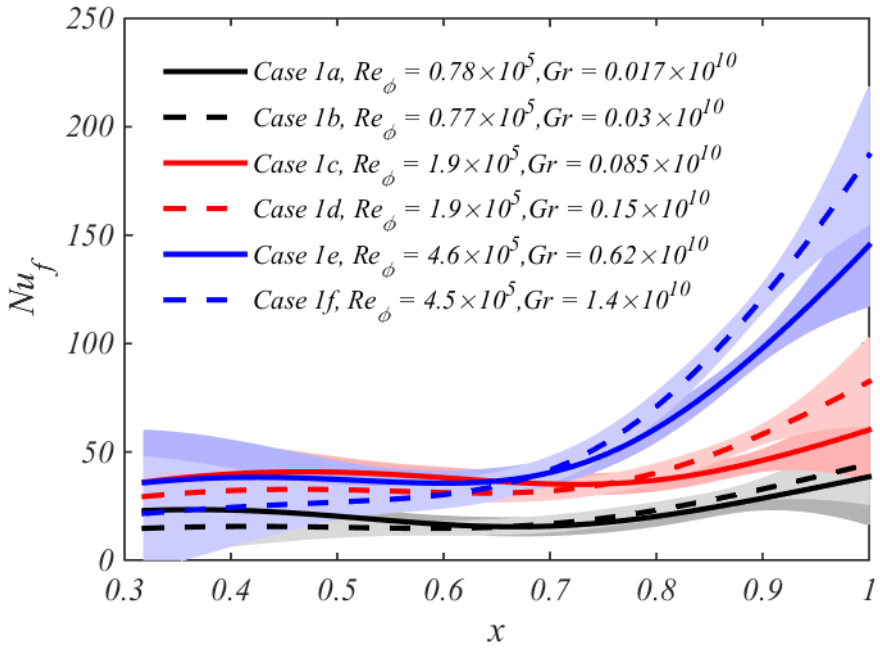

(b) Nusselt number distributions

Fig. 4.8 Disc temperatures and Nusselt numbers for *Ro* ≈ 5 (Symbols denotes measurements, curves show computations and shading shows 95% confidence intervals)

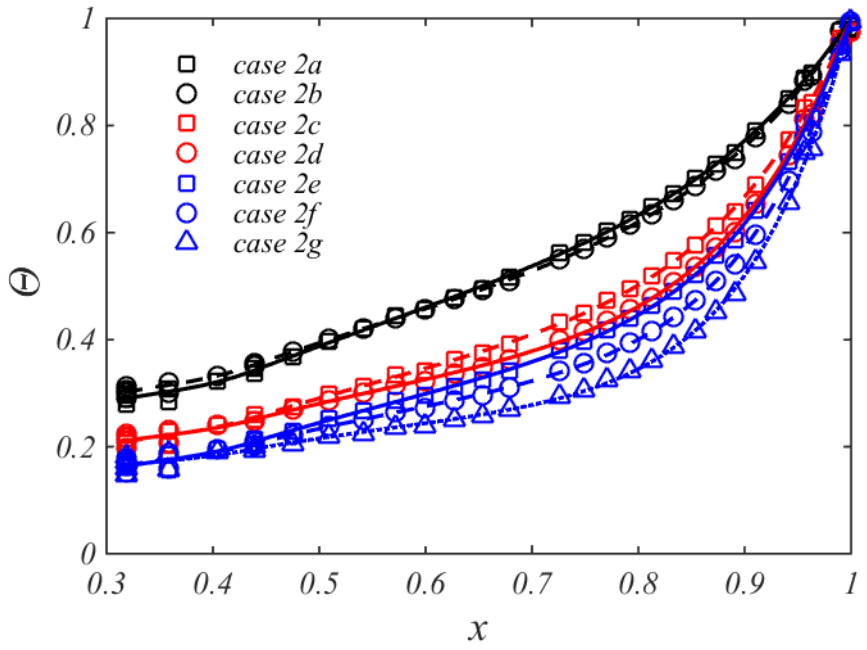

(a) Temperature distributions

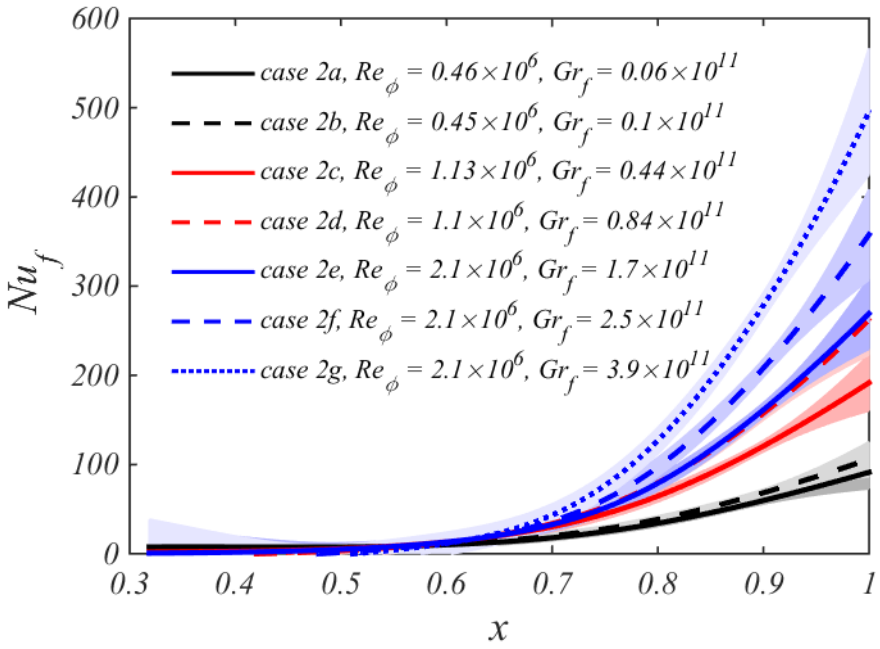

(b) Nusselt number distributions

Fig. 4.9 Disc temperatures and Nusselt numbers for *Ro* ≈ *1* (Symbols denotes measurements, curves show computations and shading shows 95% confidence intervals)

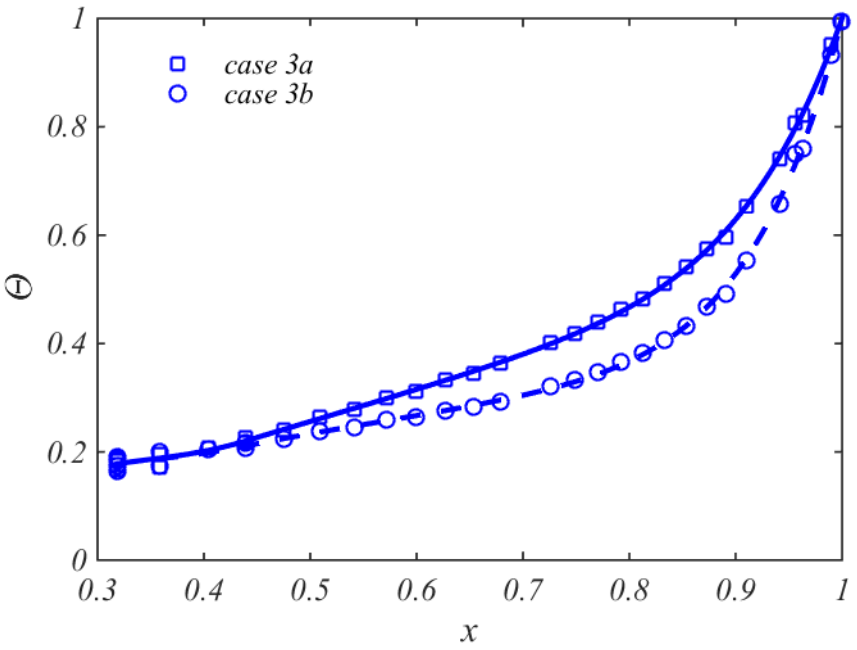

(a) Temperature distribution

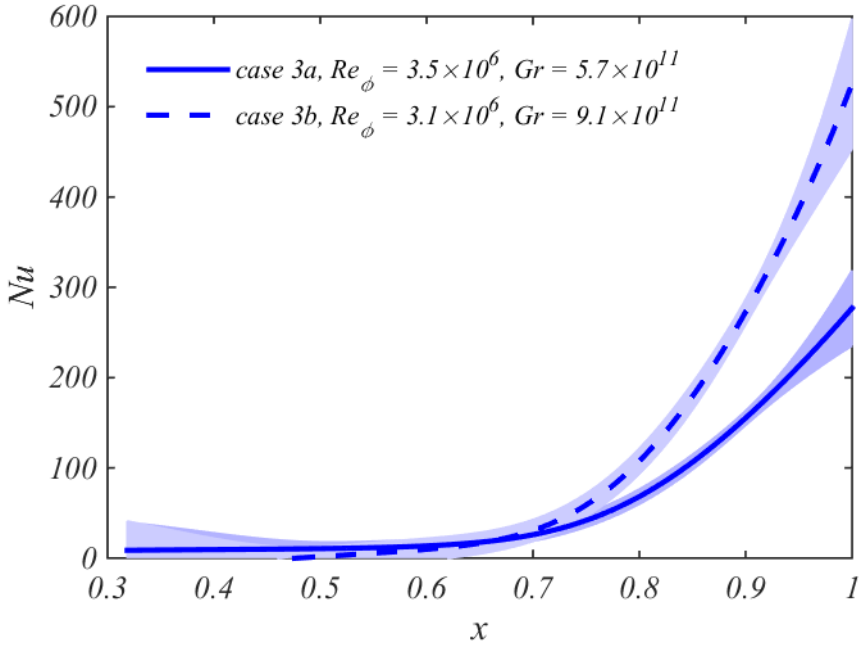

(b) Nusselt number distributions

Fig. 4.10 Disc temperatures and Nusselt numbers for *Ro* ≈ *0.6* (Symbols denotes measurements, curves show computations and shading shows 95% confidence intervals)

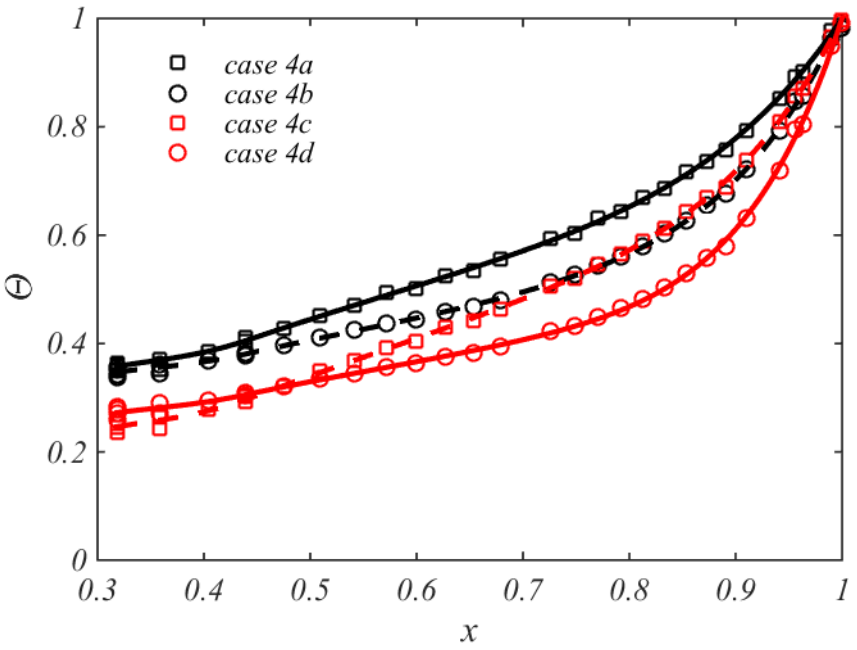

(a) Temperature distribution

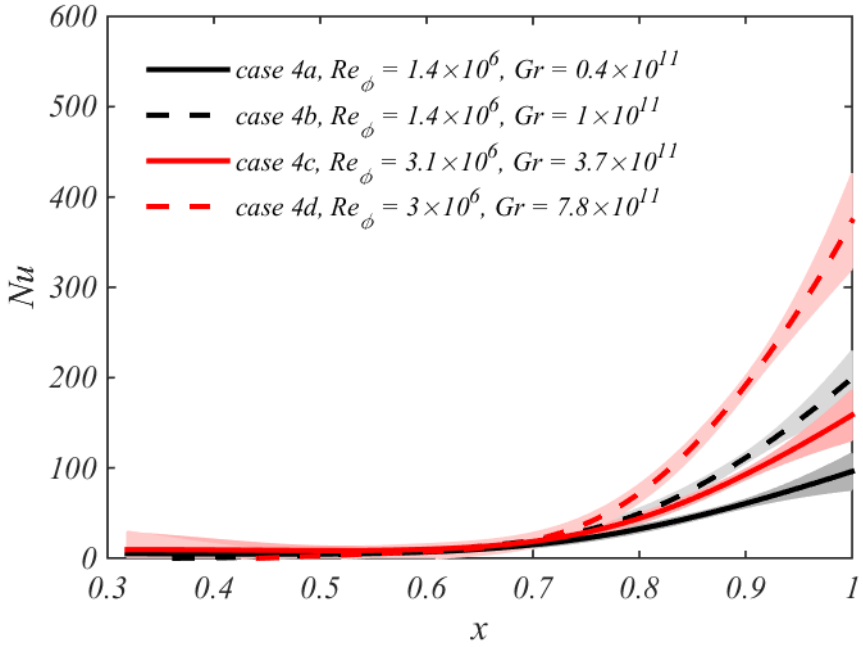

(b) Nusselt number distributions

Fig. 4.11 Disc temperatures and Nusselt numbers for *Ro* ≈ *0.3* (Symbols denotes measurements, curves show computations and shading shows 95% confidence intervals)

4.4.2 Discussion

The Nusselt numbers for the 19 cases have been obtained from the experimental temperature measurements through the Bayesian process. Although they are not measured directly, to distinguish them from the Nusselt numbers from the theory (which will be shown in Chapter 5), the Nusselt numbers from the Bayesian process are called 'experimental Nusselt numbers'. These 'experimental Nusselt numbers' can give us insights into heat convection in rotating cavities. So in this section, the feature of the Nusselt number profiles and the effects of different working conditions on Nusselt numbers are discussed.

From Fig. 4.8 to Fig. 4.11, it can be seen that for all the 19 cases, in general, the Nusselt numbers increase with radius increasing, which indicates increasing buoyancy effects. The Nusselt numbers converge to a low value at the smaller radii, especially in the high Grashof number cases. This suggests that, the effects of buoyancy are weak in the inner part of the cavity. The maximum Nusselt numbers at $r = b$ are different from case to case. How the Nusselt number changes with different working conditions will be discussed.

There are three main experimental working parameters, they are the Rossby number(Ro), the rotational Reynolds number (Re_ϕ) and the Grashof number(Gr). Recall the relationships between these parameters:

$$Ro = \frac{b^2}{2a(a-r_s)}\frac{Re_z}{Re_\phi} \tag{4.39}$$

$$Gr = \left(1-\frac{a}{b}\right)^3 Re_\phi^2 \beta\Delta T \tag{4.40}$$

As Gr is proportional to the product of the temperature difference between the shroud and the axial throughflow ($\beta\Delta T$) and Re_ϕ, and Ro is proportional to the ratio of the axial Reynolds number(Re_z) and Re_ϕ, the three independent working parameters can be Re_z, Re_ϕ and $\beta\Delta T$.

Please note that, the reference density and temperature used in these parameters are all taken as the value of axial throughflow. When the effect of one parameter on Nu is discussed, the other two parameters are approximately the same.

Effect of varying Re_z

The effects of the axial Reynolds number on Nusselt number can be seen from the cases with similar Re_ϕ and $\beta\Delta T$, for example, case 1e and 2a, or case 1f and 2b, or case 4d and 3b. At case 3b, where $Re_z \approx 1.1 \times 10^5$, Nu_{av} is higher than that at case 4d, where $Re_z \approx 4.8 \times 10^4$. This is because at high axial Reynolds numbers, the cavity temperature will be brought down, so the temperature difference between the disc and the cavity will be larger, the heat convection will be brought up, hence the Nusselt number is higher. In a word, when Re_ϕ and $\beta\Delta T$ are similar, higher Re_z will result in stronger convection in rotating cavities.

Effect of varying $\beta\Delta T$

For the cases with similar rotational Reynolds numbers and axial Reynolds numbers, for example, case 4a and 4b, or case 4c and 4d, the Nusselt numbers increase with $\beta\Delta T$ increasing. This is because the temperature difference directly drives the buoyancy effect. The higher the temperature difference, the stronger the natural convection will be, hence the Nusselt number will be increased.

Effect of varying Re_ϕ

The effect of rotational Reynolds number is more complex than the others. For most cases with similar Re_z and $\beta\Delta T$, for example, case 2b and 4b, the Nusselt number increases with Re_ϕ. This is because larger Re_ϕ will leads to larger Gr, which means there will be stronger buoyancy effects and hence heat convection in rotating cavity. However, for case 2c and 4c where $\beta\Delta T$ and Re_z are similar and the Re_ϕ values are 1.1×10^6 and 3.1×10^6 respectively, the Nusselt numbers at case 2c are much higher than those at case 4c. The most probable

explanation is that increasing Re_ϕ will not only strengthen the buoyancy effects but also result in higher cavity temperature. This is referred to as the **Re_ϕ effect** in *Tang et al. [2015]*. It will be seen that it can be explained using the theoretical model in Chapter 6.

4.5 Summary

A nondimensional form of the fin equation for circular discs has been used to model the heat transfer from air-cooled rotating discs, and Bayesian statistics have been used to determine the Biot numbers, *Bi*, or the Nusselt number, Nu, and their 95% confidence intervals from the inverse solution of the fin equation.

The power of the Bayesian method was demonstrated using simulated temperature measurements. First the direct solution of the fin equation was obtained numerically, for the case of a known radial distribution of *Bi*, and noise was added to the computed disc temperatures to simulate experimental measurements. Next, the Biot numbers were computed, using the 'experimental temperatures' as the boundary conditions for the inverse solution of the fin equation. The Bayesian method produced a smooth distribution of *Bi*, and the computed 95% confidence interval captured the true distribution. By contrast, conventional curve-fitting methods - using polynomials to approximate the experimental temperatures - resulted in large oscillations and inaccurate results.

The Bayesian method was then used to compute the Nusselt numbers, and their confidence intervals, for a compressor disc using published disc-temperature measurements of *Atkins and Kanjirakkad [2014]*. The 19 published test cases covered a wide range of Rossby, rotational Reynolds and Grashof numbers. The calculated Nusselt numbers shows that increasing Re_ϕ could lead to a decrease in Nu, which is referred to as the Re_ϕ effect.

Chapter 5 – Theoretical Model of Buoyancy-Induced Flow

The prediction of the disc temperature is a conjugate heat transfer problem which combines the heat conduction in compressor discs and the convection in rotating cavities. In Chapter 3, the conduction is modelled by the fin equation, hence what is left is the modelling of convection in rotating cavities.

The convection depends on the flow structure. When the rotating cavity is heated, buoyancy-induced flow could occur. Buoyancy-induced flow is highly 3-D and unsteady, which requires a huge amount of computing time using Computational Fluid Dynamics (CFD). However, in the engine design process, the computation needs to be done repeatedly. Therefore, a theoretical model, which is fast and of acceptable accuracy is needed for the engine design process. *Owen and Tang [2015]* published a model for buoyancy-induced flow in rotating cavities. This model will be introduced and extended in this chapter.

Section 5.1 reviews the flow structure in rotating cavities and illustrates the simplified 2-D flow structure assumed for the model. After that, in Section 5.2, the key equations for the buoyancy model are presented. Section 5.3 presents how this buoyancy model can be used to estimate the heat convection in rotating cavities. Afterwards, Section 5.4 shows how the model can be used in conjunction with the general fin equation to predict disc temperatures. For rotating cavities with axial throughflow in aeroengine compressors, another important issue is the temperature rise of the axial throughflow. Hence it is shown in Section 5.5 how the model works with the shroud heat transfer model to predict this temperature rise.

5.1 Buoyancy-induced flow in rotating cavities

As observed in *Owen and Pincombe [1979]* and *Farthing et al. [1992b]*, and as illustrated in Fig. 2.2, the axial throughflow of air creates a toroidal vortex near the centre of the rotating cavity. The radial extent of the vortex increases as the throughflow increases and the rotational speed decreases or equivalently, as Ro, the Rossby number, increases. In modern compressors, where Ro is very small, the vortex is expected to reduce to a shear layer between the throughflow and the cavity.

For isothermal rotating cavities, unless non-axisymmetric vortex breakdown occurs (*Owen and Pincombe [1979]*), the flow in the cavity is axisymmetric. When the temperature of the discs and shroud is higher than that of the axial throughflow, buoyancy-induced flow can occur and the flow radially outward of the toroidal vortex becomes non-axisymmetric. A pair or multiple pairs of cyclonic and anti-cyclonic circulation will be generated and create regions of low and high pressure. The circumferential difference of pressure produces the Coriolis forces for the radial outflow inside a "radial arm". This core structure rotates slightly slower than that of the rotating discs. The air flows radially inward within the Ekman layers on the discs. Fig. 2.4 from *Farthing et al. [1992b]* shows a schematic of the buoyancy-induced flow with a pair of circulation.

The buoyancy-induced flow is highly 3D and unsteady, so for the buoyancy model a simplified 2D flow structure needs to be assumed. The simplified 2D structure is shown in Fig. 5.1.

The cavity flow is divided into two parts – the buoyancy-induced flow in the outer region and the toroidal vortex in the inner region. It is assumed that, in the buoyancy region, the air flows radially outward in the core and inward in the Ekman layers on the discs, and that the core rotates slightly slower than the discs. These assumptions are consistent with the experimental flow structure presented in *Farthing et al. [1992b]*.

The Ekman layers are non-entraining boundary layers on the rotating discs. In the theoretical model, it is also assumed that the Ekman layers are ***laminar***. It may seem strange that, at engine conditions where the Grashof numbers are as high as 10^{12}, the Ekman layers are still laminar. However, in the literature reviewed in Chapter 2, there is evidence showing the flow is indeed laminar. *Bohn et al. [1995]* correlated their shroud Nusselt numbers for the buoyancy-induced flow in a closed rotating cavity, for Grashof number up to 10^{12}, with $Gr^{0.22}$, which is closer to the laminar exponent of 1/4 than to the turbulent one of 1/3. Moreover, *Farthing et al. [1992b]* correlated the measured disc Nusselt numbers for buoyancy-induced flow in a rotating cavity with axial throughflow with $Gr^{0.25}$. This assumption can also be interpreted from the flow structure: the rotation speed of the core is so close to that of the disc that the magnitude of the shear stress is not large enough to generate turbulent boundary layers. What is more, the demonstration of the model in Chapter 6 and Chapter 7 will also suggest that the Ekman layer flow in rotating cavities is indeed laminar.

It is also assumed that, in the outer region (the buoyancy region), the core is inviscid and adiabatic, so the temperature and pressure in the core will increase with radius. This is referred to as the compressibility effect, which can be analogous to the earth's atmosphere where the temperature and pressure decrease with vertical altitude, owing to the gravitational acceleration. While in the rotating cavity, owing to the centripetal acceleration in the core, the pressure and temperature increase adiabatically with radius.

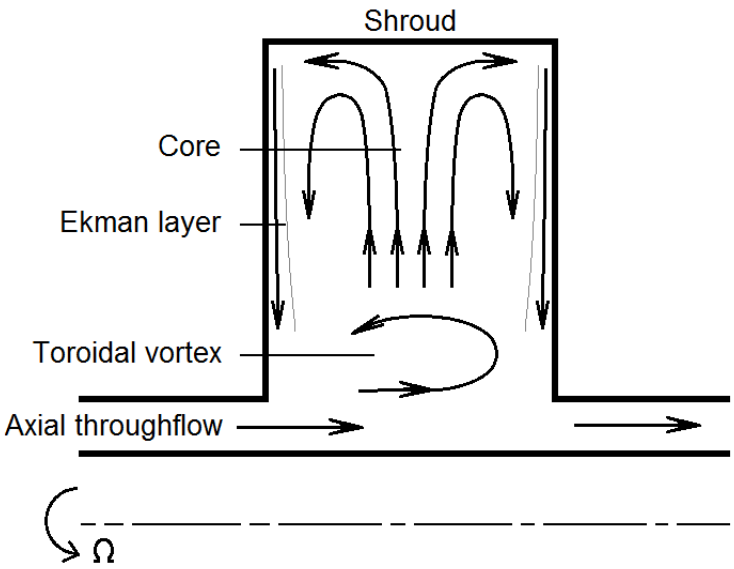

Fig. 5.1 Flow structure assumed for the buoyancy model

5.2 Buoyancy model

After the simplified flow structure is assumed, the next point is to present the equations for the buoyancy model. The derivation for the model was presented in *Owen and Tang [2015]*, here only the key equations are listed. Note: All air properties in core and in Ekman-layer are circumferentially-averaged.

5.2.1 Compressibility effect in core

As mentioned in Section 5.1, in the buoyancy region, the core pressure and temperature increase adiabatically with radius, which is referred to as the compressibility effect. According to *Owen and Tang [2015]*, the compressibility equations for T_c, p_c and ρ_c can be written in the conventional form for compressible rotating flow (Eq. (5.1) - (5.3)). Note: the values for core flow are denoted with subscript c.

$$\frac{T_c}{T_{c,a'}} = 1 + \frac{\gamma - 1}{2} Ma_c^2 (x^2 - x_{a'}^2) \tag{5.1}$$

$$\frac{p_c}{p_{c,a'}} = \left[1 + \frac{\gamma - 1}{2} Ma_c^2 \left(x^2 - x_{a'}^2\right)\right]^{\gamma/(\gamma-1)} \tag{5.2}$$

$$\frac{\rho_c}{\rho_{c,a'}} = \left[1 + \frac{\gamma - 1}{2} Ma_c^2 \left(x^2 - x_{a'}^2\right)\right]^{1/(\gamma-1)} \tag{5.3}$$

where $x_{a'} = r_{a'}/b$ and $r_{a'}$ is the inner radius of the buoyancy region(see Fig. 5.4).

The Mach number in the core, Ma_c, is defined as

$$Ma_c = \Omega_c b/c \tag{5.4}$$

where Ω_c is the rotating speed of the core, and the speed of sound is defined as

$$c = \sqrt{\gamma R T_{c,a'}} \tag{5.5}$$

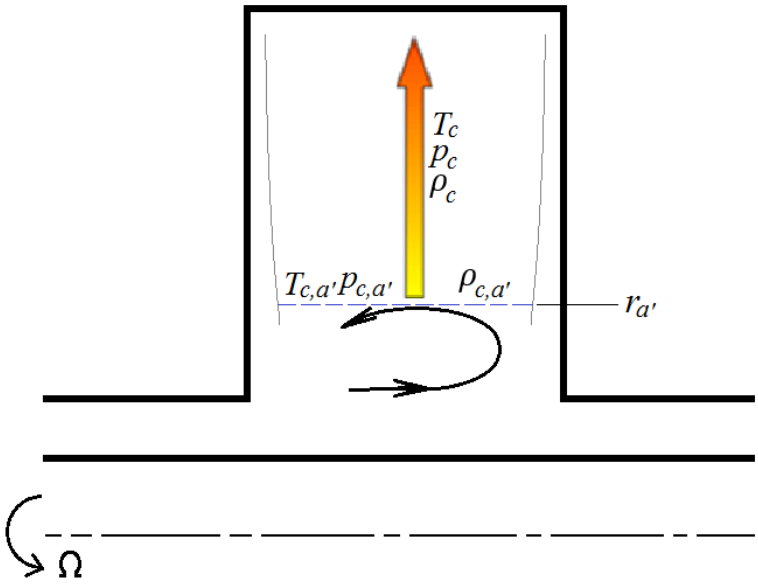

Fig. 5.2 Air properties in the core flow

5.2.2 Laminar Ekman-layer

For the flow in a rotating cavity in aeroengine compressors, the inertial terms are much smaller than the Coriolis terms, so the linear equations are solved. Given that Ekman layers are assumed to be laminar, the laminar solutions of the Ekman-layer equations are employed to

obtain an equation for computing Nusselt numbers (*Owen and Tang [2015]*). The final form of the equation is presented in Eq. (5.6). Note: Subscript 'c' denotes the value for the core, 'o' denotes the value on disc, and a' and b denote the inner and outer radii of the buoyancy region. μ, k and β are all constant and taken as the values in core flow at $r = b$.

$$Nu_c = \frac{1}{2}\frac{x_{a'}^{1/2}}{I^{1/4}} Gr_c^{1/4} \left[(\theta - Co) \left(\frac{\rho_c}{\rho_{c,b}} \right)^2 x^5 \right]^{1/3} \tag{5.6}$$

where Nu_c is the Nusselt number which uses the core temperature as the reference temperature. It is defined as

$$Nu_c = \frac{h_c r}{k_{c,b}} \tag{5.7}$$

where

$$h_c = \frac{q_o}{T_o - T_c} \tag{5.8}$$

q_o is the heat flux from the disc to air.

The Gr_c is the Grashof number for the theory and it is defined as

$$Gr_c = Re_\phi{}'^2 \beta (T_{o,b} - T_{c,b}) \tag{5.9}$$

where

$$Re'_\phi = \rho_{c,b} \Omega b^2 / \mu_{c,b} \tag{5.10}$$

θ is the nondimensional disc temperature which is defined as:

$$\theta = \frac{T_o - T_c}{T_{o,b} - T_{c,b}} \tag{5.11}$$

Co, the Coriolis parameter, is an empirical constant that must be less than unity. It is defined as

$$Co = 2\left(1 - \frac{\Omega_c}{\Omega}\right)\frac{1}{\beta\left(T_{o,b} - T_{c,b}\right)}, \tag{5.12}$$

Co is treated as an empirical constant for the Eq. (5.6). I is an integral which can be calculated from

$$I = \int_{x_{a'}}^{1} x^{11/3}\left[(\theta - Co)\left(\frac{\rho_c}{\rho_{c,b}}\right)^2\right]^{1/3} dx. \tag{5.13}$$

In Eq. (5.6), the power for Gr_c is 1/4 which is consistent with the assumption that the Ekman-layers are laminar.

The definitions of Grashof number and rotational Reynolds number for the theory are different from those for experiments. For the theory, the temperatures in the core are taken as the reference temperatures and the thermal conductivity and viscosity of the core flow at $r = b$ are used to define the parameters, while for experiments, those in the axial throughflow are used. According to the definition of Gr_c, there are two ways to increase Gr_c: increasing $Re_\phi{}'$ or increasing $\beta(T_{o,b} - T_{c,b})$.

For convenience, the model, which comprises the Ekman-layer equations and the compressibility equations, is referred to as the ***buoyancy model*** in the thesis.

5.3 Calculation of Nusselt number

To apply the buoyancy model, essential information is required. First, the shroud temperature $T_{o,b}$ and the rotational speed of the rotating cavity Ω must be provided from the working conditions, and the geometry of the cavities should be provided. Additionally, the buoyancy region needs to be assumed so that $x_{a'}$ can be specified. The only empirical constant, the Coriolis parameter Co, should be given before applying the model. Furthermore, the temperature and pressure in core at $r = a'$ (the inner radius of the buoyancy region) are required to calculate the core rotating speed (Ω_c) and the distributions of the temperature and pressure in the core

(T_c, ρ_c). With all the information provided, other variables in Eq. (5.6), Gr_c and I etc., can be calculated. Thus, the only input of the buoyancy model will be the non-dimensional disc temperature, θ, and the output will be the Nusselt number, Nu_c. Therefore, as long as the disc temperature is known, the theoretical model can be used to compute the Nusselt numbers.

Table 5.1 presents all the information needed to apply the buoyancy model to calculate the Nusselt number.

Sources of information	Variables	Symbols
From working conditions	Disc temperature at $r = b$	$T_{o,b}$
	Angular speed of disc	Ω
From disc geometry	Nondimensional radius	x
Assuming the buoyancy region	Inner nondimensional radius of buoyancy region	$x_{a'}$
Giving the empirical constant	Coriolis parameter	Co
Providing the air properties in core at $r = a'$	Temperature in core	T_c
	Density in core	ρ_c
Input	Disc temperature	T_o

Table 5.1 Parameters to apply the buoyancy model

5.4 Calculation of disc temperature

Section 5.3 shows how the buoyancy model can be used to estimate the heat convection, namely, to calculate Nusselt numbers, provided that disc temperatures are given. However, for the compressor design process, it is the disc temperature that directly determines the thermal expansion of the disc. Thus the next step is to show how the buoyancy model can be used to predict disc temperatures.

As discussed in Section 5.3, the input of the buoyancy model is the disc temperature and the output is the Nusselt number. Therefore, to predict disc temperature, the model needs to work with extra equations to close the loop between the disc temperature and the Nusselt number. The prediction of the disc temperature is a conjugate heat transfer problem so that the conduction

and the convection are coupled. The convection is modelled by the buoyancy model, and, in Chapter 4 the conduction is modelled by the fin equation. For the direct solution of the fin equation, the input is the Nusselt number and the output is the disc temperature. Therefore, the loop between the disc temperatures, the buoyancy model and the Nusselt number can be closed now, which means the buoyancy model and the fin equation can be solved iteratively to predict the disc temperature, which is referred to as the ***theoretical model*** in this thesis. This process is summarized pictorially in Fig. 5.3.

According to Eq. (5.7) and (5.8), Nu_c is defined using the core temperature as the reference temperature, however, in the definitions of the Nusselt number in Eq. (2.16) and (4.9), the temperature of the throughflow was taken as the reference temperature. To distinguish these two definitions, a subscript f is used and hence Nu_f is used to denote the Nusselt number for the fin equation or the experiments.

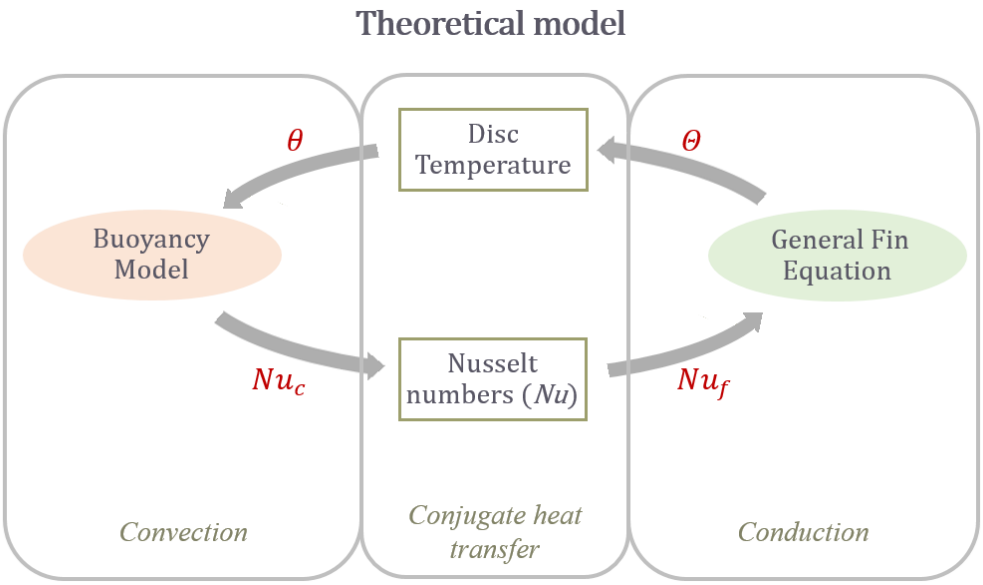

Fig. 5.3 Application of theoretical model to predict disc temperature

For the fin equation, the temperature and the thermal conductivity of the throughflow air are used to define nondimensional disc temperatures and Nusselt numbers, which are shown in Eq. (5.14) to (5.16), while, for the buoyancy model, the values in the core flow are used, (Eq. (5.7)

and Eq. (5.11)). Therefore, disc temperatures and Nusselt numbers for the theoretical model (θ, Nu_c) and for the fin equation (Θ, Nu_f) need to be connected,. The relationships are shown in Eq. (5.17) and Eq. (5.18).

$$\Theta = \frac{T_o - T_f}{T_{o,b} - T_f} \tag{5.14}$$

$$Nu_f = \frac{h_f r}{k_f} \tag{5.15}$$

$$h_f = \frac{q_o}{T_o - T_f} \tag{5.16}$$

$$\Theta = \frac{T_{o,b} - T_{c,b}}{T_o - T_c} \frac{T_o - T_f}{T_{o,b} - T_f} \theta \tag{5.17}$$

$$Nu_f = \frac{k_{c,b}}{k_f} \frac{T_o - T_c}{T_o - T_f} Nu_c \tag{5.18}$$

The buoyancy model and the fin equation are solved iteratively to predict the disc temperature. To start with, an initial profile of the disc temperature is assumed, then the buoyancy model is solved repeatedly to update the Nusselt numbers and the general fin equation is solved to update the disc temperature. All the information listed in Table 5.1 is required to solve the buoyancy model (the input will be the disc temperature updated by the fin equation). To solve the fin equation, T_f and k_f should be given and the boundary conditions at both ends of the disc are necessary. The boundary condition at the outer radius is always fixed with $\Theta_b = 1$. However, for the inner radius, as mentioned in Section 4.1.2, two different boundary conditions, the temperature boundary condition and the convective boundary condition, are considered, the choice of which depends on the experimental setup. Ideally, the convective boundary condition should be used, because it doesn't require the temperature at the inner radius to predict the profile of the disc temperature. However, currently there is no available correlation

for the heat convection on the inner surface of the disc. Hence it is only possible to use this boundary condition if a practical correlation can be obtained from the experimental data. To get this correlation, the measurements of the air temperature of the axial throughflow below the disc are required. Therefore, only an experiment that provides this information can use the convective boundary condition, otherwise the temperature boundary condition will be used.

After all the information is provided, the buoyancy model and the general fin equation can be solved to predict the disc temperature. This process will be validated by comparing the theoretical predictions to the experimental measurements. In Chapter 4, the measured disc temperatures for the 19 cases in *Atkins and Kanjirakkad [2014]* were used to demonstrate the Bayesian method. In Chapter 6, they will used again to validate the theoretical model. What is more, *Puttock-Brown [2016]* presented disc temperature measurements for 10 different cases. Thus the process will be also applied to his experiments. The application to experiments in *Atkins and Kanjirakkad* and in *Puttock-Brown* will be shown in detail in Chapter 6 and Chapter 7 respectively.

Prior to the application to these experiments, the radial extent of the buoyancy region in the rotating cavity needs to be assumed. For most of the cases in both sets of experiments, the values of Ro are less than 1, so it is assumed in this thesis that, the toroidal vortex is close to being a shear layer. Therefore, the buoyancy region starts at $r = a$, which means, $a' = a$ and $x'_a = x_a$. Consequently, both the buoyancy model and the fin equation will be solved from $r = a$ to $r = b$.

The fin equation is solved directly to update the disc temperature. The geometry of the disc will be given. The reference temperature T_f and the air thermal conductivity will be provided by the working conditions. The boundary condition at $r = b$ is always fixed at $\Theta_b = 1$, while for $r = a$, two different kinds of boundary conditions mentioned before will be used for different sets of data. For the prediction for experiments of *Atkins and Kanjirakkad*, since the

axial throughflow temperature below the disc is not measured, the temperature boundary condition will be used. For the prediction for experiments in *Puttock-Brown*, the axial throughflow temperature is measured, so a correlation for the heat convection on the inner surface of the cob can be obtained, so the convective boundary condition will be used.

For solving the buoyancy model, as mentioned before, all the information listed in Table 5.1 is needed. The input will be the temperature calculated from the fin equation. The buoyancy region has been assumed from $r = a$ to $r = b$. The working conditions and the disc geometry will be given, and the empirical parameter, Co will be chosen. Then the only unknowns will be the air temperature and density in core. From the 'experimental Nusselt numbers' calculated in Chapter 4, most of the profiles converged to low values near the cob region (where the disc thickens), so it is assumed for both sets of experiments that $Nu_f = 0$ at $r = a$. When the disc is heated, the temperature of the disc is always higher than that in core, which means $T_{o,a} > T_{c,a}$. Thus, from Eq. (5.18), $Nu_{c,a} = 0$. From Eq. (5.6), it can be seen that $Nu_{c,a} = 0$ if and only if $\theta_a = Co$, where $\theta_a = (T_{o,a} - T_{c,a})/(T_{o,b} - T_{c,b})$. Additionally it is assumed that the core pressure at $r = a$ is close to that in axial throughflow, that is, $p_{c,a} = p_f$ where p_f can be given by working conditions. With these assumptions, the compressibility equations, the ideal gas equation and Eq. (5.12) (the definition of the Co parameter) can be solved, then the air temperature and density in the core can be computed.

Given all the information, the disc temperature for both sets of experiments can be predicted. The detailed predictions for experiments by *Atkins and Kanjirakkad* and *Puttock-Brown* will be shown in Chapter 6 and Chapter 7 respectively.

5.5 Calculation of temperature rise of axial throughflow

When the shroud temperature is higher than the throughflow, the heat will transfer from the disc and the shroud to the cavity flow, which will then lead to a temperature increase for the axial throughflow. In a HP compressor, the throughflow will be used to cool the turbine stages,

so this temperature rise is critical for the cooling design of aeroengines. Hence this temperature rise should be estimated during engine design stage.

5.5.1 Energy balance

Fig. 5.4 is a typical multi-cavity system. To study the energy balance, a confined region should be selected. As mentioned in Chapter 4, the fin equation calculates the average Nusselt number of both radial disc surfaces, hence a region, which includes the whole disc, is selected. This region is confined by the two mid faces of two neighbouring cavities, the shroud and the inner shaft. It is assumed that the heat transferred from the inner shaft is negligible, that the work terms are relatively small compared with the heat transfer, and that the heat transfer on the upstream and downstream faces of the region are approximately the same. Therefore, as shown in Fig. 5.4, the temperature increase of the axial throughflow from $T_{f,i-1/2}$ to $T_{f,i+1/2}$ will be mainly caused by the heat from the shroud ($\dot{Q}_{sh,i}$), the two radial disc surfaces ($\dot{Q}_{u,i}$ and $\dot{Q}_{d,i}$) and the cob surface ($\dot{Q}_{a,i}$). Note: 'i' is used here to denote the disc referred to and '1/2' is used to denote half a cavity away from the disc. So the energy balance to calculate the increase in the ***bulk-mean total temperature*** of the axial throughflow is given by

$$c_p \dot{m}_f \left(T_{f,i+\frac{1}{2}} - T_{f,i-\frac{1}{2}} \right) = \dot{Q}_{sh,i} + (\dot{Q}_{u,i} + \dot{Q}_{d,i}) + \dot{Q}_{a,i} \tag{5.19}$$

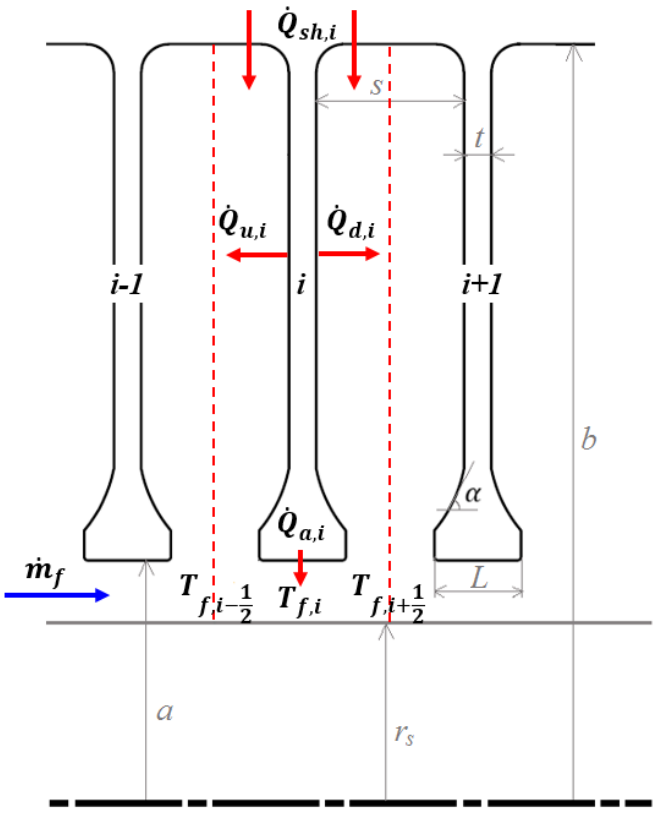

Fig. 5.4 Energy balance for rotating cavities with axial throughflow

5.5.2 Prediction of disc heat transfer

When the convective boundary condition at $r = a$ is used for the fin equation, the buoyancy model and the fin equation could be solved iteratively without the input of the disc temperature at $x = x_a$. However, as far as the author is aware, there is no published correlation for the heat convection on the inner surfaces of cobs. Therefore, a correlation based on the available experimental results needs to be assumed here. *Puttock-Brown* measured the disc temperature as well as the air temperature of the throughflow in the multi-cavity rig of University of Sussex. The air temperatures are used to obtain a practical correlation in Chapter 7. In this section, only the form of correlation is presented.

Different forms of correlations, including the free convection and forced convection schemes, were tried, but in the end only the correlation between the cob Nusselt number and the Reynolds

number based on the relative velocity between the axial throughflow and the cob was used. Two constants, B_1 and B_2, are used for heat transfer correlations.

$$Nu_a = B_1 Re_T^{B_2} \tag{5.20}$$

where

$$Nu_a = \frac{h_a L}{k_f} = \frac{\dot{q}_a L}{k_f\left(T_{o,a} - T_f\right)} \tag{5.21}$$

and

$$Re_T \equiv \frac{\rho_f \sqrt{W^2 + (\Omega a)^2} L}{\mu_f}. \tag{5.22}$$

where L here is the axial width of the cob and T_f is the temperature below the referred disc.

This correlation can be converted into the convective boundary for solving general fin equation (see Section 4.1.2).

The convective boundary condition for the fin equation is reproduced as

$$\frac{h_a b}{k_s}\Theta_a = \frac{d\Theta}{dx}|_{x=x_a}. \tag{5.23}$$

To apply this boundary condition to the numerical form of the fin equation (Section 4.2.2), a ficticious point $\Theta = \Theta_0$ at $j = 0$ is used. For the convective boundary condition,

$$\Theta_0 = \Theta_2 - \frac{2(x_2 - x_1)h_a b}{k_s}\Theta_a. \tag{5.24}$$

For the numerical scheme of the fin equation at $j = 1$ and $x = x_1$,

$$\frac{\Theta_2 - 2\Theta_1 + \Theta_0}{\Delta x^2} + \left(\frac{1}{x_1} - \frac{2}{\tau_1}\frac{cos\,\alpha_1}{sin\,\alpha_1} + \frac{1}{k_s(\Theta_1)}\frac{k_s(\Theta_2) - k_s(\Theta_0)}{2\Delta x}\right)\frac{\Theta_2 - \Theta_0}{2\Delta x} - \frac{Bi_1}{\tau_1\,sin\,\alpha_1}\Theta_1 = 0. \tag{5.25}$$

Θ_0 in Eq. (5.25) could be replaced by Eq. (5.24) and h_a could be provided by Eq. (5.21). Then then fin equation could be solved using the convective boundary condition.

The heat transfer for the inner surface of the cob can be calculated based on the correlation. The absolute heat transfer for the cob is calculated by:

$$\dot{Q}_{a,i} = 2\pi a L \dot{q}_a. \tag{5.26}$$

where $\dot{q}_a$ can be calculated basing on Eq. (5.20) and (5.21). The final form will be

$$\dot{Q}_{a,i} = 2\pi a k Nu_a\left(T_{o,a} - T_f\right). \tag{5.27}$$

The buoyancy model and the general fin equation with the convective boundary condition in Eq. (5.20) can be solved iteratively to estimate disc temperatures and Nusselt numbers. Then the heat flux from the disc radial surfaces could be predicted. Since the Nusselt number is actually equivalent to the averaged value of the two disc faces, the theoretical prediction of the heat fluxes on both faces are the same, which can be written as

$$\dot{Q}_{u,i} = \dot{Q}_{d,i} = \dot{Q}_o \tag{5.28}$$

The heat flux can be calculated through the integration on the radial disc surface:

$$\dot{Q}_o = 2\pi \int_a^b kNu_f(T_o - T_f)/sin\,\alpha\, dr \tag{5.29}$$

The heat transfer on the inner surface of the cob and that on the radial faces form the heat transfer from the disc. So the disc heat transfer will be

$$\dot{Q}_{a,i} + 2\dot{Q}_o \tag{5.30}$$

5.5.3 Prediction of heat transfer for the shroud

After the heat transfer for the disc is predicted, the remaining part will be the heat transfer for the shroud. Analogously to the free convection on a horizontal plate in the gravitational field, the free convection correlation for horizontal plates is used. The theoretical model for buoyancy-induced flow assumes that the Ekman-layer flow is laminar, hence, to be consistent, the laminar free convection correlation for horizontal plates is applied to the heat transfer for the shroud. There is evidence that the convection on the shroud is indeed laminar. As mentioned in Section 5.1, *Bohn et al. [1995]* correlated the shroud Nusselt numbers in a closed rotating cavity with $Gr^{0.22}$, which is close to the laminar exponent 1/4. *Long and Childs[2007b]* correlated the shroud Nusselt number with Grashof number and it was found that the experimental results are very close to the curve using the laminar correlation(see Fig. 2.16).

The correlation of free convection on horizontal plates (*Incropera and DeWitt [1996]*) is then applied to the shroud:

$$Nu_{sh} = 0.54(Gr_{sh}Pr)^{0.25} \tag{5.31}$$

where

$$Gr_{sh} = \frac{\rho_{c,b}^2 \Omega_c^2 b}{\mu_{c,b}} \frac{T_{sh} - T_{c,b}}{T_{c,b}} \left(\frac{s}{2}\right)^3 \tag{5.32}$$

and

$$Nu_{sh} = \frac{\dot{q}_{sh}\left(\frac{s}{2}\right)}{k_{c,b}(T_{sh} - T_{c,b})}. \tag{5.33}$$

The local air temperature, the core temperature at $r = b$, is taken as the reference temperature, and the ratio of the shroud area to the perimeter, s/2, is taken as the characteristic length. k, μ

and ρ are all taken to be the values at $r = b$. The disc temperatures at $r = b$ are taken as the shroud temperatures, that is, $T_{sh} = T_{o,b}$.

Then the calculation of the shroud heat transfer can be written as

$$\dot{Q}_{sh,i} = 2\pi bs\dot{q}_{sh} \tag{5.34}$$

or

$$\dot{Q}_{sh,i} = 4\pi bkNu_{sh}\left(T_{o,b} - T_{c,b}\right) \tag{5.35}$$

5.5.4 Prediction of temperature increase and comparison to experiment

After all the heat fluxes have been predicted, Eq. (5.19) could be used to calculate the temperature increase -- $T_{f,i+\frac{1}{2}} - T_{f,i-\frac{1}{2}}$. For convenience, Eq. (5.19) is rearranged below as

$$T_{f,i+\frac{1}{2}} - T_{f,i-\frac{1}{2}} = \frac{\dot{Q}_{sh,i} + 2\dot{Q}_o + \dot{Q}_{a,i}}{c_p\dot{m}_f} \tag{5.36}$$

The non-dimensional temperature increase is defined:

$$\Delta\Theta_f = \frac{T_{f,i+\frac{1}{2}} - T_{f,i-\frac{1}{2}}}{T_{o,b} - T_{f,i}} \tag{5.37}$$

5.6 Summary

The buoyancy-induced flow and heat transfer inside the compressor rotors is modelled by the buoyancy model proposed by *Owen and Tang [2015]*, assuming laminar Ekman-layer flow on the discs and compressible flow in the fluid core between the Ekman layers.

Using the buoyancy model in conjunction with the fin equation, which is referred to as the theoretical model, the disc temperature and the Nusselt number can be predicted. For the buoyancy model, it is necessary to assume a value for the Coriolis parameter, Co. For the fin equation, the measured temperature of the shroud is used as the outer boundary condition, and,

depended on if the axial throughflow is measured, the temperature inner boundary condition and the convective inner boundary condition can be chosen. This process will be applied to the prediction of the temperature and Nusselt number for experiments of *Atkins and Kanjirakkad [2014]* and of *Puttock-Brown [2016]*, which will be shown in Chapter 6 and Chapter 7 respectively.

The theoretical model is extended to correlate the Nusselt numbers for the shroud and cob as well as estimating the temperature rise of the axial throughflow of the cooling air. The correlation for laminar free convection on horizontal plates is used to model the heat transfer from the shroud. This process will be applied to experiments of *Puttock-Brown* in Chapter 7.

Chapter 6 – Prediction of Atkins and Kanjirakkad Data

Chapter 5 illustrated that the theoretical model, which comprises the buoyancy model and the fin equation, can be used to predict the disc temperature. *Atkins and Kanjirakkad [2014]* measured the disc temperatures for 19 cases in a multi-cavity rig, and in this chapter the theoretical predictions are compared to their experimental data.

To begin with, the experimental working parameters are related to the parameters used in the model. Then the assumptions for the theoretical prediction are presented. After that, the theoretical model is used to calculate the disc temperature. Since no correlation for the convection on inner surfaces of cobs is available and no practical correlation can be obtained from the experimental data, the temperature boundary condition is used for solving the fin equation. Later the theoretical model is demonstrated by comparing the theoretical disc temperatures and Nusselt numbers to the experimental ones. Finally, the effects of the working parameters on Nusselt numbers are discussed.

6.1 Relationship between theoretical and experimental parameters

In experiments, the working conditions are given by a group of nondimensional parameters (see Section 2.1). These parameters are all defined using the air properties of the axial throughflow, which are denoted using the subscript 'f'. In order to distinguish between the Grashof number for the experiments and for the buoyancy model, a subscript 'f' is also added to 'Gr'. However, the theoretical model uses the air properties of the core flow to define the nondimensional parameters, which are the Grashof number and the Reynolds number, Gr_c and $Re_\phi{}'$. The definitions have been given by Eq. (5.9) and (5.10) in Chapter 5. The definitions for

those used in experiments are reproduced in Eq. (6.1) and (6.2) Eq. (6.3) and (6.4) are given to clarify the differences and to show the relationships.

$$Re_\phi = \frac{\rho_f \Omega b^2}{\mu_f} \tag{6.1}$$

$$Gr_f = \left(1 - \frac{a}{b}\right)^3 Re_\phi^2 \frac{T_{o,b} - T_f}{T_f} \tag{6.2}$$

$$Re_\phi = \frac{\rho_f}{\rho_{c,b}} \frac{\mu_{c,b}}{\mu_f} Re_\phi{}' \tag{6.3}$$

$$Gr_f = \left(1 - \frac{a}{b}\right)^3 \left(\frac{\rho_f}{\rho_{c,b}}\right)^2 \left(\frac{\mu_{c,b}}{\mu_f}\right)^2 \frac{T_{c,b}}{T_f} \frac{T_{o,b} - T_f}{T_{o,b} - T_{c,b}} Gr_c \tag{6.4}$$

The prediction of the disc temperature is a conjugate heat transfer problem, so both the theoretical predictions of disc temperatures and Nusselt numbers will be compared to the experimental ones. Fig. 6.1 shows the logic of the comparison. The temperature measurements from *Atkins and Kanjirakkad* are used for the ***experimental temperatures***. The Nusselt numbers calculated using the Bayesian method in Chapter 4 are used here as the '***experimental Nusselt numbers***'. As discussed in Section 5.4, the ***theoretical disc temperatures*** and the ***theoretical Nusselt numbers*** are calculated using the theoretical model.

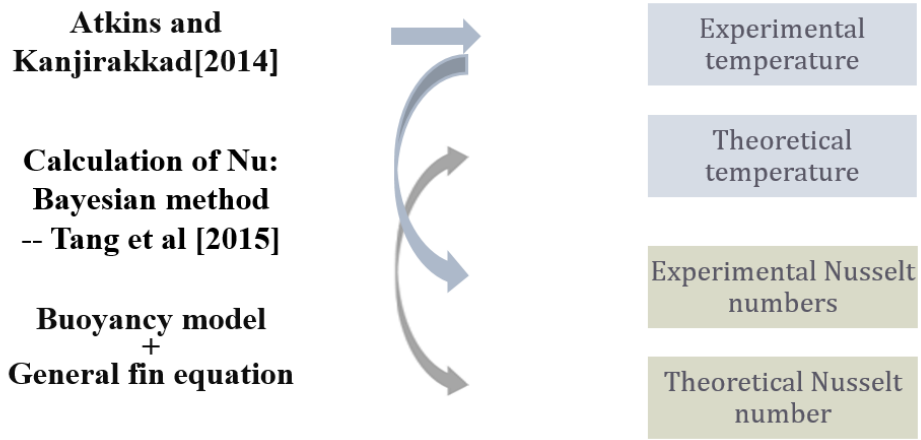

Fig. 6.1 Comparison between theory and experiment

The air properties of the axial throughflow are also used to define the experimental nondimensional disc temperature and Nusselt number, which are denoted as Θ and Nu_f. The same definitions are used for the fin equation (see Section 4.1). Therefore the experimental profiles of Θ and Nu_f can be compared to those predicted by the theoretical model.

It is also useful to compare the average disc temperature and average Nusselt number. The average nondimensional disc temperature, which is denoted as Θ_{av}, is calculated by Eq. (6.5).

$$\Theta_{av} = \frac{2\pi \int_a^b \frac{T_o - T_f}{T_{o,b} - T_f} r dr}{2\pi \int_a^b r dr} = \frac{\int_{x_a}^1 \Theta x dx}{\int_{x_a}^1 x dx} \tag{6.5}$$

The equation to calculate Nu_{av} has been given by Eq. (2.20). It is reproduced in Eq. (6.6).

$$Nu_{av} = \frac{\int_{x_a}^1 Nu_f \Theta dx}{\int_{x_a}^1 \Theta x dx} \tag{6.6}$$

6.2 Assumptions

Atkins and Kanjirakkad presented the non-dimensional parameters, $Gr, Re_\phi, \beta\Delta T, Re_z$ and Ro, and the nondimensional temperature measurements, Θ, for 19 cases. To work out the absolute disc temperature, the temperature of the axial throughflow, T_f, is needed. To work out the working condition from the experimental working parameter, the density of the axial throughflow air, ρ_f, is required. If the pressure of the throughflow, p_f, could be provided, ρ_f, can be calculated using the perfect gas law. But T_f and p_f are given for only four cases. Therefore, the pressure p_f for $Re_z/10^5 \approx 0.2$, 0.5 and 1.1 were assumed to be 1.20, 1.33 and 1.47 bar respectively. Although T_f is expected to be different for different working conditions, it was assumed – in the absence of more information – to be constant at 294K.

Section 5.4 discussed the information required for the prediction of the disc temperature. Further details are explained below.

To begin with, ***unlike*** the paper by *Tang and Owen [2016]* where only the diaphragm section ($x_{a'} = 0.439$) was used for the theoretical model to predict disc temperatures for experiments by *Atkins and Kanjirakkad*, in this thesis, it is assumed that the toroidal vortex region is so small that the buoyancy model is applied to the whole cavity. Therefore, the inner radius of the buoyancy region is equal to that of the disc, i.e., $x_a' = x_a$ = 0.319. Consequently, both the general fin equation and the buoyancy model will be solved from x_a to x_b.

As mentioned in Section 5.4, since *Atkins and Kanjirakkad* didn't measure the throughflow temperature below the cob and there is no available correlation for the heat transfer on the cob, the temperature boundary condition at $x = x_a$ is used to solve the fin equation. Thus, at $x = x_a$, $\Theta = \Theta_a$, where Θ_a is the average of the disc temperature measurements on the upstream and downstream faces at $x = x_a$. At $x = x_b = 1$, Θ is always fixed at $\Theta_b = 1$.

As discussed in Section 5.4, the input of the buoyancy model will be the temperature calculated from the general fin equation. The only empirical constant for the buoyancy model, the Coriolis parameter, Co, should be given. As there is not enough information about the swirl ratio in rotating cavities, a single value of $Co = 0.029$ is used for all the 19 cases. This value is chosen to minimize the difference between the average theoretical and experimental nondimensional disc temperature. The experimental parameters and the disc geometry were provided. The only unknown information is the core temperature and density. As discussed in Section 4.4, it is assumed the Nusselt number at x_a is zero, so $\theta_a = Co$, where $\theta_a = (T_{o,a} - T_{c,a})/(T_{o,b} - T_{c,b})$. It is also assumed that the core pressure is close to that of the axial throughflow air, which is $p_{c,a} = p_f$. Then the compressibility equations can be coupled with the definition of Co and the ideal gas law to calculate the radial variation of the temperature and density of the core.

All the information required for predicting the disc temperature for experiments by *Atkins and Kanjirakkad* is listed in Table 6.1.

Sources of information	Variables	Symbols
From working conditions	Disc temperature at $r = b$	$T_{o,b}$
	Angular speed of disc	Ω
	Throughflow temperature	T_f
	Throughflow pressure	p_f
From disc geometry	Nondimensional radius	x
	Nondimensional thickness	τ
	Angel of gradient of disc surface	α
Assuming the buoyancy region	Inner nondimensional radius of buoyancy region ($x_{a'} = x_a$)	$x_{a'}$
Giving the empirical constant	Coriolis parameter	Co
Temperature boundary condition $x = x_a$	Disc temperature at $x = x_a$	$T_{o,a}$
Assuming $\theta_a = Co, p_{c,a} = p_f$	Core temperature	T_c
	Core density	ρ_c

Table 6.1 Information required to apply the theoretical model

Once all the assumptions are made, the theoretical model can be applied to predict the disc temperature. Firstly, an initial profile of the disc temperature is given, then the buoyancy model and the fin equation are solved iteratively. The iteration stops when the disc temperature converges, that is, when the maximum of Θ changing is less than 10^{-4}. The converged profiles of the disc temperature and the Nusselt number will be the theoretical predictions. Detailed results will be shown in Section 6.3.

6.3 Comparisons between theory and experiment

MATLAB code is used to solve the theoretical model. The calculation only takes seconds to obtain the converged profiles of disc temperatures and Nusselt numbers with a laptop. The comparisons between the predictions and the experiments are shown below.

6.3.1 Average disc temperatures and Nusselt numbers

Before showing the distributions, it is useful to compare the average values. Table 4.1 has already shown the main working parameters and the average experimental Nusselt numbers for 19 experimental cases of *Atkins and Kanjirakkad*, which are reproduced in Table 6.2. The table also presents the average experimental and theoretical disc temperatures and the average theoretical Nusselt numbers. The experimental and theoretical values are distinguished using the subscripts, exp and th, respectively.

	Ro ≈ 5						Ro ≈ 1							Ro ≈ 0.6		Ro ≈ 0.3			
Case No	1a	1b	1c	1d	1e	1f	2a	2b	2c	2d	2e	2f	2g	3a	3b	4a	4b	4c	4d
Ro	4.7	4.7	4.9	4.9	4.5	4.5	0.8	0.8	0.9	0.9	1.0	1.0	1.0	0.6	0.6	0.3	0.3	0.3	0.3
$Gr/10^{11}$	0.0017	0.003	0.0085	0.015	0.062	0.14	0.065	0.1	0.44	0.84	1.7	2.5	3.9	5.7	9.1	0.4	1.0	3.7	7.8
$\beta\Delta T$	0.08	0.17	0.05	0.11	0.09	0.24	0.09	0.16	0.11	0.23	0.13	0.19	0.32	0.15	0.32	0.06	0.16	0.12	0.29
$Re_\phi/10^6$	0.078	0.077	0.19	0.19	0.46	0.45	0.46	0.45	1.13	1.1	2.1	2.1	2.1	3.5	3.1	1.4	1.4	3.1	3.0
$Re_z/10^5$	0.19	0.19	0.5	0.5	1.1	1.1	0.19	0.18	0.51	0.5	1.1	1.1	1.1	1.1	1.1	0.2	0.2	0.48	0.48
$\Theta_{av,exp}$	0.601	0.603	0.509	0.508	0.452	0.443	0.595	0.590	0.492	0.468	0.446	0.417	0.381	0.460	0.398	0.625	0.565	0.546	0.485
$\Theta_{av,th}$	0.607	0.598	0.533	0.514	0.460	0.433	0.574	0.571	0.482	0.464	0.433	0.416	0.398	0.465	0.409	0.617	0.568	0.545	0.493
$Nu_{av,exp}$	31.5	32.9	55.7	61.8	97.0	113	48.2	53.4	97	126	132	170	232	128	224	45.4	81.0	73.2	143
$Nu_{av,th}$	30.7	35.8	50.3	60.9	91.4	117	55.8	60.9	101	121	137	159	190	119	190	47.1	74.8	71.4	127

Table 6.2 Working parameters and experimental and theoretical average disc temperatures and Nusselt numbers for 19 experimental cases of Atkins and Kanjirakkad [2014]

Mainly good agreement between theory and experiment has been obtained, even for the cases with high Grashof numbers (up to $Gr_f = 9.1 \times 10^{11}$, typical of those found in aeroengine compressors). Fig. 6.2 and Fig. 6.3 show the comparison between $\Theta_{av,exp}$ and $\Theta_{av,th}$ and that between $Nu_{av,th}$ and $Nu_{av,exp}$ respectively. The red symbols are the theoretical predictions and the broken lines are the experimental values. As Co was chosen to minimise the average temperature differences, it could not minimise the difference between the average Nusselt numbers predicted from the theoretical model and the 'experimental values' obtained using the

Bayesian method. Consequently, the agreement between the theoretical and experimental average temperatures is very good, but the average Nusselt numbers are slightly underpredicted. It can be seen that the differences between the theoretical and experimental Θ_{av} are all less than 0.025. Although the Nusselt numbers are underestimated, the differences between the theoretical and experimental values are still within 20%. The theoretical Nusselt numbers were relatively insensitive to the value of *Co*: doubling *Co* from 0.029 to 0.058 increases the value of $Nu_{av,th}$ by less than 7%.

Section 4.4.2 discussed the effects of Re_z, Re_ϕ and $\beta\Delta T$ on Nu_f from the distributions of the 'experimental Nusselt numbers'. For the average values, it can be seen that these effects are well predicted by the theory, including the paradox when discussing the effects of Re_ϕ. The explanations of these effects using the theoretical model will be presented in Section 6.4.

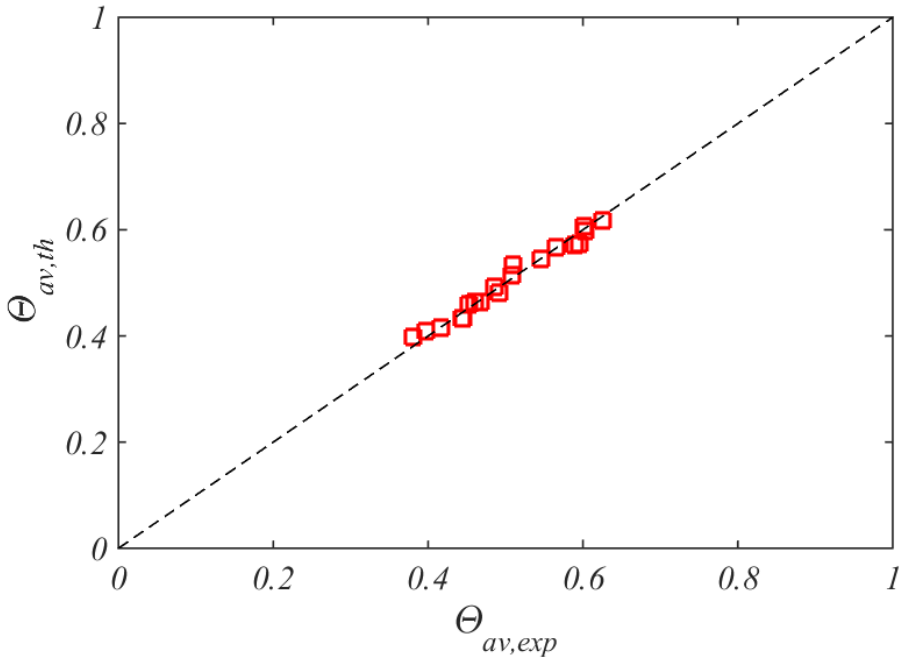

Red squares – theoretical prediction of average disc temperatures, broken line – $\Theta_{av,exp} = \Theta_{av,th}$

Fig. 6.2 Comparison of theoretical and experimental average disc temperatures

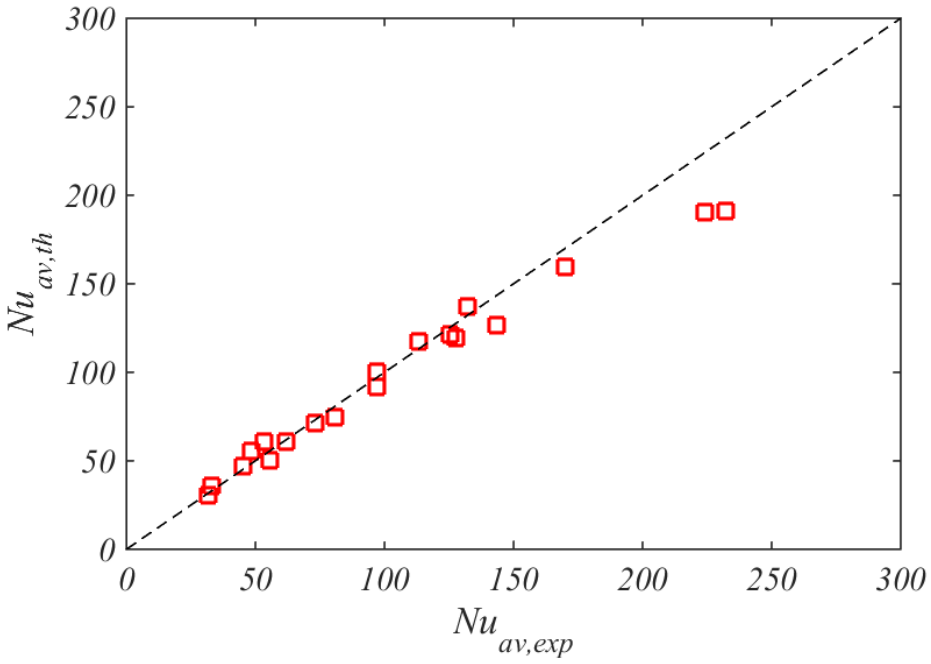

Red squares – theoretical prediction of average Nusselt numbers, broken line – $\Theta_{av,exp} = \Theta_{av,th}$

Fig. 6.3 Comparison of theoretical and experimental average Nusselt numbers

6.3.2 Radial distributions of disc temperatures and local Nusselt numbers

Fig. 6.4 – Fig. 6.7 show the comparisons between the experimental and theoretical radial distributions of Θ and Nu_f for all the cases shown in Table 6.2. The sub figures on the left and the right are the comparisons of Θ and Nu_f respectively. The symbols are the temperature measurements made by *Atkins and Kanjirakkad*. The solid curves in the left and right figures show the theoretical distributions of Θ and Nu_f, which are obtained using the theoretical model with an overall constant $Co = 0.029$. The broken curves are the profiles of Θ and Nu_f obtained from the Bayesian method in Chapter 4. The shaded regions are the 95% confidence intervals of Nu_f calculated from the Bayesian method. The results are presented below and are then discussed in more detail in Section 6.4. In general, an overestimate of the Nusselt numbers will result in an underestimate of the temperatures and vice versa.

Fig. 6.4 shows the results for the six test cases at $Ro \approx 5$. In Fig. 6.4a, for Cases 1a and 1b, the experimental Nusselt numbers increase linearly with x, which is consistent with laminar

flow over a free disc. At these relatively low Grashof numbers it is probable that the effects of buoyancy are very small, so laminar forced-convection dominates for the rotating discs in the cavity. For these cases, the theoretical Nusselt numbers overestimate the experimental values near the shroud where $x = 1$. The overestimate can also be seen in Fig. 6.4b, for cases 1c and 1d, but the upturn at larger radii suggests that the buoyancy effects are starting to become significant. In Fig. 6.4c, for cases 1e and 1f, the experimental Nusselt numbers at the larger radii show clear evidence of buoyancy-induced flow. Even though there are discrepancies between the profiles of the theoretical and experimental Nu_f in Fig. 6.4, the theoretical profiles of Θ show reasonable agreement with the measurements.

Fig. 6.5 shows the results for $Ro \approx 1$. All seven cases show strong evidence of buoyancy-induced flow and there is mainly good agreement between the theoretical and experimental distributions of Θ and Nu_f. From case 2a to case 2g, Nu_f increases as Gr_f increases, which indicates that the buoyancy effects are getting stronger. The values of Gr_f are highest for the two cases for $Ro \approx 0.6$ in Fig. 6.6 (up to $Gr_f = 9.1 \times 10^{11}$, typical of those found in aeroengine compressors.), where again there is good agreement between the theoretical and experimental distributions. As the buoyancy model is based on laminar Ekman-layer flow, this suggests that the buoyancy-induced flow for these cases is indeed laminar.

Fig. 6.7, for $Ro \approx 0.3$, again good agreement is achieved. From case 4b to 4c, although Gr_f increases from 1.0×10^{11} to 3.7×10^{11}, both theoretical and experimental Nu_f decreases. This will be explained using the 'Re_ϕ effect' mentioned in Section 4.4.2 and it will be illustrated using the theoretical model in Section 6.4.

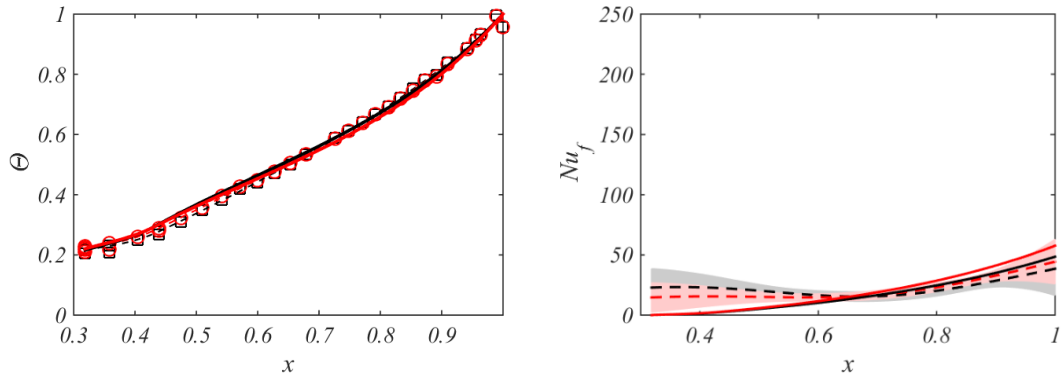

Fig. 6.4 (a) Case 1a (black) and case 1b (red)

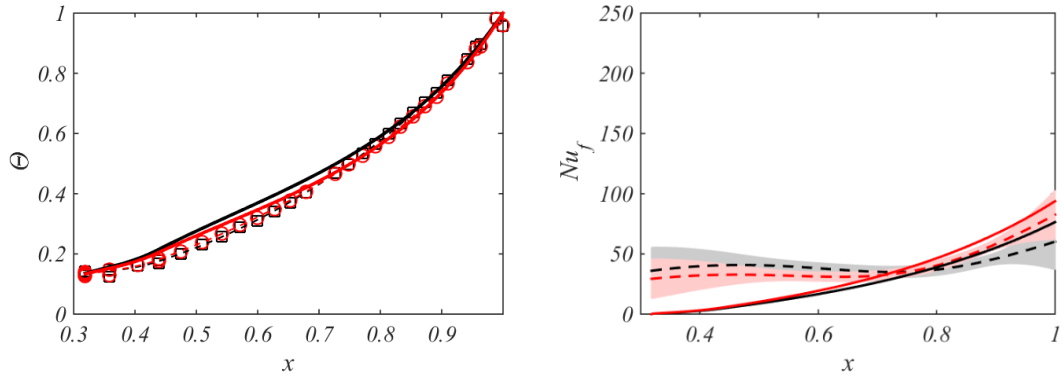

Fig. 6.4 (b) Case 1c (black) and case 1d (red)

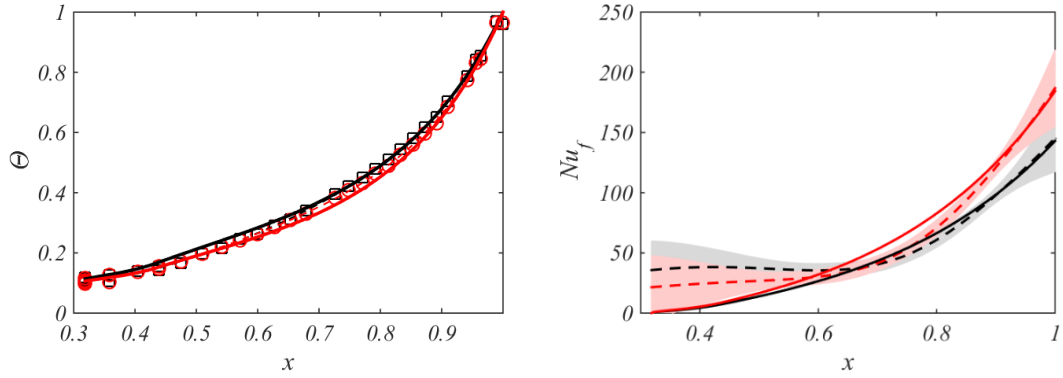

Fig. 6.4 (c) Case 1e (black) and case 1f (red)

Symbols denote measured temperatures; broken lines represent results obtained from the Bayesian method; solid lines denote the theoretical prediction; shading shows 95% confidence intervals on experimental Nusselt numbers

Fig. 6.4 Distributions of disc temperatures and Nusselt numbers for $Ro \approx 5$

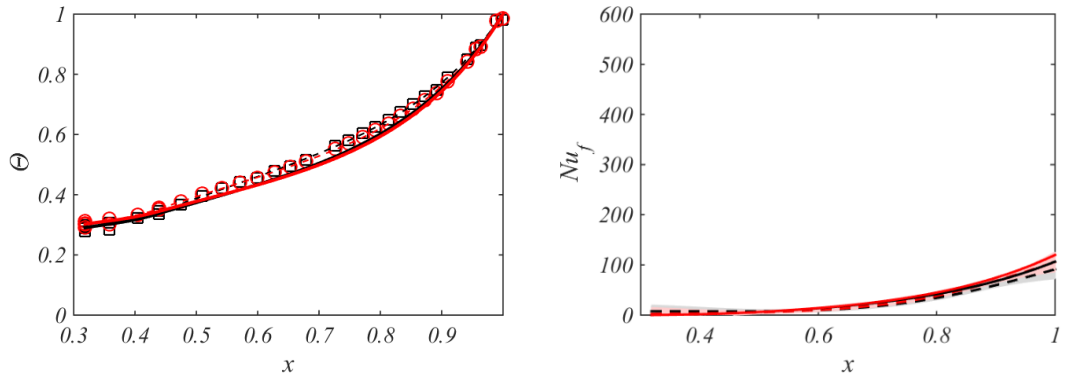

Fig. 6.5 (a) Case 2a (black) and case 2b (red)

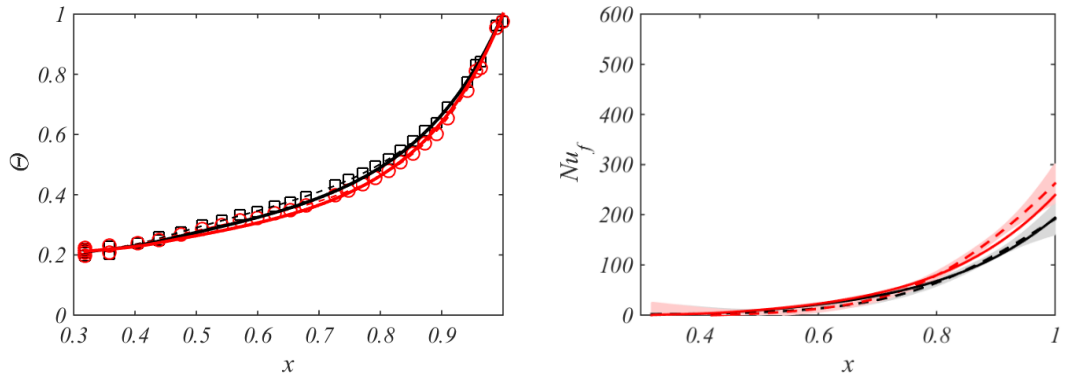

Fig. 6.5 (b) Case 2c (black) and case 2d (red)

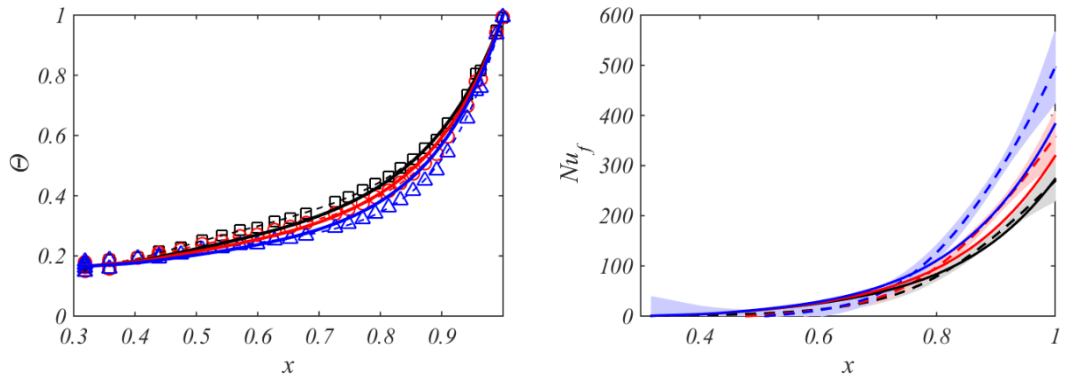

Fig. 6.5 (c) Case 2e (black), case 2f (red) and case 2g (blue)

Symbols denote measured temperatures; broken lines represent results obtained from the Bayesian method; solid lines denote the theoretical prediction; shading shows 95% confidence intervals on experimental Nusselt numbers.

Fig. 6.5 Distributions of disc temperatures and Nusselt numbers for $Ro \approx 1$

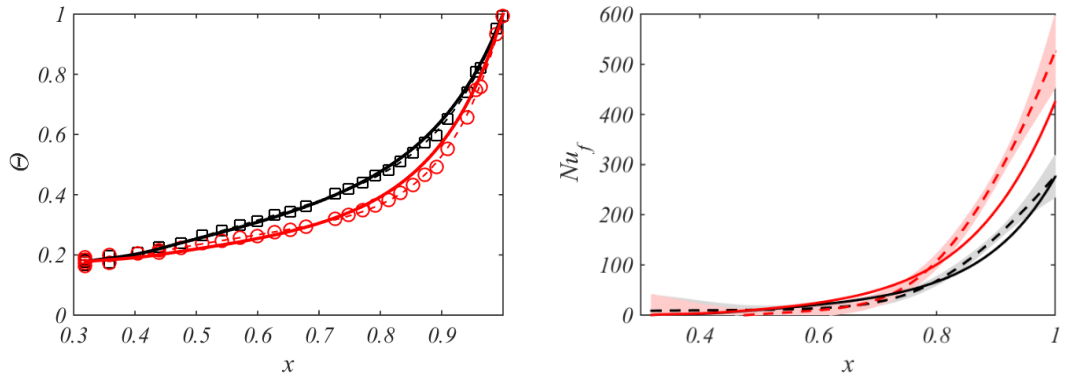

Symbols denote measured temperatures; broken lines represent results obtained from the Bayesian method; solid lines denote the theoretical prediction; shading shows 95% confidence intervals on experimental Nusselt numbers.

Fig. 6.6 Distributions of disc temperatures and Nusselt numbers for *Ro* ≈ *0.6* (case 3a – black, case 3b – red)

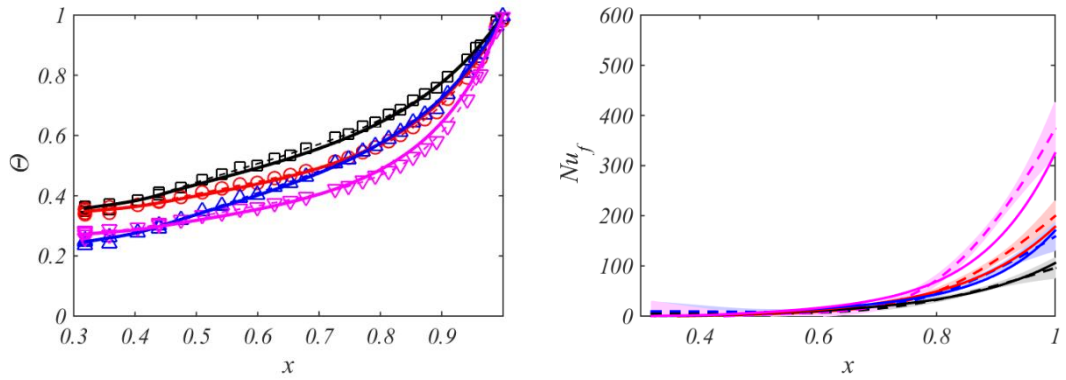

Symbols denote measured temperatures; broken lines represent results obtained from the Bayesian method; solid lines denote the theoretical prediction; shading shows 95% confidence intervals on experimental Nusselt numbers.

Fig. 6.7 Distributions of disc temperatures and Nusselt numbers for *Ro* ≈ *0.3* (case 4a – black, case 4b – red, case 4c – blue, case 4d – magenta)

6.4 Discussion

The effects of Re_z, Re_ϕ and $\beta\Delta T$ on Nu_f were discussed in Section 4.4.2 where the experimental Nusselt numbers are obtained from the temperature measurements. In this section, these effects will be explained in detail using the theory.

To explain these effects, it is necessary to show how Nu_f is predicted. Eq. (5.18) shows the relationship between Nu_c and Nu_f, which is reproduced as

$$Nu_f = \frac{k_{c,b}}{k_f}\frac{T_o - T_c}{T_o - T_f}Nu_c \tag{6.7}$$

where the core temperature, T_c, is always higher than T_f, so Nu_f is smaller than Nu_c.

Nu_c is the Nusselt number calculated from the buoyancy model. Recall the calculation of Nu_c:

$$Nu_c = \frac{1}{2}\frac{x_a^{1/2}}{I^{1/4}}Gr_c^{1/4}\left[(\theta - Co)\left(\frac{\rho_c}{\rho_{c,b}}\right)^2 x^5\right]^{1/3} \tag{6.8}$$

Nu_c is governed by Gr_c, which is defined as

$$Gr_c = {Re_\phi}'^2\beta(T_{o,b} - T_{c,b}) \tag{6.9}$$

Re'_ϕ is the rotational Reynolds number used in the buoyancy model and it can be related to Re_ϕ by

$${Re_\phi}' = \frac{\rho_{c,b}}{\rho_f}\frac{\mu_f}{\mu_{c,b}}Re_\phi \tag{6.10}$$

Therefore, from the definitions above, it can be seen that Nu_f is proportional to both $(T_o - T_c)/(T_o - T_f)$ and Nu_c, and Nu_c increases as Re_ϕ increases, or as $T_{o,b}$ increases, or as $T_{c,b}$ decreases. Therefore, Nu_f increases with increasing T_o (including $T_{o,b}$), or increasing Re_ϕ , or decreasing T_c (including $T_{c,b}$).

Effect of Re_z

Increasing Re_z will enhance the heat transfer between the axial throughflow and the rotating cavities, which will in turn decrease the core temperature, T_c. So Nu_f will be increased. This explains why case 3b has higher Nu_f than case 4d (see Tab. 6.3).

Cases 4d and 3b have similar Re_ϕ and $\beta\Delta T$ but different Re_z (Tab. 6.3). The average Nusselt number for case 3b, where $Re_z = 1.1 \times 10^5$, is much higher than that for case 4d, where $Re_z = 4.8 \times 10^4$, which shows that increasing Re_z will increase Nu_f.

	Re_z	$\beta\Delta T$	Re_ϕ	$Nu_{c,b}$	$Nu_{av,th}$
Case 4d	4.8×10^4	0.29	3.0×10^6	482	127
Case 3b	1.1×10^5	0.32	3.1×10^6	540	190

Table 6.3 Comparison between case 4d and case 3b – Effects of Re_z on Nu_f

Effect of $\beta\Delta T$

Increasing $\beta\Delta T$ is achieved by increasing disc temperatures, T_o and $T_{o,b}$, so both $(T_o - T_c)/(T_o - T_f)$ and Nu_c will be increased. Therefore, according to Eq. (6.8), Nu_f will be increased. This is shown by the comparison between case 4c and case 4d in Table 6.4.

	Re_z	$\beta\Delta T$	Re_ϕ	$Nu_{c,b}$	$Nu_{av,th}$
Case 4c	4.8×10^4	0.12	3.1×10^6	373	71.4
Case 4d	4.8×10^5	0.29	3.0×10^6	482	127

Table 6.4 Comparison between case 4c and case 4d – Effects of $\beta\Delta T$ on Nu_f

Effect of Re_ϕ

As discussed in Section 4.4, the effect of Re_ϕ on Nu_f is complex. The Nu_f can either increase or decrease as Re_ϕ increases. The theory predicted the trends well. This complex behaviour is explained below.

In the theoretical model, the core temperature increases with increasing radius owing to the compressibility effect. This increase can be calculated in Eq. (6.11).

$$\frac{T_c}{T_{c,a}} = 1 + \frac{\gamma - 1}{2} Ma_c^2 (x^2 - x_a^2) \tag{6.11}$$

where $Ma_c = \Omega b/c$.

It follows from Eq. (6.11) that T_c increases as Ma_c increases. Therefore increasing Re_ϕ will also increase T_c. As shown in Eq. (6.7) , for a given value of Nu_c, Nu_f decreases as T_c increases. Therefore, an increase in Nu_f, which is caused by an increase in Re_ϕ, will be less than that in Nu_c, and, under some conditions, Nu_f could decrease as Re_ϕ decreases. This explains the paradox of the Re_ϕ effect discussed in section 4.4.2 and examples are shown below

When the value of Re_ϕ is relatively low, the core temperature increase from $r = a$ to $r = b$ will be relatively small. For example, for case 2b where $Re_\phi = 4.5 \times 10^5$, $(T_{c,b} - T_{c,a})$ is only about 0.3K , and for case 4b where $Re_\phi = 1.4 \times 10^6$, $(T_{c,b} - T_{c,a})$ is still only 3K. Consequently, the decrease of $R_{\Delta T}$ from case 2b to case 4b is relatively small and the increase of Nu_c dominates the change of Nu_f, so Nu_f will be increased. This is shown in Table 6.5.

However, for case 4c where $Re_\phi = 3.1 \times 10^6$, $(T_{c,b} - T_{c,a})$ is about 12K while for case 2c where $Re_\phi = 1.1 \times 10^6$, $(T_{c,b} - T_{c,a})$ is only about 1K, so the decrease of $(T_o - T_c)/(T_o - T_f)$ dominates the change of Nu_f. Therefore, even though case 4c has higher Nu_c than case 2c, Nu_f will be lower, which is also shown in Table 6.5.

	Re_z	$\beta\Delta T$	Re_ϕ	Gr_f	$Nu_{c,b}$	$Nu_{av,th}$
Case 2b	1.8×10^4	0.16	4.5×10^5	1.0×10^{10}	162	60.9
Case 4b	2.0×10^4	0.16	1.4×10^6	1.0×10^{11}	279	74.8
Case 2c	4.8×10^4	0.11	1.1×10^6	4.4×10^{10}	248	101
Case 4c	4.8×10^4	0.12	3.1×10^6	3.7×10^{11}	373	71.4

Table 6.5 Comparison between case 2c and case 4c – Effects of Re_ϕ on Nu_f

As Gr_f is proportional to the product of Re_ϕ and $\beta\Delta T$, the effects of Gr_f is actually the combining effects of Re_ϕ and $\beta\Delta T$. If an increase in the Gr_f is caused by an increase in $\beta\Delta T$ then both Nu_c and Nu_f will increase. If however an increase in the Grashof number is caused by an increase in Re_ϕ then the increase in Nu_f will be less than that in Nu_c and, under some conditions, Nu_f could decrease. This reduction of Nu_f with increasing Gr_f can be seen from the comparison between case 2c and case 4c and that between case 4b and case 4c.

6.5 Summary

This chapter used the theoretical model (which comprises the buoyancy model and the general fin equation) to predict the disc temperature for experiments by *Atkins and Kanjirakkad* in a multi-cavity rig. The ranges of the experimental parameters were: $1.7 \times 10^8 < Gr_f < 9.1 \times 10^{11}; 7.7 \times 10^4 < Re_\phi < 3.5 \times 10^6; 1.8 \times 10^4 < Re_z < 1.1 \times 10^5; 0.3 \times Ro < 5; 0.05 < \beta\Delta T_f < 0.32$. As far as the author is aware, it is the first time a theoretical buoyancy model (rather than CFD or a statistical model) has been used to predict the temperatures in a compressor-disc rig or in any other rotating-disc rig.

A constant Co (0.029) was used for the buoyancy model, and it was assumed that Nusselt number at x_a was equal to zero. The temperature boundary condition at x_a was used for the fin equation. The MATLAB code was used to solve the theoretical model. It only took seconds for the model to predict the Nusselt number and disc temperature using a laptop whereas it would take days or even weeks to make these predictions using unsteady 3D CFD.

The theoretical distributions of Θ and Nu_f were compared to the experimental ones. The 'experimental Nusselt' numbers were obtained in Chapter 4 using the Bayesian statistics in conjunction with the fin equation. The results showed that buoyancy-induced flow did not occur until $Gr_f > 8.5 \times 10^8$. Mainly good agreement between theory and experiment was achieved,

especially at high Gr_f cases, which suggests that the Ekman-layer flow is indeed laminar even at the high Grashof numbers found inside compressor rotors, where $Gr_f = O(10^{12})$.

The paradox of the Re_ϕ effects, where an increase in Re_ϕ can cause a reduction in Nu_f, has been explained.

Chapter 7 – Prediction of Puttock-Brown Data

In Chapter 6, the theoretical model was used to predict the disc temperatures for the experiments of *Atkins and Kanjirakkad [2014]*. In this chapter, the disc temperature and the temperature increase of the axial throughflow are predicted for the experiments of *Puttock-Brown [2016]*.

The theoretical disc temperature is calculated using a similar approach to that applied in Chapter 6. First, the assumptions for the calculation including the convective boundary condition are presented. Then both the theoretical disc temperatures and Nusselt numbers are compared to the experimental values. Besides that, the theoretical and experimental core temperatures are compared.

The temperature increase of the axial throughflow is predicted using the approach presented in Section 5.5. The predicted distributions of the disc temperatures and the Nusselt numbers are used to calculate the heat transfer from the disc surfaces. The correlation obtained for the convective boundary condition is used to calculate the heat transfer from the inner surface of the cob. Next, the correlation for laminar free convection on horizontal plates is used to calculate the heat transfer from the shroud. Then the temperature increase of the throughflow can be computed using the energy balance equation. Finally, the predicted temperature increases are compared to the experimental measurements.

7.1 Prediction of disc temperature

7.1.1 Assumptions

Puttock-Brown measured the disc temperatures in a similar rig to the one *Atkins and Kanjirakkad* used. Besides the disc temperatures, he also measured the air temperature of the

axial throughflow, using thermocouples located at several different axial positions in the throughflow, and the air temperature in the cavity using thermocouples fixed on the upstream disc at $x = 0.580$. The temperature measurements of the axial throughflow can be used to obtain a correlation for convection on the inner surface of the cob. Thus, instead of using the temperature boundary condition to solve the fin equation, as was done in Chapter 6, a convective boundary condition is used here. To validate the theoretical model using the convective boundary condition, the calculated disc temperatures and Nusselt numbers are compared to experimental values. The relationships between theoretical and experimental parameters have been introduced in Section 6.1.

The assumptions for solving the buoyancy model and the fin equation are similar to those in Chapter 6, except that the thoughflow temperature and pressure are given for all the 10 cases. The detailed information required for predicting the disc temperature is shown in Table 7.1.

	Variables	Symbols
From working conditions	Disc temperature at $r = b$	$T_{o,b}$
	Angular speed of disc	Ω
	Throughflow temperature	T_f
	Throughflow pressure	p_f
From disc geometry	Nondimensional radius	x
	Nondimensional thickness	τ
	Angel of gradient of disc surface	α
Assuming the buoyancy region	Inner nondimensional radius of buoyancy region ($x_{a'} = x_a$)	$x_{a'}$
Giving the empirical constant	Coriolis parameter	Co
Convective boundary condition at $x = x_a$	Throughflow temperature below the cob	T_f
	Heat transfer coefficients	h_a
Assuming $\theta_a = Co, p_{c,a} = p_f$	Core temperature	T_c
	Core density	ρ_c

Table 7.1 Information required to apply the theoretical model

As discussed in Section 5.4, the theoretical model is applied to the whole cavity. The Coriolis parameter is chosen to minimize the difference between the average theoretical and experimental nondimensional disc temperatures, Θ_{av}. A single value of $Co = 0.030$ is used to for all the 10 cases in this chapter.

For the convective boundary condition, a form of the correlation for the convection on the inner surface of the cob, which was shown in Eq. (5.20), is used. Two empirical constants, B_1 and B_2, are included in the correlation. The two constants are adjusted to obtain the closest prediction of the average nondimensional disc temperature. In the end, based on the experiments by *Puttock-Brown*, B_1 and B_2 are optimised to 0.69 and 0.37. Hence the optimised form of Eq. (5.20) will be

$$Nu_a = 0.69 Re_T^{0.37} \tag{7.1}$$

As shown in Eq. (5.24), this correlation can be transferred to the boundary condition for the fin equation. With this boundary condition, the fin equation can be solved directly to compute disc temperatures. The theoretical model is solved to compute Nusselt numbers. The converged profiles of the disc temperature and the Nusselt number are the theoretical predictions.

7.1.2 Comparison between theory and experiment

Theoretical and experimental disc temperatures (Θ) and Nusselt numbers (Nu_f) are compared. The temperature measurements of all 10 cases in *Puttock-Brown* are taken as the experimental temperature. The 'experimental Nusselt numbers' are calculated from the temperature measurements using the Bayesian method. The theoretical temperatures and Nusselt numbers are predicted using the theoretical model in conjunction with the direct solution of the general fin equation. The convective boundary condition at $x = x_a$ is used for solving the fin equation. Table 7.2 presented the working parameters and the average experimental and theoretical disc temperatures (Θ_{av}) and Nusselt numbers (Nu_{av}).

The ranges of flow parameters are $4.1 \times 10^{11} < Gr_f < 1 \times 10^{12}$, $0.15 < \beta\Delta T < 0.35$, $1.6 \times 10^6 < Re_\phi < 3.0 \times 10^6, 1.1 \times 10^5 < Re_z < 5.1 \times 10^5$ and $0.1 < Ro < 0.6$. The Rossby numbers for the ten cases are all less than 1 and Gr_f values are all higher than 10^{11}, which means the buoyancy effects dominate the flow in the rotating cavity.

The theoretical predictions of the average disc temperature and Nusselt number are compared to the experimental ones in Fig. 7.1 and Fig. 7.2 respectively. Again, since Co is selected to minimize the differences between the theoretical and experimental average temperatures, Θ_{av} are very well predicted but Nu_{av} are slightly underpredicted. The differences between $\Theta_{av,th}$ and $\Theta_{av,exp}$ are all less than 0.025 and those between $Nu_{av,th}$ and $Nu_{av,exp}$ are within 20%. As the convective boundary condition is used, the results are more sensitive to Co values than the results for the experiments by *Atkins and Kanjirakkad*. Doubling *Co* from 0.03 to 0.06 will increase $Nu_{av,th}$ by 10-20%.

	Ro ≈ 0.6	Ro ≈ 0.3		Ro ≈ 0.2						Ro ≈ 0.1
Case No	a	b1	b2	c1	c2	c3	c4	c5	c6	d
Ro	0.61	0.31	0.31	0.16	0.16	0.18	0.17	0.17	0.17	0.10
$Gr_f/10^{11}$	2.5	10	10	4.2	4.5	6.8	7.2	7.2	7.8	4.1
$\beta\Delta T$	0.32	0.35	0.35	0.15	0.16	0.33	0.32	0.32	0.34	0.29
$Re_\phi/10^6$	1.6	3.0	3.0	3.0	3.0	2.5	2.7	2.7	2.7	2.1
$Re_z/10^5$	5.1	5.0	5.0	2.5	2.5	2.4	2.4	2.4	2.5	1.1
$\Theta_{av,exp}$	0.347	0.349	0.330	0.499	0.494	0.357	0.377	0.385	0.368	0.413
$\Theta_{av,th}$	0.368	0.349	0.351	0.504	0.487	0.366	0.368	0.366	0.359	0.400
$Nu_{av,exp}$	233	274	308	90.4	92.7	262	233	224	253	192
$Nu_{av,th}$	208	251	248	89.3	100	219	217	219	231	175

Table 7.2 Flow paramenters and experimental and theoretical average Nusselt numbers for 10 experimental cases of Puttock-Brown [2016]

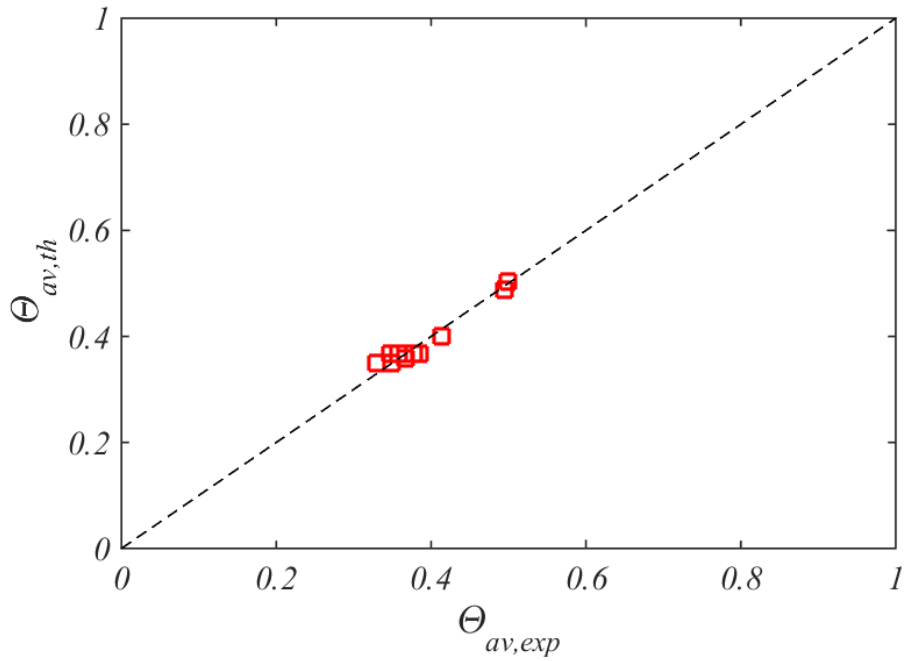

Fig. 7.1 Comparison of theoretical average disc temperature to experiments (Red squares: theoretical prediction of average disc temperaturse, broken line: $y = x$, the experimental values)

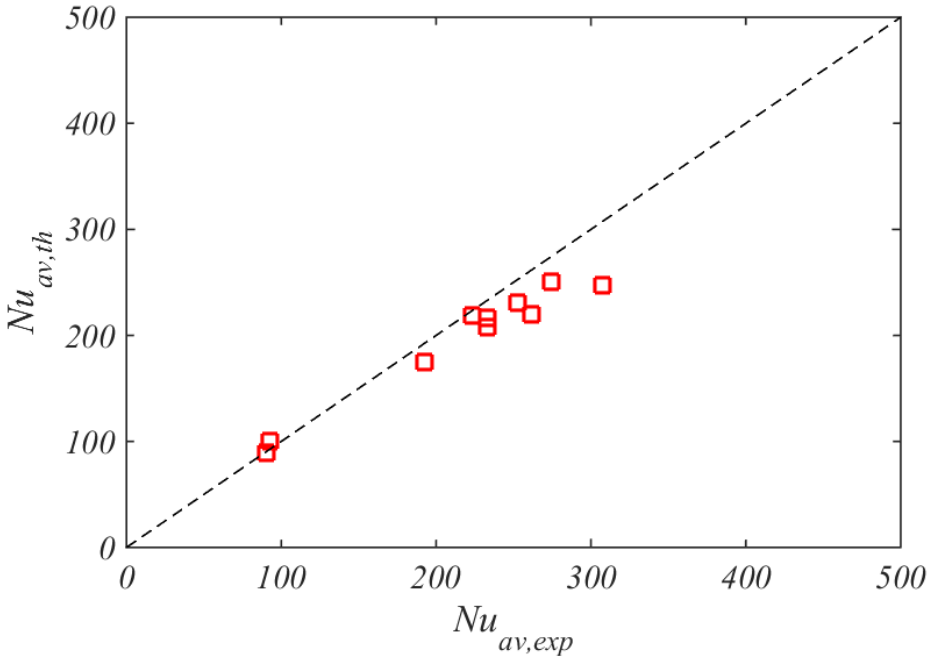

Fig. 7.2 Comparison of theoretical average Nusselt number to experiments (Red squares – theoretical prediction of average Nusselt numbers, broken line – $y = x$, the experimental values)

Fig. 7.3 to Fig. 7.6 show the comparison between the theoretical and experimental profiles of the disc temperature and the Nusselt number. On the left, radial distributions of temperatures are compared: the black circles and triangles denote the disc temperature measurements on the upstream and downstream face of the instrumented disc respectively; the blue squares are the measured core temperatures at one radius (the core temperatures are normalised using $(T_c - T_f)/(T_{o,b} - T_f)$); the red broken lines are the temperature curves which are calculated from the measured disc temperature using the Bayesian method in conjunction with the fin equation; The black solid and dashed lines are the theoretical prediction of the disc temperature and the core temperature respectively. On the right, the Nusselt number distributions are compared: The red broken curves are the 'experimental Nusselt numbers' calculated from the disc temperature measurements using the Bayesian method in conjunction with the fin equation; the background shades are their 95% confidence intervals; the solid curves are the theoretical predictions of Nusselt numbers.

Mainly good agreement between the theoretical and experimental distributions of disc temperatures and Nusselt numbers has been obtained for all 10 cases. Although the convective boundary condition is used, the local differences of the nondimensional disc temperature, Θ, between theory and experiment are all smaller than 0.05, which corresponds to the absolute temperature difference of around 5K. Nu_f are underpredicted near the shroud and overpredicted near the cob. As stated in Chapter 6, overprediction of the Nusselt numbers causes underprediction of the disc temperature and vice versa.

The distributions of the core temperature are also presented using the black dash lines. As the values of Re_ϕ for all 10 cases are quite high, it can be seen that the radial increase of the core temperature is significant.

Puttock-Brown measured the core temperatures at $x = 0.580$ which are shown in the figures using the blue squares. The theoretical predictions of the core temperature are compared to these

measurements. For case c1, c2, c3, c4, c5, c6 and d, the theoretical predictions agree well with the experiments. But for case a, b1 and b2, the measured core temperatures are very close to the measured disc temperatures. As the thermocouple for measuring the core temperature is close to the disc instead of the centre of the cavity, it is possible that the air temperatures in the Ekman layers instead of those in the core were measured for these cases.

As the theory is based on the laminar assumption, it appears that the buoyancy-induced flow for these ten cases is indeed laminar. The Re_ϕ effect, which was seen in Chapter 6, can also be found from the comparison between case c1 (or c2) and case d here. Due to the Re_ϕ effect, case c1, where Gr_f is similar to that of case d but Re_ϕ is larger, has much lower value of Nusselt numbers than case d.

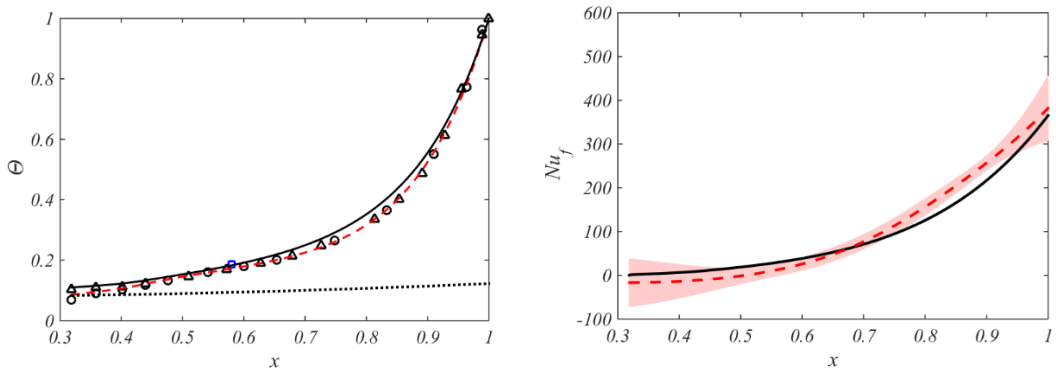

○, Δ: measured disc temperatures on upstream and downstream disc surfaces; □ : measured cavity temperature; ---, ▭: Results from the Bayesian method; —: theoretical predictions of disc temperatures and Nusselt numbers; ⋯: theoretical predictions of cavity air temperature

Fig. 7.3 Distributions of temperature and Nusselt numbers for *Ro* ≈ *0.6* – Case a

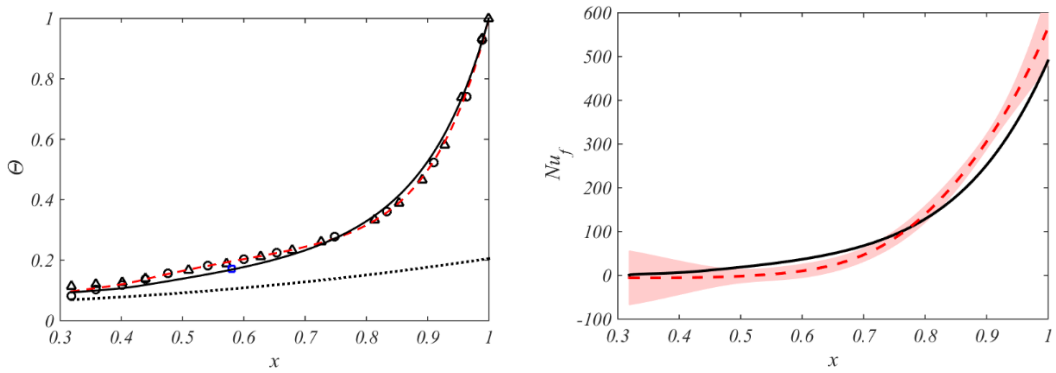

Fig. 7.4 (a) Case a1

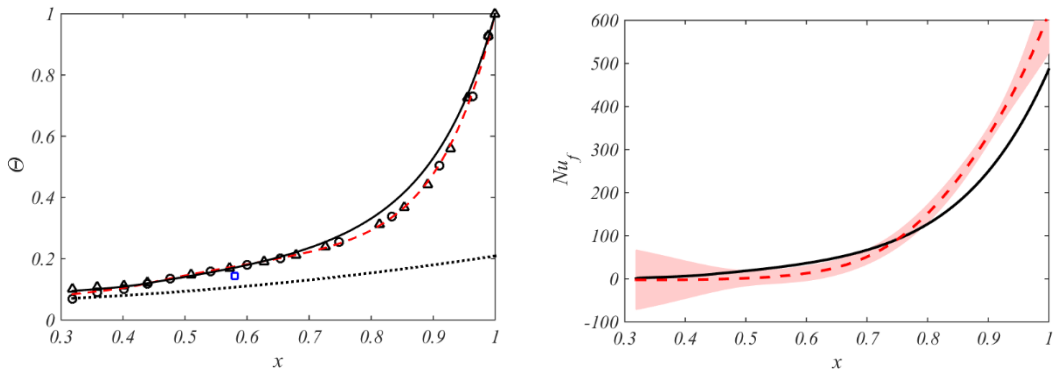

Fig. 7.4 (b) Case a2

○, Δ: measured disc temperatures on upstream and downstream disc surfaces; □ : measured cavity temperature; ---, ▭: Results from the Bayesian method; —: theoretical predictions of disc temperatures and Nusselt numbers; ⋯: theoretical predictions of cavity air temperature

Fig. 7.4 Distributions of temperature and Nusselt numbers for *Ro* ≈ *0.3* – Cases b1 and b2

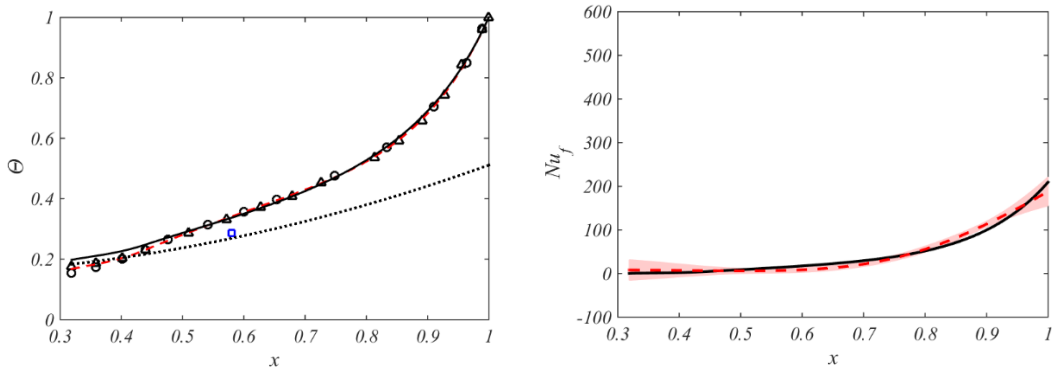

Fig. 7.5 (a) Case c1

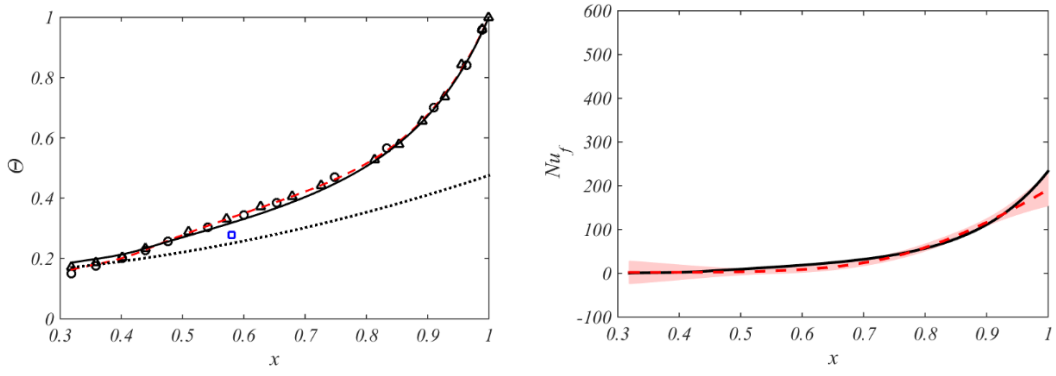

Fig. 7.5 (b) Case c2

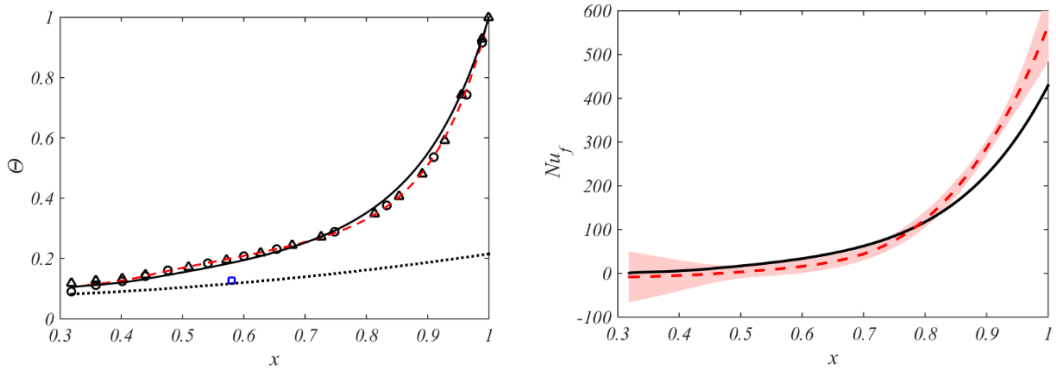

Fig. 7.5 (c) Case c3

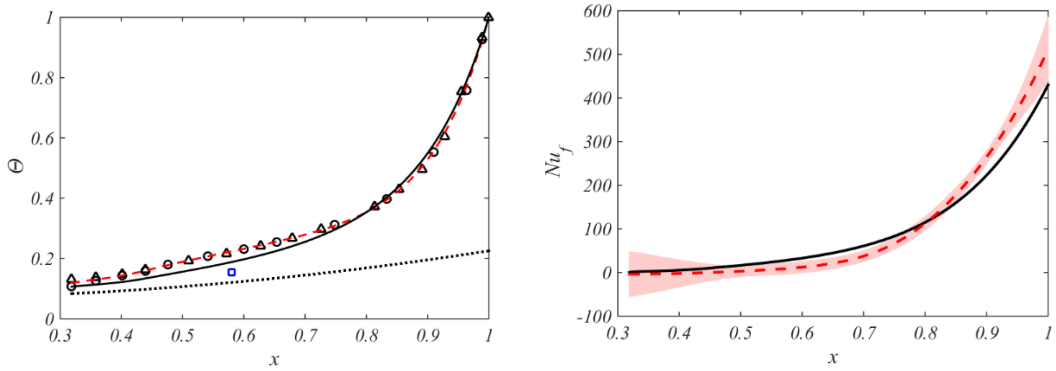

Fig. 7.5 (d) Case c4

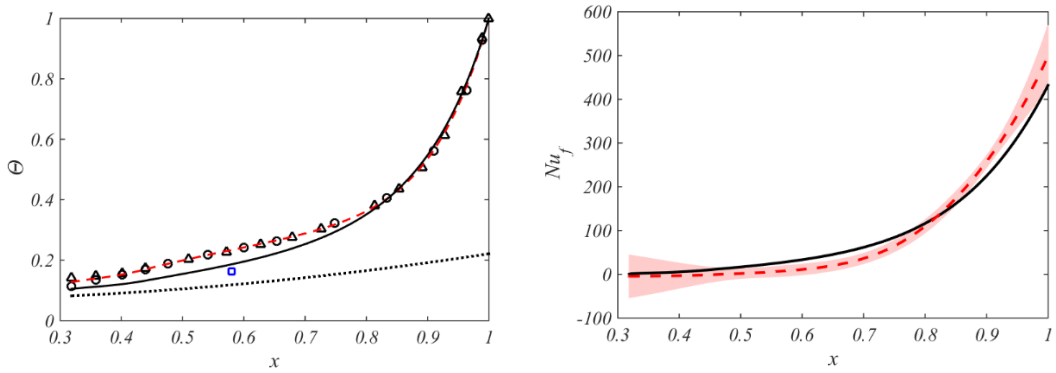

Fig. 7.5 (e) Case c5

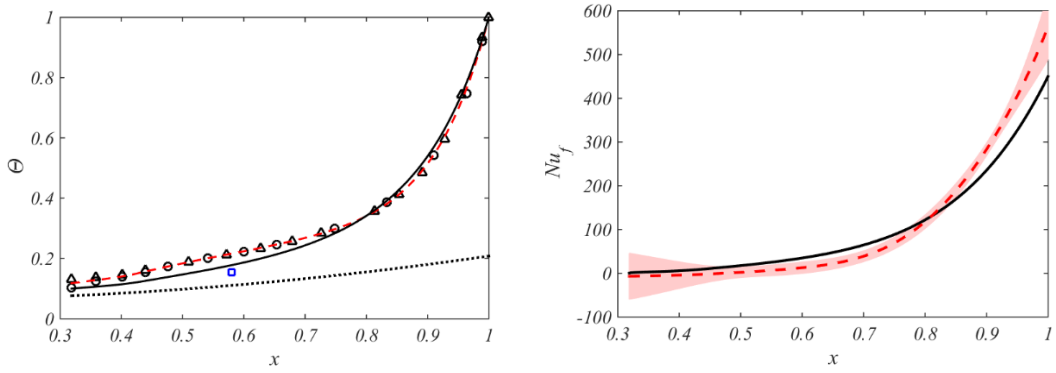

Fig. 7.6 (f) Case c6

○, Δ: measured disc temperatures on upstream and downstream disc surfaces; □ : measured cavity temperature; ---, : Results from the Bayesian method; —: theoretical predictions of disc temperatures and Nusselt numbers; ···: theoretical predictions of cavity air temperature

Fig. 7.5 Distributions of temperature and Nusselt numbers for *Ro* ≈ *0.2* – Cases c1 and c6

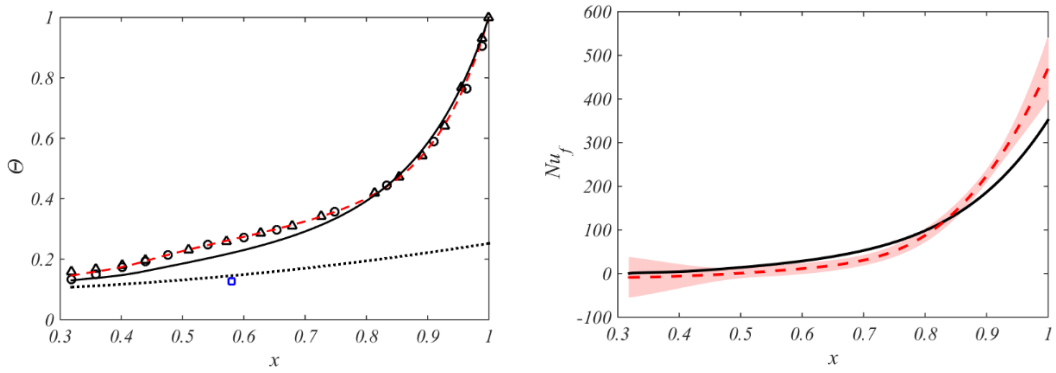

○, Δ: measured disc temperatures on upstream and downstream disc surfaces; □ : measured cavity temperature; ---, : Results from the Bayesian method; —: theoretical predictions of disc temperatures and Nusselt numbers; ···: theoretical predictions of cavity air temperature

Fig. 7.6 Distributions of temperature and Nusselt numbers for *Ro* ≈ *0.1* – Case d

7.2 Prediction of throughflow temperature rise

7.2.1 Comparison between theory and experiment

Section 5.5 presents the method to predict the bulk mean temperature rise of the axial through flow. The energy balance equation is developed for a region confined by the mid faces of two adjacent cavities. It was shown that the total-temperature rise of the axial throughflow, $(T_{f,i+1/2} - T_{f,i-1/2})$, is determined by the heat transfer from the shroud and the disc.

The heat transfer from the disc comprises that from the two radial surfaces and that from the inner surface of the cob. The radial distribution of the disc temperature and the Nusselt number were predicted in Section 7.1, so the heat flux from the two disc radial surfaces can be calculated by integrating the heat flux on both faces from $r = a$ to $r = b$. As the calculated Nusselt number is actually equivalent to the average of the values for two disc faces, so the theoretical prediction of the heat flux on both faces are identical. Then the heat transfer on the radial disc surface, which is denoted as $\dot{Q}_o$, can be calculated with Eq. (5.29). For the heat transfer on the inner surface ($\dot{Q}_a$), the cob correlation in Eq. (7.1) and Eq. (5.26) are used. Then the heat transfer from the disc can be calculated using Eq. (5.30).

To calculate the heat transfer for the shroud, a correlation for laminar free convection on horizontal plates, Eq. (5.31), is used. The heat flux for the shroud is denoted as $\dot{Q}_{sh}$ and can be computed using Eq. (5.35). In the end, the bulk mean temperature rise can be predicted using Eq. (5.36).

Puttock-Brown also measured the air temperature increase from $T_{f,i-1}$ to $T_{f,i+1}$ and the prediction is compared with the experimental data in Fig. 7.7. Although the predictions tend to underestimate the measured values, overall reasonably good agreement between the theory and the experiments has been achieved.

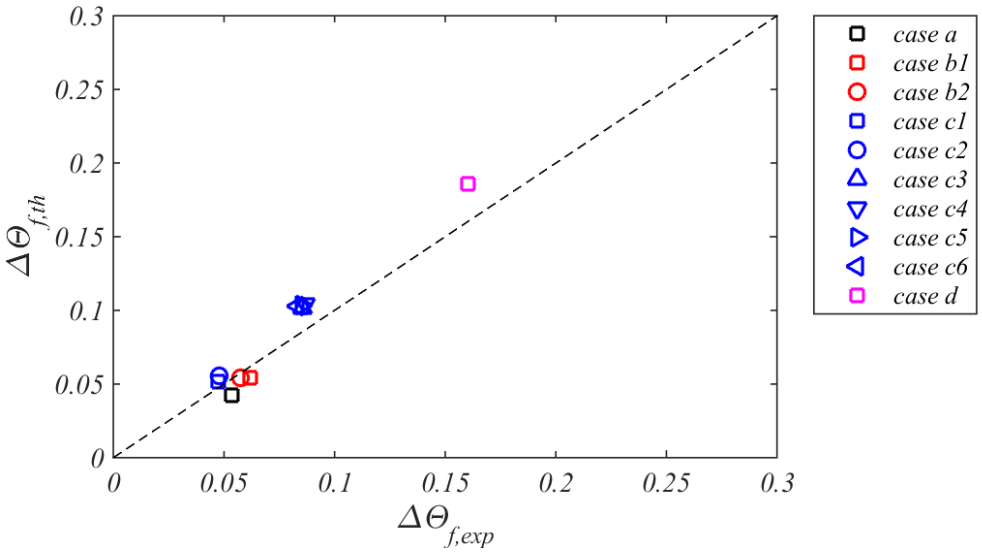

Fig. 7.7 Comparison between theoretical and experimental temperature increase of axial throughflow (symbols denote the theoretical prediction, the broken line denotes the experimental values.)

7.2.2 Discussion

The theoretical values underpredicted the temperature increase for cases a, b1 and b2 but overpredicted those for cases c1-c6 and d. There are various reasons for this discrepancy. As mentioned in Chapter 5, the temperature increase predicted by the theory is the bulk-mean total temperature of the axial throughflow, while the experimental values are the temperature measurements at only one radial location, which is not the bulk mean total temperature. Moreover, the correlation of the laminar free convection on horizontal plates, $Nu_{sh} = 0.54(Gr_{sh}Pr)^{1/4}$, is used here to calculate heat transfer for the shroud, but the constant, 0.54, may need to be adjusted for rotating cylinders.

7.3 Summary

This chapter has extended the validation of the theoretical model described in Chapter 6, using the experimental data of *Atkins and Kanjirakkad [2014]*, to the experimental values obtained by *Puttock-Brown [2016]* on the Sussex multi-cavity rig. The ranges of the experimental parameters were $2 \times 10^{11} < Gr_f < 10^{12}$; $1.5 \times 10^6 < Re_\phi < 3.0 \times 10^6$;

$5.1 \times 10^3 < Re_z < 5.1 \times 10^4;\ 0.05 < Ro < 0.61;\ 0.13 < \beta\Delta T < 0.36$. As well as predicting the disc temperatures and Nusselt numbers, the core temperatures and the temperature rise of the throughflow were also predicted. This involved using empirical correlations for forced convection from the cob and free convection from the shroud in conjunction with the theoretical model and the fin equation. For the buoyancy model, a single value of the Coriolis parameter $Co = 0.030$ was used, and for the fin equation, the convective boundary condition at x_a is used.

The 'experimental Nusselt numbers' were obtained from the disc temperature measurements using the Bayesian statistics in conjunction with the fin equation. Mainly good agreement between the theoretical and the experimental disc temperatures and Nusselt numbers has been obtained. This provides additional evidence that Ekman layer flow in rotating cavities in real engines, where $Gr = O(10^{12})$, could indeed be laminar. Reasonable agreement between theoretical distributions of the core temperature and experimental values (measured at only one radial location) has also been achieved.

The increase of the bulk-mean temperature of the throughflow has been predicted using a heat balance incorporating the prediction of heat transfer from the shroud and disc. The predictions were in reasonably good agreement with the experimental values measured by *Puttock-Brown*, and possible reasons for any differences have been suggested.

Chapter 8 – Conclusions and Future Work

8.1 Conclusions

In this thesis, the buoyancy-induced flow and heat transfer inside compressor rotors is modelled assuming laminar Ekman-layer flow on the discs and compressible flow in the fluid core between the Ekman layers; conduction in the compressor discs is modelled using a one-dimensional fin equation. This is a strongly conjugate problem where the equations for the disc temperature and the Nusselt numbers are coupled.

Bayesian statistics have been used to determine the Nusselt numbers, (Nu), or equivalently the Biot numbers (Bi), from the inverse solution of the fin equation. Using simulated temperature distributions, the Bayesian method produced a smooth distribution of *Bi*, and the computed 95% confidence interval captured the true *Bi* distribution. By contrast, conventional curve-fitting methods - using polynomials to approximate the simulated temperatures - resulted in large oscillations and inaccurate results.

Theoretical disc temperatures and Nusselt numbers, calculated using the buoyancy model of *Owen and Tang [2015]* assuming laminar Ekman-layer flow on the discs and compressible flow in the fluid core, have been compared with experimental data obtained from measurements in the multi-cavity compressor rigs of *Atkins and Kanjirakkad [2014]* and *Puttock-Brown [2016]*. The ranges of the experimental parameters for *Atkins and Kanjirakkad* were: $1.7 \times 10^8 < Gr_f < 9.1 \times 10^{11}; 7.7 \times 10^4 < Re_\phi < 3.5 \times 10^6; 1.8 \times 10^4 < Re_z < 1.1 \times 10^5; 0.3 < Ro < 5; 0.05 < \beta\Delta T_f < 0.32$. The ranges of *Puttock-Brown's* experiments were: $2.2 \times 10^{11} < Gr_f < 10^{12}$; $1.5 \times 10^6 < Re_\phi < 3.0 \times 10^6$; $5.1 \times 10^3 < Re_z < 5.1 \times 10^4$; $0.05 < Ro < 0.61$; $0.13 < \beta\Delta T_f < 0.36$. The 'experimental' Nusselt numbers were obtained by applying

Bayesian statistics to inverse solutions of the general fin equation. Solved in conjunction with the fin equation, the buoyancy model predicted the radial distribution of the Nusselt numbers and temperature of the disc.

For all cases, the measured temperature of the rotor shroud was used as the outer boundary condition for the fin equation. In the 19 cases of *Atkins and Kanjirakkad*, where the temperature of the axial throughflow was not measured, the measured temperature of the inner surface of the cob was used for the inner boundary condition of the disc. For the 10 cases of *Puttock-Brown*, where the temperature of the throughflow was measured, a convective correlation was used for the inner boundary condition. To optimise the fit between the predicted and measured disc temperatures, values of *Co*, an empirical Coriolis parameter in the buoyancy model, were assumed to be 0.029 and 0.030 for the experiments of *Atkins and Kanjirakkad* and *Puttock-Brown* respectively.

The results suggested that buoyancy-induced flow did not occur until $Gr_f > 8.5 \times 10^8$, and above this value there was mainly good agreement - particularly at the higher Grashof numbers - between the theoretical and experimental distributions of Nusselt numbers and disc temperatures. This agreement suggests that the Ekman-layer flow could remain laminar even at the high Grashof numbers found inside compressor rotors, where $Gr_f = O(10^{12})$. For *Puttock-Brown's* data, mainly good agreement was also achieved between the predicted and experimental core temperatures, which were measured at a single radial location. The compressibility effect in the core means that an increase in Gr_f, caused by an increase in Re_ϕ, can – under some conditions - result in a *decrease* in Nu_f.

The theoretical model, comprising the coupled buoyancy model and fin equation, was extended to calculate the convective heat transfer from the shroud and cobs. A correlation for free convection on horizontal plates was used to calculate the heat transfer from the shroud, and an optimised forced-convection correlation was used to calculate the heat transfer from the cob.

The extended model was then used to predict the temperature increase in the axial throughflow, and the predictions were in reasonable agreement with the measured temperatures of *Puttock-Brown*.

This is the first time a theoretical model (rather than CFD) has been used to predict the temperatures of a compressor disc and the axial throughflow, and the model takes only seconds to predict the temperatures that would take days or even weeks to compute using CFD. More research is required to fully test the model, and some suggestions are made below. Much of this research will be conducted in a project, funded by EPSRC and starting in January 2017, involving collaboration between Bath University, Surrey University and Rolls Royce.

8.2 Future work

To apply the buoyancy model, a value is needed for the empirical Coriolis parameter (*Co*), which depends on the geometry of the cavity, on the size of the cobs and on the working conditions. Its value was chosen here to ensure that the disc Nusselt number was zero at $r = a$ (which also determines the temperature of the core at inlet to the cavity), and to minimise the difference between the theoretical and experimental average disc temperatures. More experimental data are needed to develop a more general correlation for Co.

In this thesis, the temperature of the core at the inner radius of the buoyancy region, $T_{c,a'}$, was derived from the value of Co and the zero-Nusselt-number assumption. In practice, $T_{c,a'}$ will depend on the toroidal vortex, which creates the interface between the axial throughflow and the buoyancy-induced flow in the cavity. As discussed in Chapter 2, the radial extent of the toroidal vortex decreases as *Ro* decreases. For small values of *Ro*, the term 'toroidal vortex' may be misleading as the buoyancy-induced flow in the cavity will eventually be separated from the throughflow by a thin shear layer in which Kelvin-Helmholtz instability (see *Tritton [1988]*) is likely to occur. It was assumed here that the buoyancy region starts at $= a$, which means that

$T_{c,a'} = T_{c,a}$, but more experimental or computational evidence is required to test this and the zero-Nusselt-number assumption.

As far as the author is aware, there are no published correlations for heat transfer from the inner surface of the cobs to the throughflow or for the relationship between the total heat transfer and the temperature difference across the shear layer. In addition, the core temperature depends on how much heat is convected from the cavity to the throughflow through the axial gap between adjacent cobs, and the temperature of the core will be affected by the size of this gap. More research is required for both of these topics.

The fin equation is based on the assumption that the Nusselt numbers are the same on the upstream and downstream surfaces of the disc. In general, this will not be true, and the Nusselt numbers presented in this paper are an average of the two values. It would therefore be helpful if, in some future experiments, tests could be conducted with one surface of the instrumented disc thermally insulated.

The current theoretical model has been applied only to steady-state tests, and modifications would be needed for transient cases, which are particularly important for aeroengines. Although it would be relatively easy to develop a transient 1D fin equation, it would be better to use a 2D version of Fourier's equation for the disc in conjunction with a quasi-unsteady version of the buoyancy model. This would also involve extending the Bayesian model to include the inverse solution of the 2D conduction equation, enabling 'experimental' Nusselt numbers to be used to validate the predicted values.

References

Alexiou, A., 2000, "Flow and Heat Transfer in Gas Turbine HP Compressor Internal Air Systems", PhD thesis, University of Sussex.

Atkins, N. R., and Kanjirakkad, V., 2014, "Flow in a Rotating Cavity with Axial Throughflow at Engine Representative Conditions", ASME Paper GT2014-27174.

Bohn, D., Deuker, E., Emunds, R. and Gorzelitz, V., 1995, Experimental and Theoretical Investigations of Heat Transfer in Closed Gas-Filled Rotating Annuli", Journal of turbomachinery, 117(1), 175-183.

Bohn, D. E., Deutsch, G. N., Simon, B. and Burkhardt C. "Flow Visualisation in a Rotating Cavity with Axial Throughflow," ASME Paper 2000-GT-0280.

Bohn, D., Ren J. and Tuemmers C., 2006, "Investigation of the Unstable Flow Structure in a Rotating Cavity", ASME Paper GT2006-90494.

Cho, G., Tang, H., Owen, J.M. and Lock, G.D. 2016 "On the measurement and analysis of data from transient heat transfer", International Journal of Heat and Mass Transfer, 98, 268-276.

Cumpsty, N. A., 2015, "Jet Propulsion: A Simple Guide to the Aerodynamics and Thermodynamic Design and Performance of Jet Engines", Cambridge University Press.

Farthing, P.R., Long, C.A., Owen, J.M. and Pincombe, J.R., 1992a, "Rotating Cavity with Axial Throughflow of Cooling Air: Heat Transfer", ASME J. Turbomach., 114(1), pp. 229-236.

Farthing, P.R., Long, C.A., Owen, J.M. and Pincombe, J.R., 1992b, "Rotating Cavity with Axial Throughflow of Cooling Air: Flow Structure", ASME J. Turbomach., 114(1), pp. 237-246.

Gnanasekaran, N., and Balaji, C., 2011, "A Bayesian Approach for the Simultaneous Estimation of Surface Heat Transfer Coefficient and Thermal Conductivity from Steady State Experiments on Fins", Int. J. Heat Mass Trans. 54(13), 3060-3068.

Grossmann, S., and Lohse, D., 2000, "Scaling in Thermal Convection: A Unifying Theory", J. Fluid Mech., 407, pp. 27–56.

Günther, A, Uffrecht, W., and Odenbach, S, 2014, "The Effects of Rotation and Mass Flow on Local Heat Transfer in Rotating Cavities with Axial Throughflow", ASME Turbo Expo 2014.

Hollands, K. G. T., Raithby, G. D., and Konicek, L., 1975, "Correlation Equations for Free Convection Heat Transfer in Horizontal Layers of Air and Water", Int. J. Heat Mass Transfer, 18(7–8), 879–884.

Incropera, F. P. and DeWitt, D. P., 1996, "Fundamentals of Heat and Mass Transfer", Wiley, New York.

Kaipio, J. and Somersalo, E., 2006, "Statistical and Computational Inverse Problems", Springer Science & Business Media, Vol. 160.

Kim, S. Y., Han, J. C., Morrison, G. L. and Elovic, E., 1994, "Local Heat Transfer in Enclosed Co-Rotating Disks with Axial Throughflow", Journal of Heat Transfer, *116*(1), 66-72.

Long, C. A., 1994, "Disk Heat Transfer in a Rotating Cavity with an Axial Throughflow of Cooling Air", International Journal of Heat and Fluid Flow, 15(4), 307-316.

Long, C. A. and Tucker, P. G., 1994, "Shroud Heat Transfer Measurements from a Rotating Cavity With an Axial Throughflow of Air", Journal of Turbomachinery, 116(7), 525-534.

Long, C. A., Morse, A. P. and Tucker, P. G., 1997, "Measurement and Computation of Heat Transfer in High-Pressure Compressor Drum Geometries with Axial Throughflow", Journal of Turbomachinery, 119(1), 51-60.

Long, C. A., Alexiou, A. and Smout, P. D., 2003, "Heat Transfer in HP Compressor Gas Turbine Internal Air Systems: Measurements from the peripheral Shroud of a Rotating Cavity with Axial Throughflow", In HEFAT2003, 2nd Intl. Conf. on Heat Transfer, Fluid Mechanics, and Thermodynamics, Paper No. LC1.

Long, C. A., Miché, N. D. D. and Childs, P. R. N., 2007, "Flow Measurements inside a Heated Multiple Rotating Cavity with Axial Throughflow", Int. J. Heat Fluid Flow, 28(6), 1391-1404.

Long, C. A., and Childs, P. R. N., 2007, "Shroud Heat Transfer Measurements inside a Heated Multiple Rotating Cavity with Axial Throughflow", Int. J. Heat Fluid Flow, 28(6), 1405–1417.

Matérn, B., 1960, "Spatial Variation: Stochastic Models and their Application to Some Problems in Forest Surveys and Other Sampling Investigations", Meddelanden fran statens Skogsforskningsinstitut, 49(5).

Miché, N. D., 2009, "Flow and heat transfer measurements inside a heated multiple rotating cavity with axial throughflow", PhD thesis, University of Sussex, UK.

O'Hagan, A., 1994, "Kendall's Advanced Theory of Statistics," Vol. 2B: Bayesian Inference.

Owen, J. M. and Pincombe, J. R., 1979, "Vortex Breakdown in a Rotating Cylindrical Cavity", Journal of Fluid Mechanics, 90(01), 109-127.

Owen, J. M. and Powell, J., 2006, "Buoyancy-induced Flow in a Heated Rotating Cavity", Journal of Engineering for Gas Turbines and Power 128(1), 128-134.

Owen, J. M., Abrahamsson, H. and Lindblad, K., 2007, "Buoyancy-Induced Flow in Open Rotating Cavities", Journal of Engineering for Gas Turbines and Power, 129(4), 893-900.

Owen, J. M., 2010, "Thermodynamic Analysis of Buoyancy-Induced Flow in Rotating Cavities", Journal of Turbomachinery, 132(3), 031006.

Owen, J. M. and Long, C. A., 2015, “Review of Buoyancy-Induced Flow in Rotating Cavities”, ASME J. Turbomach, 137(11), 111001.

Owen, J.M. and Tang, H., 2015, “Theoretical Model of Buoyancy-Induced Flow in Rotating Cavities”, ASME J. Turbomach, 137(11), 111005.

Puttock-Brown, M., 2017, “Experimental and Numerical Investigation of Flow Structure and Heat Transfer in Gas Turbine H.P. Compressor Secondary Air Systems”, to be submitted for the degree of DPhil, University of Sussex.

Rolls-Royce, 1986, “The Jet Engine”, John Wiley & Sons.

Stein, M. L. 1999, “Interpolation of Spatial Data: Some Theory for Kriging”, Springer, New York.

Sun, Z., Kifoil, A., Chew, J. W. and Hills, N. J., 2004, “Numerical Simulation of Natural Convection in Stationary and Rotating Cavities”, ASME Paper GT2004-53528.

Sun, Z., Lindblad, K., Chew, J. W. and Young, C., 2007, “LES and RANS Investigations into Buoyancy-Affected Convection in a Rotating Cavity with a Central Axial Throughflow”, Journal of Engineering for Gas Turbines and Power, 129(2), 318-325.

Tan, Q., Ren, J. and Jiang, H., 2009, “Prediction of Flow Features in Rotating Cavities with Axial Throughflow by RANS and LES”, ASME Paper GT2009-59428.

Tan, Q., Ren, J., Jiang H., 2014, “Prediction of 3D Unsteady Flow and Heat Transfer in Rotating Cavity by Discontinuous Galerkin Method and Transition Model”, ASME Paper GT2014-26584.

Tang, H., Shardlow, T., and Owen, J.M., 2015, “Use of Fin Equation to Calculate Nusselt numbers for Rotating Discs”, ASME J. Turbomach, 137(12), 121003.

Tang, H. and Owen, J.M., 2016, “Effect of Buoyancy-Induced Flow on Temperatures of Compressor Discs”, ASME J. Eng. Gas Turbines Power, in press.

Tian, S., Tao, Z., Ding, S. and Xu, G., 2004, “Investigation of Flow and Heat Transfer Instabilities in a Rotating Cavity with Axial Throughflow of Cooling Air”, ASME Paper GT2004-53525.

Tian, S., Tao, Z., Ding, S. and Xu, G., 2008, “Computation of Buoyancy-Induced Flow in a Heated Rotating Cavity with an Axial Throughflow of Cooling Air”, International Journal of Heat and Mass Transfer, 51(3), 960-968.

Tian, S. and Zhu, Y., 2012, “Disk Heat Transfer Analysis in a Heated Rotating Cavity with an Axial Throughflow”, ASME Paper GT2012-69185.

Tritton, D. J., 1988, “Physical Fluid Dynamics”, OUP, New York.

Tucker, P. G., 1993, “Numerical and Experimental Investigation of Flow Structure and Heat Transfer in a Rotating Cavity with an Axial Throughflow of Cooling Air”, PhD thesis, University of Sussex.